공학박사 학위논문

# Shape Control of Semiconductor Nanocrystals and Their Applications to Optoelectronic Devices

# 반도체 나노입자의 형상제어 및 광전자소자로의 응용

2013년 2월

서울대학교 대학원

공과대학 화학생물공학부

임 재 훈

공학박사 학위논문

# Shape Control of Semiconductor Nanocrystals and Their Applications to Optoelectronic Devices

# 반도체 나노입자의 형상제어 및 광전자소자로의 응용

2013년 2월

서울대학교 대학원

공과대학 화학생물공학부

임 재 훈

# Shape Control of Semiconductor Nanocrystals and Their Applications to Optoelectronic Devices

지도 교수 차 국 헌

이 논문을 공학박사 학위논문으로 제출함

2013년 2월

서울대학교 대학원

공과대학 화학생물공학부

임 재 훈

임재훈의 공학박사 학위논문을 인준함

2013년 2월

위 원 장 현 택 환 (인)

부위원장 차 국 헌 (인)

위 원 이 성 훈 (인)

위 원 이 창 희 (인)

위 원 강 문 성 (인)

## Abstract

# Shape Control of Semiconductor Nanocrystals and Their Applications to Optoelectronic Devices

Jaehoon Lim

School of Chemical and Biological Engineering

College of Engineering

Seoul National University

Shape- and size-controlled semiconductor nanocrystals have recently drawn keen attention due to their tunable optical and electrical properties. Precise control in their dimension and spatial chemical composition (i.e., dot, rod, or tetrapod structure with homogeneous or multi-compositions) enables us to manipulate their electronic states, exciton generation/relaxation dynamics, and transport phenomena, which determines light absorption, fluorescence, or carrier transport within nanocrystals or nanocrystals arrays. In order to realize their full potentials to practical applications based on these promising materials,

deeper understanding on their physical and chemical properties as well as systematic utilization should be progressed. In these regards, design principles on semiconductor nanocrystals to control optical or electrical properties and their applications to optoelectronic devices are discussed.

For effective generation of photons from other energy sources, spherical-shaped InP quantum dots with ZnSeS chemical composition gradient are synthesized by wet chemistry. The composition gradient of Se in the shell phase is easily achieved by one-pot approach with a simple addition of both Se and S precursors at the same time, where Se is dominantly located close to the InP cores while S content increases along the radial direction of the shell. The introduction of the ZnSeS composition gradient shells ensures high quantum efficiency above 70 % due to the successful passivation of surface states with reduced lattice strain and also improves chemical stability against chemical and physical stress.

In order to facilitate the exciton dissociation for photovoltaic devices, tetrapod-shaped cadmium selenide nanocrystals are synthesized by “continuous precursor injection” approach. The “continuous precursor injection” implies the successive injection of precursor solution and branching agent using a syringe pump with a controlled injection rate. The CdSe tetrapods prepared with new synthetic route exhibit exceptional shape selectivity above 90 % as well

as finely tunable dimensions varying from 1 to above 40 in aspect ratio simply by controlling the reaction temperature and injection rate. Moreover, these high quality tetrapods can be easily scaled-up in multi-gram quantity without reduction in morphological uniformity.

Using the InP quantum dots with ZnSeS chemical composition gradient shells, highly efficient and bright green light emitting diodes are demonstrated. On the basis of an inverted device structure, solution-processed interfacial dipole was introduced for minimizing electron injection barrier between an electron transport layer to InP quantum dots. Optimized carrier transport energy levels allows direct injection of charge carriers within quantum dots, which leads to the considerable improvement in external quantum efficiency of the devices in entire operation range.

To utilize CdSe tetrapods in organic-inorganic hybrid solar cells in reproducible and reliable manner, sequential fabrication is employed to realize bicontinuous hybrid morphology. The sequential fabrication solves the poor colloidal stability of ligand-less tetrapods as well as the inseparable fabrication variables participating in nanoscopic morphology and surface state of nanocrystals. It is found that primary amines could effectively passivate surface state of CdSe nanocrystal phase and contribute to the enhancement of device performance. The improved device performance is rationalized by the reduced

bimolecular recombination of charged carriers at the trap sties. The optimized device shows considerable power conversion efficiency up to 2.2 % with high reproducibility.

This thesis demonstrates the practical approaches to exploit semiconductor nanocrystals into the practical devices, covering the tailored synthesis of nanocrystals, suitable device structure, and novel processing method. It is believed that this comprehensive approach will make a success on the realization of emerging nanoscience into the practical optoelectronic applications.

**Keywords: Semiconductor Nanocrystals, Quantum Dots, Tetrapods, Quantum Dot-Based Light Emitting Diodes, Organic-Inorganic Hybrid Solar Cells**

**Student Number: 2007-21216**

# Contents

**Chapter 1 Introduction ..... 1**

1.1 Fundamental properties of semiconductor nanocrystals .....1

1.2 Design principle of semiconductor nanocrystals for optoelectronic devices.....10

1.3 Applications of shape-controlled semiconductor nanocrystals .....23

1.3.1 Quantum dot-based light emitting diodes (QD-LEDs) .....23

1.3.2 Semiconductor nanocrystal-based photovoltaic devices .....29

1.3.3 Water splitting systems.....32

**Chapter 2 Synthesis of Shape-Controlled Semiconductor Nanocrystals for Photon-Electron Conversion Materials**..... 34

2.1 InP@ZnSeS, core@composition gradient shell quantum dots for efficient lumophors.....34

2.1.1 Introduction .....34

2.1.2 Experimental section .....37

2.1.3 Results and Discussions .....40

2.1.4 Conclusions .....55

2.2 Scalable and Controllable Synthesis of CdSe Tetrapods with High Morphological Uniformity by Persistent Kinetic Growth and Halide-Mediated Phase Transformation .....56

2.2.1 Introduction .....56

2.2.2 Experimental section ..... 59
2.2.3 Results and Discussions ..... 64
2.2.4 Conclusions ..... 82

**Chapter 3 Fabrication of InP Quantum Dot-Based Light Emitting Diodes** ..... 83
3.1 Introduction ..... 83
3.2 Experimental section ..... 86
3.3 Results and Discussions ..... 89
3.4 Conclusions ..... 101

**Chapter 4 Stepwise Formation of CdSe Tetrapod:P3HT Bulkheterojunction for Hybrid Solar Cells** ..... 102
4.1 Introduction ..... 102
4.2 Experimental section ..... 106
4.3 Results and Discussions ..... 112
4.4 Conclusions ..... 132

**Chapter 5 Conclusion and Outlook** ..... 133

**Bibliography** ..... 142

**Abstract** ..... 158

# List of Tables

**Table 2.1.1** Temporal change in atomic contents for InP@ZnSeS QDs with n = 2 and r = 0.05. (Values in bracket mean standard deviations in estimation) .....43

**Table 2.1.2** Estimated shell thicknesses of core@shell QDs with an optimal ratio of TOPSe (r). .....49

**Table 2.2.1** The effect of various types of branching agents on the shape of CdSe nanocrystals: group I) bromine compounds with different counterparts (i.e., $NH_4Br$, tetrabutylammonium bromide (TBAB), and CTAB); group II) halide compounds with the same cation part (i.e., tetrabutylammonium chloride (TBAC), TBAB, and tetrabutylammonium iodide (TBAI)) (T: tetrapods). .....74

**Table 2.2.2** Amount of oleate ligands on spherical CdSe nanocrystals depicted in Figure 2.2.8a. .....77

**Table 3.1** Optical properties and device performance of InP QLEDs according to the concentration of PFN. .....99

**Table 4.1** Summary of current density ($J_{SC}$), open-circuit voltage ($V_{OC}$), fill-factor (FF), and power conversion efficiency (PCE) of CdSe tetrapod:P3HT BHJ solar cells in Figure 4.5. .....127

**Table 4.2** Summary of current density ($J_{SC}$), open-circuit voltage ($V_{OC}$), fill-factor (FF), and power conversion efficiency (PCE) of CdSe tetrapod:P3HT BHJ solar cells with the arm length of 40 nm, 76 nm, and 103 nm, as shown in Figure 4.6. .....130

# List of Figures

**Figure 1.1** (a) The band structure for bulk semiconductor and nanocrystals with cubic lattice around **k** = 0. This illustration is reconstructed from C. B. Murray et al. (b) Atom-like S, P, and D orbitals of spherical semiconductor nanocrystals. © 2009 American Chemical Society. (c) A schematic on building up of electrons in a strongly-confined spherical semiconductor nanocrystals ($E_S$: single-electron energy level; $E_C$: charging energy; $E_{e\text{-}e}$: Coulomb repulsion). This illustration is redesigned from D. Vanmaekelbergh, D et al. .....2

**Figure 1.2** (a) (left) A schematic on conventional hot-injection method for group II-VI QDs. (right) The temporal change in degree of supersaturation (The LaMer plot). Rapid injection of precursors (region I) results in sudden supersaturation over critical point, resulting in burst nucleation of QDs (region II). In following period, QDs grow to finite size (region III), depending on the reaction parameters. (b) Size-dependent optical spectra for monodisperse CdSe QDs. (c) An absorption spectrum of CdSe QDs and the manifolds of excitonic states. .....4

**Figure 1.3** Schematic illustrations of various dimensional materials (left) and corresponding density of states (right). .....5

**Figure 1.4** (a) Representative shape variation of CdSe nanocrystals, from dots (0-D), rods(1-D) and tetrapods (3-D). (b) Spatial distribution of electron and hole wavefunction in various nanocrystal shape. © American Chemical Society. (c) Carrier transport mode in semiconductor nanocrystals. .....8

**Figure 1.5** (a) An absorption and photoluminescence spectrum of CdS QDs. The trap emission is denoted as a red arrow. (b) Schematics on the effect of surface states on the recombination process. The band structure as a function of **k** and the other relaxation processes are omitted for the simplicity. .....11

**Figure 1.6** Schematics on (a) a type-I bandgap configuration and (b) type-II bandgap configurations. The type-I bandgap configuration confines electron and hole wavefunctions in a same space, improving the recombination probability and it produces the band-edge emission. While the type-II bandgap configuration divides electron wavefunctions spatially, as a result, the probability on the radiative recombination is reduced and photon energy is the difference between the conduction (valence) band of core and valence (conduction) band of shell. (c) Electronic energy levels of several group II-VI, III-V, IV-VI, VI semiconductor materials using the valence-band offsets. ...14

**Figure 1.7** (top) A picture of core/shell structured II-VI QD dispersions illuminated under UV irradiation (352 nm) and (bottom) representative emission spectrum. .....15

**Figure 1.8** (a) TEM images of representative shape-controlled CdSe nanocrystals. (b) Fraction of atoms on the nanocrystal surface as a function of the total number of atoms. The wires (purple) are 1 μm in length, the disks (green) are 20 nm in length, and the rods (red) are 4 nm in diameter. © 2009 American Chemical Society. .....19

**Figure 1.9** (a) A schematic on solution-liquid-solid growth process. (b) A schematic of oriented attachment process. (c) (left) Surface energy of wurtzite ZnS nanocrystals, where (00$\underline{1}$) facet has the highest surface energy. (right)

Comparision of thermodynamic and kinetic growth of PbS nanocrystals. At high temperature above two activation energy barrier, the formation of thermodynamically-stable truncated cube is preferred. At low temperature, the kinetic process causes a rod shape. © 2006 Wiley-VCH. .....20

**Figure 1.10** Schematics on simplified device structures of (a) an electroluminescence device and (b) a down-conversion device based on QDs. ..... 24

**Figure 1.11** (a) EL spectra and device structures of two kinds of QD-LEDs without TAZ layer (left) and with TAZ (right) as a hole-blocking layer. Dashed lines represent the deconvolution of the EL spectra into $Alq_3$ and QD components. The QDs used are illustrated in the inset that is composed of CdSe core (~38 Å in diameter) coated with 1.5 monolayers of ZnS. PL QE was 22 ± 2 %. (b) An AFM phase image of a complete, hexagonally packed QD monolayer segregated from an underlying TPD layer. Grain boundaries between ordered domains of QDs are shown. (c) A proposed energy level diagram of an EL device shown on the left of (a). © 1998 Nature Publishing Group. .....25

**Figure 1.12** (a) Comparision of (left) commercial LEDs and (right) LEDs with additional converter materials. (b) Photograph of a white-LED with QDs at 1000 mA. .....26

**Figure 1.13** (a) TEM images of shape-controlled CdSe nanocrystals: dots (7 nm x 7 nm), short rods (7 nm x 30 nm) and long rods (7 nm x 60 nm) from the left. (b) External quantum efficiency and (c) the current-voltage

characteristics of photovoltaic devices comprising shape-controlled CdSe nanocrystals in (a). © 2002 AAAS. .....30

**Figure 2.1.1** (a) A schematic on the synthetic procedure of InP@ZnSeS QDs. (b) Temporal evolution of the atomic ratio of Se (Se / (Se + S)) during the shell growth in InP@ZnSeS QDs with n = 2. .....41

**Figure 2.1.2** Photoluminescence (PL) spectra for InP core only (solid line), InP@ZnS (dashed line), InP@ZnSe (dotted line), and InP@ZnSeS (bold green line, r = 0.05) solutions with n = 2. .....42

**Figure 2.1.3** (a) PL QEs after the termination of reaction for InP@ZnSeS QDs as a function of the amount of shell precursors (n) as well as the ratio of TOPSe (r) in the shell precursor solution. Dotted red circles represent the optimal points for r for a given n. (b) Temporal evolution in PL QE for InP@ZnS (filled triangles), InP@ZnSe (filled circles), and InP@ZnSeS QDs (open squares) with n = 2. .....45

**Figure 2.1.4** Temporal change in PL QE for InP@ZnSeS QDs as a function of the molar ratio of TOPSe (r) with (a) n = 1 and (b) n = 4. .....46

**Figure 2.1.5** TEM images of InP@ZnSeS QDs with (a, b) n = 1, (c, d) n = 2, and (e, f) n = 4 with optimal Se ratio (r). .....47

**Figure 2.1.6** The PL redshift of InP@ZnSeS QDs as a function of the molar ratio of TOPSe (r) with n = 4. .....51

**Figure 2.1.7** The effect of shell composition and thickness on QE against (a) UV irradiation in air (with 2 mW / $cm^2$ at 352 nm) and (b) ligand exchange with MPA. .....52

**Figure 2.1.8** The PL redshift of InP@ZnSeS@ZnS QDs as a function of the amount of shell precursors. To investigate the effect of shell thickness on the confinement of exciton wavefunctions, $Zn(OA)_2$ and TOPS precursors were sequentially added into the InP@ZnSeS QD solution (n = 1, r = 0.2) with a standard shell growth procedure. .....53

**Figure 2.2.1** (a) Ensemble absorption spectra of CdSe seeds (black) and CdSe tetrapods (red) prepared by the CPI approach. Distinct multiple excitonic features observed in absorption spectra support excellent uniformity of the arm diameter of prepared CdSe tetrapods. TEM images of at (b) 0 (seeds), (c) 10, (d), 20, (e) 30, (f) 40, and (g) 50 min of reaction elapsed. The inset in (g) is the final product obtained from a single batch of reaction. A coin in the picture is a US quarter. .....65

**Figure 2.2.2** A low magnification TEM image of CdSe tetrapods given in Figure 1b. Aggregates (black boxes) are excluded in the counting when we consider the shape selectivity of CdSe tetrapods. Yellow circles represent defective nanocrystals (i.e., dots, mono-, bi-, tripods, and tetrapods with short arms). .....66

**Figure 2.2.3** (a) A HR-TEM image of an arm region with a FFT pattern (inset). (b) Powder X-ray diffractograms of ZB CdSe seeds (red) and tetrapods with WZ-arms (blue), referenced to JCPDS 08-0459 for wurtzite CdSe as well as 19-0191for zincblende CdSe. .....67

**Figure 2.2.4** (a) Representative growth behavior of CdSe tetrapods (arm length (●) and diameter (■)) as a function of reaction time. Arm diameter was estimated from the excitonic transition absorption peak in correlation with

TEM images (Figure 2.2.5). (b) The effect of injection rate and reaction temperature on the aspect ratio of arms (L/D) obtained at 10 min of elapsed reaction. TEM images of (c) arm length-controlled CdSe tetrapods and (d) diameter-controlled CdSe tetrapods. (e) A TEM image of CdSe tetrapods with stepwise-varying arm diameter. The inset is a high magnification image of arm region. All the scale bars are 50 nm. .....69

**Figure 2.2.5** A plot of theoretical $\Delta E_g$ ($E_{g,\ tetrapod} - E_{bulk}$) values against arm diameter (d) of CdSe tetrapods. The tetrapods with long arms ranging from 20 nm to 50 nm were chosen to minimize the influence of central cores. Empirical least-squares fitting to the equation, $\Delta E_g = C / d^n$, gave $C = 1.60 \pm 0.02$ eV $nm^{1.36}$ with a fixed n of 1.36. .....70

**Figure 2.2.6** TEM images of CdSe nanocrystals obtained with: (a) ammonium bromide ($NH_4Br$), (b) tetrabutylammonium bromide (TBAB), (c) tetrabutylammonium chloride (TBAC), and (d) tetrabutylammonium iodide (TBAI). All the samples were prepared the same reaction condition (see Experimental Section) except for the halogen ion sources. .....73

**Figure 2.2.7** (a) Binding energies of 3d electron from Br, (b) 2p electrons from Cl and (c) $3d_{5/2}$ electrons from I, bound to CdSe tetrapods (red) and from TBAB, TBAC and TBAI (blue) measured by XPS. (d) Au 4*f* binding energies of the substrates used as an internal reference: TBAC (red, dashed line), Cl-bound CdSe tetrapods (red, solid line), TBAB (green, dashed line), Br-bound CdSe tetrapods (green, solid line), TBAI (blue, dashed line), and I-bound CdSe tetrapods (blue, solid line). .....75

**Figure 2.2.8** (a) The $^{1}H$ NMR peaks from the alkene protons of oleate ligands bound to spherical CdSe nanocrystals (denoted in the molecular structure), as a function of p, defined as CTAB / (OA + CTAB). A sharp peak at 5.19 ppm is due to impurities contained in methoxyacetone (served as a concentration reference, inset), contributing less than 1 % of the total integration area. (b) Temporal change in the average radius of CdSe dots (<r>) as a function of p at 240 $^{o}$C. (c) The effect of p on the aspect ratio of CdSe tetrapod arms (L/D) taken at 10 min of elapsed reaction. The inset in d) is the TEM image obtained at the highest p, denoted as an arrow. .....76

**Figure 2.2.9** A HR-TEM image of CdSe tetrapods at 100 sec of elapsed reaction and their fast Fourier transform (FFT) patterns at (b) ZB seed and (c) WZ arm region (denoted as dotted boxes). The ZB phase is viewed along a [001]-zone axis and the WZ phase is observed with a $[11\bar{2}0]$-zone axis. .....82

**Figure 3.1** (a) Absorption (open) and photoluminescence (filled) spectra of InP QDs with single (red), double ZnSeS shells (blue), and final QDs (green) (b) A TEM image of final InP QDs. Inset is a high-resolution TEM image of (b) (avg. d = 4.6 nm). .....92

**Figure 3.2** (a) Schematic on InP QLEDs based on the ZnO/PFN electron injection layer. (b) A HR-TEM image of InP QDs with optimal ZnSeS composition gradient shells (InP@$GS_2$). (c) Schematic energy-level diagrams near the ZnO/QD interface with and without the PFN layer. .....93

**Figure 3.3** AFM height images and water contact angle (inset) of ZnO/PFN thin films fabricated with (a) 0, (b) 0.5, (c) 1.0, and (d) 1.5 mg $mL^{-1}$ of PFN solutions. .....94

**Figure 3.4** (a) High binding energy cutoff region in UPS spectra of a bare ZnO film and PFN-coated ZnO films. Inset is a trend on vacuum level shift (Δ) varied by concentrations of PFN solutions. All spectra are referenced to the Fermi energy level of Au (111) surface. (b) *J*-*V* and *L*-*V* characteristics of QLEDs as a function of the concentration of PFN solution. Inset is turn-on voltages of QLEDs as a function of vacuum level shift. (c) EQE-*J* characteristics of QLEDs varied by the concentration of PFN solution (closed markers with solid lines) and the number of ZnSeS composition gradient shells (n) of QDs (open markers with dashed lines). .....96

**Figure 3.5** (a) Normalized EL spectra of InP QLEDs comprising of InP@$GS_2$, as a function of current density (*J*). (b) A demonstration of large-area InP QLEDs on flexible polyethersulphone (PES) substrate (pixel size: 1.2 cm x 1.2 cm) at 5.5 V of applied bias. .....98

**Figure 4.1** (a-c) TEM images of CdSe tetrapods with controlled arm length and diameter. (d) Absorption spectra of CdSe tetrapods shown in (a-c). ....115

**Figure 4.2** (a) A schematic on two-step ligand exchange of CdSe TPs. (b) FT-IR spectra of CdSe TPs with repeating $HBF_4$ treatment. (c) TGA curve of pristine and $HBF_4$-treated CdSe TPs. (d) Absorption spectra of pristine and modified CdSe TPs in chloroform. .....118

**Figure 4.3** (a) A schematic on the fabrication of porous CdSe TP thin films. Top (top) and cross-sectional SEM images (bottom) of final CdSe TP thin films comprising of (d) 40 nm, (e) 76 nm, and (f) 103 nm of arm length. All scale bars are 500 nm. .....121

**Figure 4.4** (a) Absorption spectra of a ZnO (open blue circle), a ZnO/CdSe tetrapod (open red square), a ZnO/CdSe tetrapod:P3HT thin film (closed black dot), and a ZnO/CdSe tetrapod thin film acquired from ZnO/CdSe tetrapod:P3HT thin film, rinsed with chloroform. (b) Depth profiles Si, S, Zn, and Cd in ZnO/CdSe tetrapod:P3HT BHJ thin films taken by Auger electron spectroscopy. Samples in (a) and (b) were assembled with the TPs with 76 nm of arm length. Cross-sectional SEM images of ZnO/CdSe TP:P3HT thin films comprising of the TPs with (c) 40 nm, (d) 76 nm, and (e) 103 nm of arm length (scale bar: 200 nm). .....123

**Figure 4.5** (a) Current density (J) – voltage (V) characteristics, (b) Incident photon-to-current conversion efficiency (IPCE), and (c) light intensity dependence of short circuit current density of CdSe TP:P3HT BHJ solar cells comprising of CdSe tetrapod without surface ligands (black), passivated with hexylamine (red), pyridine (blue), hexanoic acid (yellow), hexanethiol (green). Dotted lines in (c) denote fitting line according to $J_{sc} \sim (I_{light})^{\alpha}$. The arm length of tetrapods was fixed to 76 nm and the thickness of CdSe TP:P3HT thin film was 230 nm. .....126

**Figure 4.6** (a) J-V characteristics and (b) IPCE curves of optimized CdSe TP:P3HT BHJ solar cells (Arm length / active layer thickness: 40nm / 190 nm for blue, 76 nm / 200 nm for green, and 103 nm / 210 nm for red). .....129

# List of Schemes

**Scheme 2.1.1** A schematic illustration on the CPI approach. .....58

**Scheme 4.1** (top) A schematic on a device structure of CdSe tetrapod:P3HT bulk heterojunction (BHJ) solar cells and (bottom) energy level diagram of CdSe Tetrapod:P3HT BHJ solar cells with an inverted device structure. ...113

# Chapter 1. Introduction

## 1.1 Fundamental properties of semiconductor nanocrystals

Since colloidal semiconductor nanocrystals were prepared by L. E. Brus et al.,[1] semiconductor nanocrystals have attracted keen attention due to their unique optical and electronic properties, such as facile bandgap tunability, wide absorption range, narrow emission bandwidth, and photo-/chemical-stability.[2-5] Particularly, combining two or more semiconductor materials and manipulating their shape enable us to manipulate photons or electrons in nanoscale: up- or down-conversion of photons, photocarrier generation or control in transport of carriers in nanometer scale. Moreover, hybridization of those semiconductor nanocrystals with the other functional materials such as conducting polymers or metal nanoparticles opens unprecedented opportunity in utilizing their full potentials in energy conversion and generation. Because of their distinguishable physical and chemical properties as well as potential applications to novel optoelectronic devices, the semiconductor nanocrystals can be regarded as the nanoscale toolbox for forthcoming novel optoelectronic devices based on nanosciences.

The physical property of semiconductor nanocrystals is mainly determined by their size and shape, which have never been observed in bulk materials. In the case of bulk semiconductors, electrons are excited vertically to the “continuous” conduction band when semiconductors absorb photons with higher energy than the bandgap of materials (Figure 1.1a, left), and, thus,

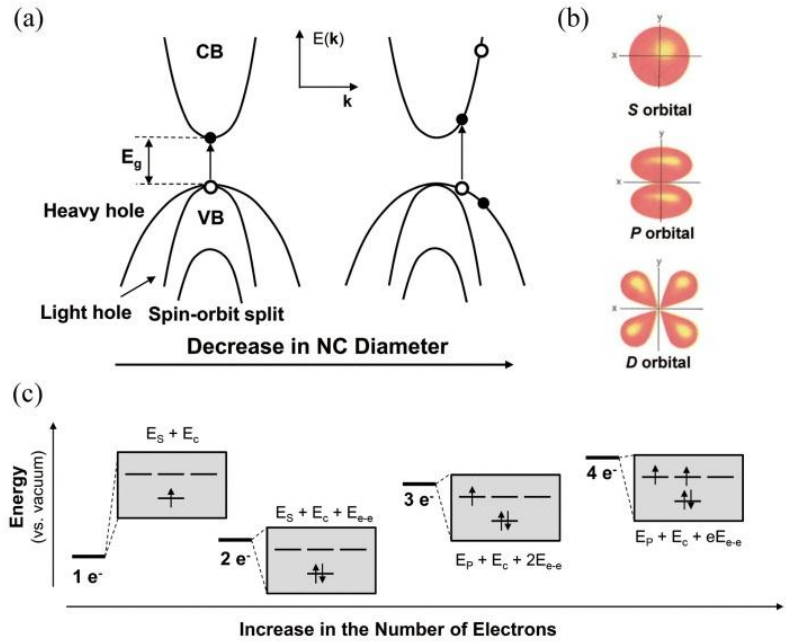


**Figure 1.1** (a) The band structure for bulk semiconductor and nanocrystals with cubic lattice around **k** = 0. This illustration is reconstructed from C. B. Murray et al.[3] (b) Atom-like S, P, and D orbitals of spherical semiconductor nanocrystals. Reprinted from D. V. Talapin et al.[5] with permission. © 2009 American Chemical Society. (c) A schematic on building up of electrons in a strongly-confined spherical semiconductor nanocrystals ($E_S$: single-electron energy level; $E_C$: charging energy; $E_{e-e}$: Coulomb repulsion). This illustration is redesigned from D. Vanmaekelbergh, D et al.[6]

the absorption spectrum of a bulk semiconductor shows monotonous and continuous increase above the optical bandgap energy of materials. However, if the spatial dimension of materials is reduced, the wavefunction of charge carriers (i.e., electron and hole) is spatially restricted (dimension = a), and the allowed wavenumbers for the optical transition, $|\mathbf{k}|=2\pi/\lambda$, gets quantized to discrete states which only satisfy the boundary condition (Figure 1.1a, right). This effect, the quantization of electronic structure in nanometer regime, is referred as the quantum confinement effect. The quantum confinement effect is highly distinguishable feature compared with organics or metals with nanometer dimension, so thus, the semiconductor nanocrystals are commonly named as quantum dots (QDs), quantum rods (QRs) or quantum wires (QWs), according to their shape. In a case of QDs, at the strong confinement regime where the physical size of QDs are smaller than the bulk Bohr exciton size ($a < a_B$), the electron and hole wavefunctions of QDs are described by hydrogen atom-like symmetry, named as S, P, and D electronic states with 2-, 6-, and 10-fold degeneracy (Figure 1.1b and 1.1c). Because of these similarities in electronic features with hydrogen atom, QDs are frequently described as artificial atoms.

Colloidal QDs have been normally synthesized by thermal decomposition of organometallic precursors in hot reaction medium. In common synthetic methods, anionic precursors are rapidly injected into solution containing cationic precursors at elevated temperature, so-called as hot injection method (Figure 1.2a, left). The hot injection method facilitates the instantaneous supersaturation of reactant over critical point for nucleation

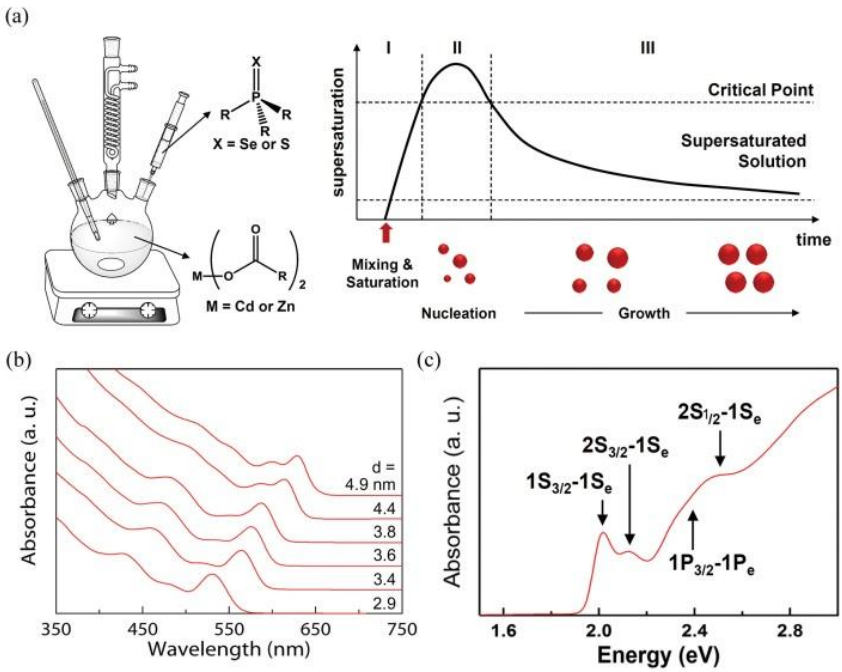


**Figure 1.2** (a) (left) A schematic on conventional hot-injection method for group II-VI QDs. (right) The temporal change in degree of supersaturation (The LaMer plot). Rapid injection of precursors (region I) results in sudden supersaturation over critical point, resulting in burst nucleation of QDs (region II). In following period, QDs grow to finite size (region III), depending on the reaction parameters. (b) Size-dependent optical spectra for monodisperse CdSe QDs. (c) An absorption spectrum of CdSe QDs and the manifolds of excitonic states.

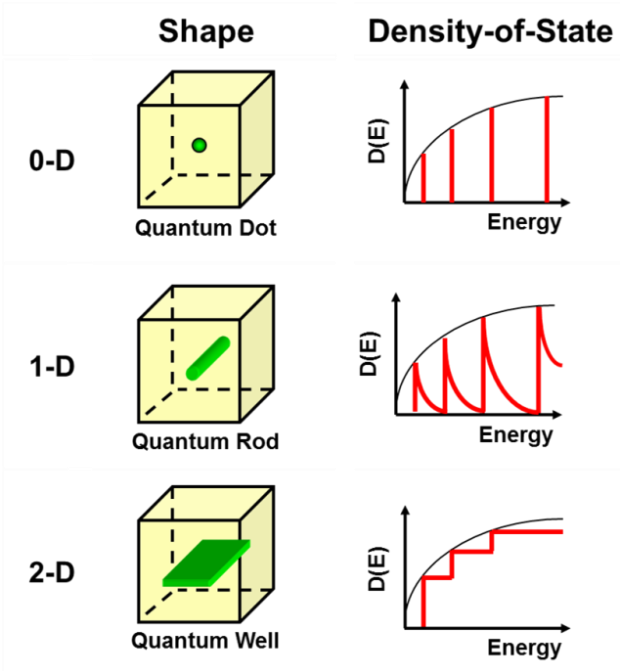


**Figure 1.3** Schematic illustrations of various dimensional materials (left) and corresponding density of states (right).

in very short period, which results in the monodisperse QDs during growth period (Figure 1.2a, right). Nucleation and growth kinetics depend on the reactivity of precursors, reaction variables (i.e., temperature and concentration), and surfactants (i.e., fatty acids, fatty amines, alkylphosphonic acids, or trialkylphosphine or trialkylphosphine oxides), and their mechanical aspects have been finely resolved by H. Weller, P. A. Alivisatos, or X. Peng.[7-12]

The quantized electronic states of monodisperse QDs are easily observed in optical transitions. The absorption edge and excitonic transition energy of QDs shift to a higher energy as the size of QD decreases (Figure 1.2b). The size-dependent energy trace follows the quantum confinement effect of charge carriers and, thus, can be described as a function of $1/a^2$. Another representative size-dependent feature of QDs is the wavy and continuous signature in the extinction coefficient (Figure 1.2c), which reflects the density of state participating in the electronic transition from a ground state to excited states (i.e., $1S_{3/2}$-$1S_e$ at the first peak implies that the electron is excited from $1S_{3/2}$ valence band to $1S_e$ conduction band)[13]. In the meantime, the electronic structure of QDs can be additionally altered by changing the dimensionality of nanocrystals. For instance, elongation in one direction (QRs) only represents quantum confinement effect in radial direction (x, y-direction) and the bandgap is mostly governed by a radius of QRs. And the light absorption is largely increased as a function of the length of rod, which contributes an increase in the density of state (Figure 1.3).

In addition to the electronic structure, the shape control of semiconductor nanocrystals also affects the carrier dynamics and transport phenomena in separated one or nanocrystal assembly. For instance, recombination process of photo-generated exciton wavefunctions is quite different between 0-D (dots) and 3-D (i.e., tetrapods) system. For the 0-D system, electron and hole wavefunctions are highly overlapped in confined space even at highly excited states, causing radiative recombination with high probability. Compared with such 0-D system (Figure 1.4a, left), the formation of multiple branches in every direction (Figure 1.4a, right) results in the spatial distribution of exciton wavefunctions and induces nonradiative process (i.e., surface state-induced nonradiative decay or exciton dissociation at interface with other semiconductor materials) rather than radiative recombination process (Figure 1.4b). In a case of carrier transport in a nanocrystal assembly, the elongated nanocrystals serves more effective carrier transport pathway based on conduction mechanism rather than hopping mechanism of quantum dots (Figure 1.4c).

Summing up the statement above, the optical and electronic properties of semiconductor nanocrystals can be controlled by their size as well as shape, varying quantum confinement effect and spatial distribution of exciton wavefunctions. For the practical utilization of semiconductor nanocrystals to optoelectronic devices, the chemical (for proper bandgap size and position) and structural factor (0-D, 1-D, 2-D or 3-D shape with controlled size) should be carefully regarded for the final purpose. In a following section, chemical and structural design of semiconductor

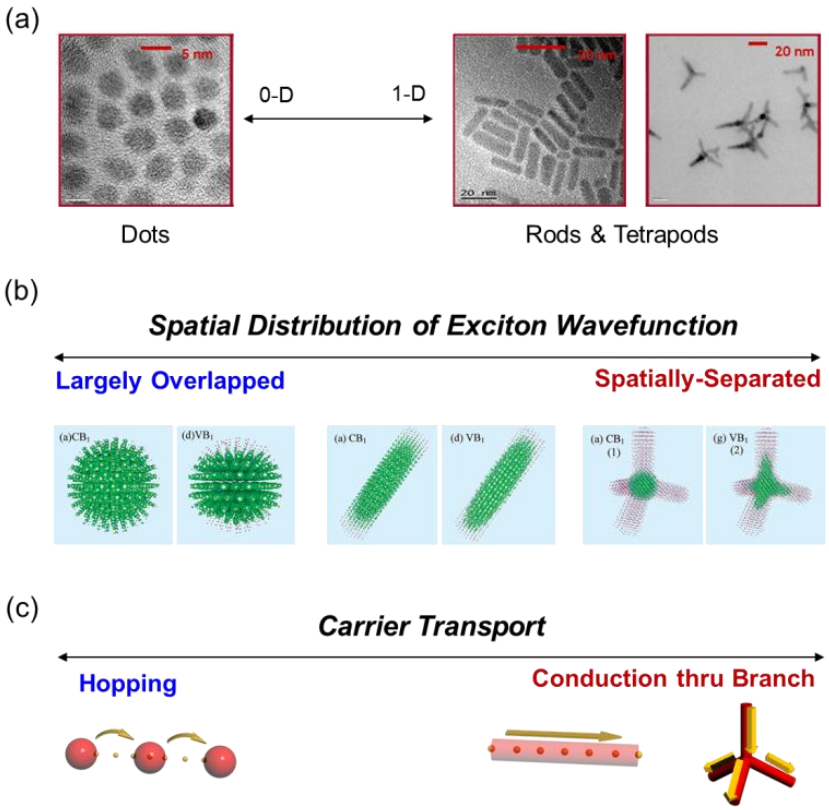


**Figure 1.4** (a) Representative shape variation of CdSe nanocrystals, from dots (0-D), rods(1-D) and tetrapods (3-D). (b) Spatial distribution of electron and hole wavefunction in various nanocrystal shape. Reprinted from J. Li et al.[14] with permission. © American Chemical Society. (c) Carrier transport mode in semiconductor nanocrystals.

nanocrystals for optoelectronic devices light generation (LEDs) or electricity generation (solar cells) will be discussed with the important milestone in academic area.

## 1.2 Design principle of semiconductor nanocrystals for optoelectronic devices

Among the unique physical and chemical properties of semiconductor nanocrystals, optical and electronic properties have been regarded as the most distinctive features compared with conventional materials, so the optoelectronic devices based on such nanomaterial have been ceaselessly researched. In terms of optical properties, particularly, the semiconductor nanocrystals possess highly narrow emission spectrum and their emission wavelength is tunable by adjusting the size and the chemical composition (i.e., from binary compounds to quaternary alloy). Because of these reason, in the early stage, the semiconductor nanocrystals have been mainly utilized in light emitting diodes[15-20] or biomarkers[21-25] requiring wide excitation range, narrow emission bandwidth and photostability. In the meantime, the wide and continuous absorption as well as excellent conducting property of semiconductor nanocrystals have been also paid attention to the photovoltaic applications since early 2000's.[26-31] By employing semiconductor nanocrystals as n-type or p-type materials, it is found that they successfully generate photo-generated carriers via exciton dissociation, and transport charged carriers in effective way. These two approaches, generating light or electricity, are the major applications based on the unique optical and electronic properties of semiconductor nanocrystals and the other applications such as photodetectors,[32-33] nanoscopic pressure sensor,[34] or water splitting materials[35] have been vigorously studied to date.

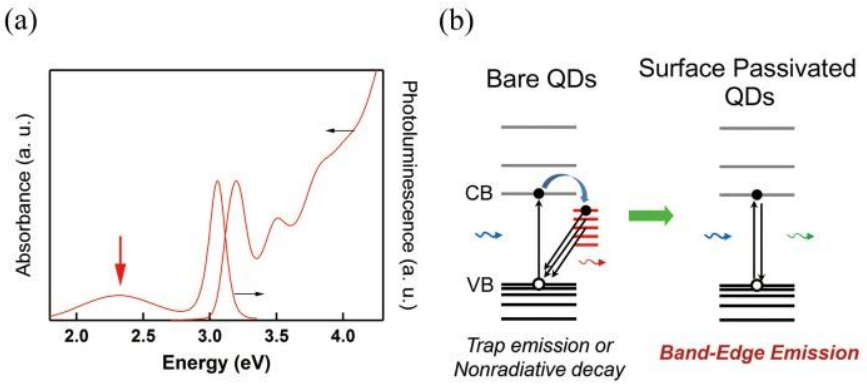


**Figure 1.5** (a) An absorption and photoluminescence spectrum of CdS QDs. The trap emission is denoted as a red arrow. (b) Schematics on the effect of surface states on the recombination process. The band structure as a function of **k** and the other relaxation processes are omitted for the simplicity.

Although both light generation (LEDs) and electricity generation (solar cells) using the semiconductor nanocrystals have been researched on a same background, the requirement for such opposite energy conversion process is quite different.

For the effective generation of photons by incident light or charged carriers, the radiative recombination process of excitons have to occur before undesired nonradiative process. In the viewpoint of nanocrystal shape, QDs are suitable to facilitate the radiative recombination process by maximizing the overlap between electron and hole wavefunctions. The monodispersity of QDs is also major requirement to produce a narrow emission spectrum. In common, Gaussian-shape spectrum (from 250 to 60 nm in full-width at half-maximum) is observed from colloidal QDs and low size distribution ($\sigma$ < 5 %) yields narrow spectral bandwidth below 35 nm.

Based on the spherical geometry, it is found that the core/shell formulation improves the quantum efficiency of QDs by eliminating surface states on nanocrystals. Figure 1.5a is a common absorption and emission spectrum of CdS QDs measured at room temperature. Although the absorption spectrum with well-resolved excitonic transition features signifies narrow size and shape distribution of QDs, the emission spectrum shows a sharp band-edge emission and unexpected broad emission at lower energy than the band-edge PL energy (denoted with a red arrow in Figure 1.5a). This broad PL is known as surface trap emission or surface state emission. If the surface states are not passivated (left, bare QDs), an electron at the conduction band edge can be trapped at the surface states, resulting in a broad and weak surface state

emission or nonradiative decay. On the other hand, if the surface states are passivated by organic or inorganic shells, then the trap emission is eliminated and only band-edge emission is occurred. The QDs with surface state emission typically possess poor PL QE (below 5 %) compared with the one with solely band-edge emission due to the non-radiative relaxation process through the surface states.

There are two general approaches to passivate the surface states of QDs for the enhanced QE and improved photochemical stability: 1) passivating surface dangling bonds with organic ligands or 2) passivating surface states with inorganic shells. Although the surface passivation with organic ligands is generally simple and straightforward (i.e., addition of ligands into QD solution), the organic capping is vulnerable to external stresses. For instance, primary amines, which efficiently passivate the hole trap states in CdSe QDs, are easily desorbed from the surface by adsorption-desorption equilibrium[36], and, thus, it does not guarantee reliable QE over time. Moreover, the addition of other organic ligands or solvents may change the areal density of original ligands on surface (i.e., thiols, frequently used functionality for surface modification), and easily affects the PL QE of QDs.[37]

In order to enhance the reliability and stability of QE, the surface passivation with inorganic shells has been developed. This structural engineering of QDs in a core/shell formulation is regarded as a major advance in QD synthesis, because it provides robustness and tolerance to QDs against

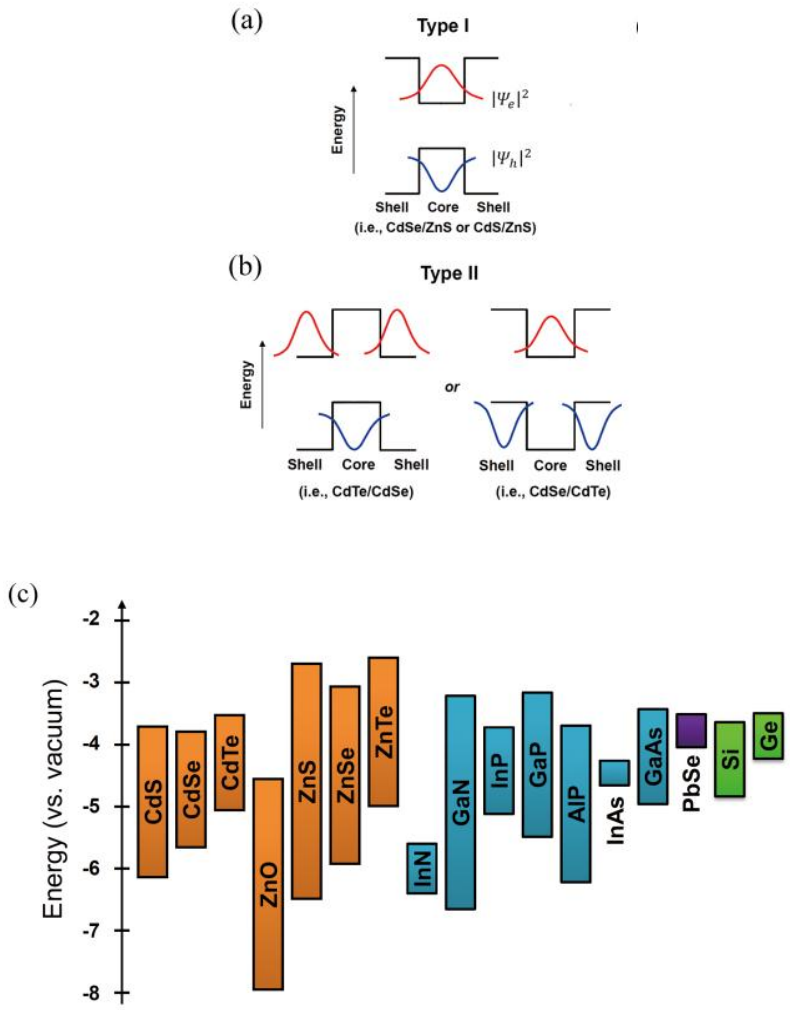


**Figure 1.6** Schematics on (a) a type-I bandgap configuration and (b) type-II bandgap configurations. (c) Electronic energy levels of several group II-VI, III-V, IV-VI, VI semiconductor materials using the valence-band offsets from reference [38], [39].

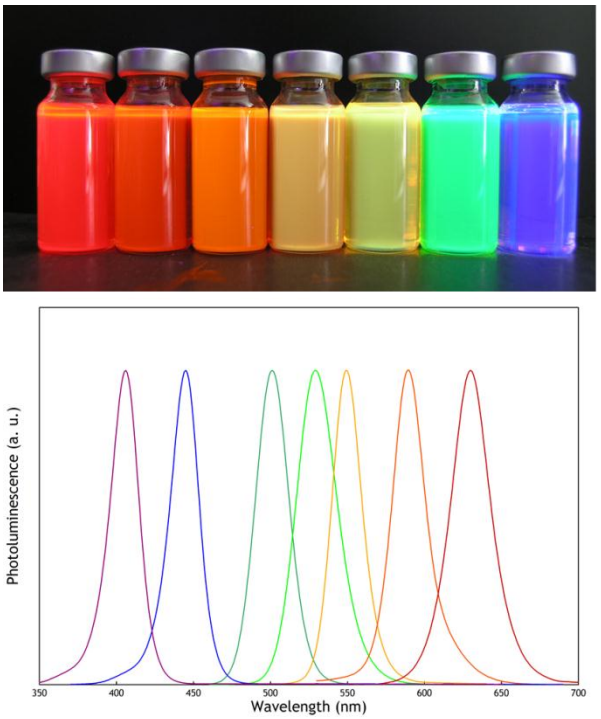


**Figure 1.7** (top) A picture of core/shell structured II-VI QD dispersions illuminated under UV irradiation (352 nm) and (bottom) representative emission spectrum.

physical and chemical stresses enabling QDs applied to various research fields. Ever since A. R. Kortan et al. firstly suggested the CdSe/ZnS core/shell QDs synthesized in inverse micelle media[40], numerous efforts have been followed to realize the core/shell structured QDs with high QE and stability.

The luminescent property of core/shell structured QDs can be engineered with relative position of core bandgap and shell bandgap. If core QD with a smaller bandgap is located within shell material with a larger one, the electron and hole wavefunctions are confined into core (type-I bandgap configuration, Figure 1.6a). In this case, the recombination probability of two wavefunctions increases while the non-radiative decay process via surface states decreases, and, thus, the PL QE of QDs increases. By contrast, if two bandgaps are staggered (type-II bandgap configuration, Figure 1.6b), then two wavefunctions are spatially dissociated and the energy from radiative decay are determined by the difference between spatially-different energy levels, which is smaller than the bandgap of the core or shell. The type-II bandgap configuration give a huge opportunity to manipulate exciton recombination or dissociation process, so it is a strong candidate for photovoltaic applications [41]. From the QD-LED perspectives, type-I bandgap configuration is favored, and various types of semiconductor materials are realized in core-shell structures with type I configuration,[42-45] such as CdSe/CdS,[43] CdSe/ZnS, CdSe/ZnSe/ZnS or CdSe/CdS/ZnS.[46] The information (i.e., bandgap and the electronic energy levels) for group II-VI, III-V and II-VI semiconductors are depicted in Figure 1.6c[38], [47] More recently, the core/shell structures of QDs are more advanced for highly efficient and color-saturated QDs (Figure 1.7);

ternary[48-50] or quaternary alloy core[51] ensures the extended controllability in emission wavelength, and homogeneous alloy[52] or composition gradient shell[53] was invented to synthesize highly luminescent and stable QDs in simple manner.

Although the advances in the synthesis of group II-VI QDs provide a positive outlook, the hazardous chemical components (i.e., Cd or Pb) hamper the commercialization of QDs-based applications. In order to avoid such harmful substance, the research on group III-V QDs (i.e., InP-based QDs) is accelerated. Unfortunately, the current status of III-V QDs is still embryonic level and the technological advances for these materials are not matured. However, the physical background and the synthetic approaches to improve QE and stability are similar with these of group II-VI QDs. Recent progress on the development of InP/GaP/ZnS core/shell/shell QDs[54], composition gradient InP/ZnS QDs[55], or InPZnS alloyed QDs[56] supports such prospective. Novel synthetic strategy for size-controlled, monodisperse, and surface-passivated core/shell QDs will raise the possibility of non-toxic group III-V QDs.

In the meantime, light harvesting and electricity generation using semiconductor nanocrystals requires the exact opposite way: the geometry delocalizing electron and hole wavefunctions,[14] small bandgap semiconductors, and insulating ligand-free surface. As mentioned in chapter 1.1, the elongated semiconductor nanocrystals (i.e., rod or tetrapods) serve the space for delocalization of wavefunctions and such delocalization is dominantly occurred at high electronic states. Because of those reason, the

rods, tetrapods, or hyperbranced morphology consisting of CdSe or CdTe has been synthesized for building blocks in organic-inorganic hybrid solar cells,[26-31] due to their small bandgap covering visible (for CdSe) or near IR (for CdTe) region.

From the thermodynamic viewpoint, the anisotropic nanocrystals (Figure 1.8b) are unstable system. In a nanoscale, the surface energy term largely contributes the overall Gibbs free energy of nanocrystals, because of the large surface to volume ratio (Figure 1.8a). Therefore the nanocrystals tends to decrease surface area to minimize overall energy, namely, spherical shape is favored. In this context, the nanocrystals with non-spherical shape is not thermodynamically favored and trapped at metastable states. In order to synthesize anisotropic nanocrystals, so thus, delicate control in reaction kinetics and quenching are required to fix anisotropic shapes.

The formation of shape-controlled semiconductor nanocrystals can be classified into three major approaches: seed-mediated solution-liquid-solid growth (Figure 1.9a),[57] oriented attachment (Figure 1.9b),[58] and kinetically-controlled anisotropic growth (Figure 1.9c).[58] The seed-mediated solution-liquid-solid (SLS) growth creates inorganic nanowires such as Si or Ge on metal seeds by supersaturation and expel of semiconductors on a seed surface (Figure 1.9a). This approach is useful to prepare nanowires comprising of IV [57],[59] or III-V[60-61] [62] semiconductors. In a case of oriented attachment, for ZnO,[63] ZnS,[64] $TiO_2$[65] or PbSe,[66] the multiple isotropic nanocrystals are rearranged to reduce surface energy of specific facets and form various

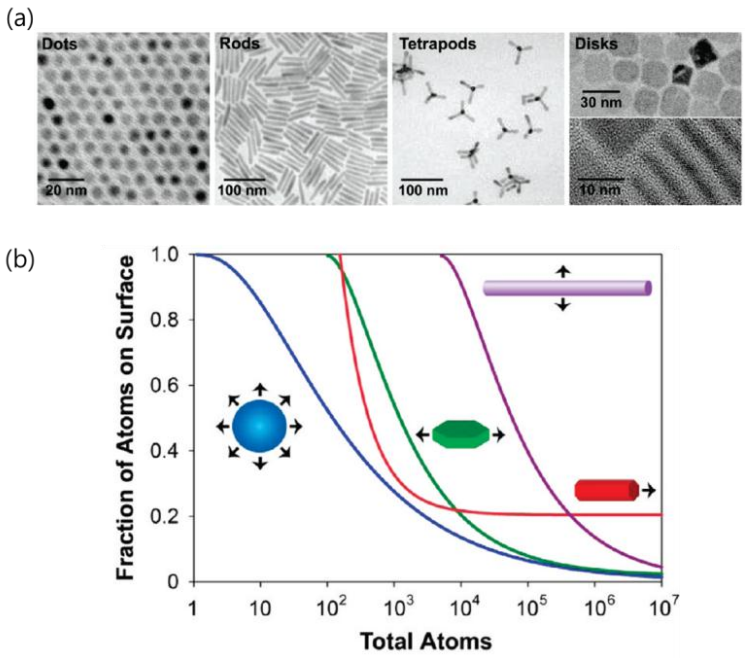


**Figure 1.8** (a) TEM images of representative shape-controlled CdSe nanocrystals. (b) Fraction of atoms on the nanocrystal surface as a function of the total number of atoms. The wires (purple) are 1 μm in length, the disks (green) are 20 nm in length, and the rods (red) are 4 nm in diameter.[4] © 2009 American Chemical Society.

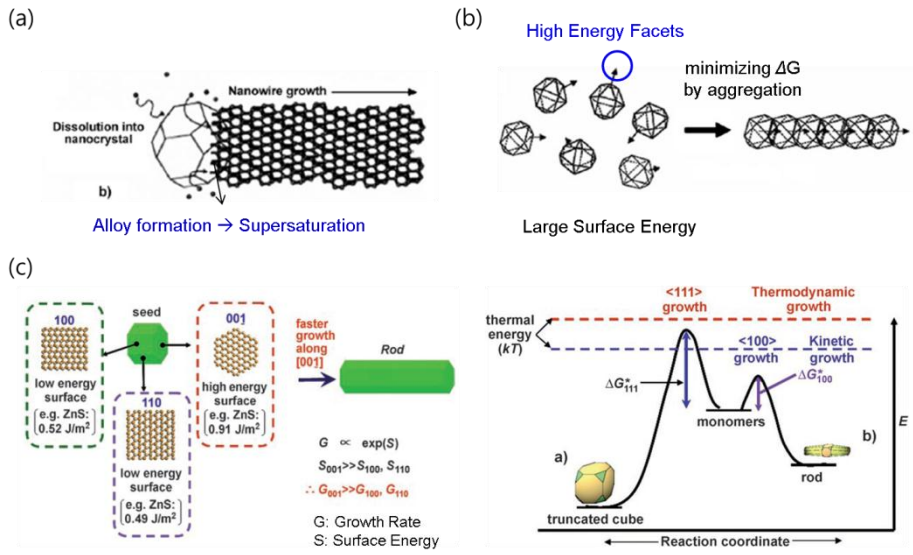


**Figure 1.9** (a) A schematic on solution-liquid-solid growth process. [57] (b) A schematic of oriented attachment process.[58] (c) (left) Surface energy of wurtzite ZnS nanocrystals, where (00$\underline{1}$) facet has the highest surface energy. (right) Comparision of thermodynamic and kinetic growth of PbS nanocrystals. At high temperature above two activation energy barrier, the formation of thermodynamically-stable truncated cube is preferred. At low temperature, the kinetic process causes a rod shape.[58] © 2006 Wiley-VCH.

anisotropic shapes according to their arrangement. Although the oriented attachment can easily prepare the anisotropic nanocrystals, the large size and shape variations are disadvantageous to exploit shape-controlled nanocrystals on optoelectronic applications.

The kinetically-controlled anisotropic growth is widely utilized for metal chalcogenide nanocrystals with anisotropic shapes (i.e., rod, branched shape or dendritic shape). The anisotropic nanocrystals synthesized by this approach originate from the reactivity difference of each crystal facets (Figure 1.9c, left), and high concentration level and selected reaction temperature (Figure 9c, right) initiates the anisotropic growth on high-surface energy facets. A term, kinetically-controlled growth, comes from their growth behavior determined by reaction kinetics. Based on this principle, employing site-selective ligands widens the diversity of shapes (i.e., rods, tetrapods, dendritic shapes) as well as spatial variation in chemical compositions (i.e., $rod_A$-$rod_B$-$rod_A$ or $core_A$/$arms_B$).[67]

Cadmium chalcogenides are considerable example on the shape control based on the kinetically-controlled anisotropic growth. Cadmium chalcogenides have two polymorphs: zincblende and wurtzite crystal phase. Such crystal structure can be selectively synthesized by adjusting reaction temperature and surface ligands, for instance, fatty acid commonly derives zincblende crystal phase and fatty amine or alkylphosphonic acid induces wurtzite ones. Between two polymorphs the wurtzite phase shows anisotropic growth behavior along [0001]-direction under kinetic growth environment, so that pure wurtzite nanocrystals can be grown to rod-shaped nanocrystals.

Moreover, if the zincblende nanocrystals are used as seeds and wurtzite arms are grown, then tetrapod-shape nanocrystals are synthesized. Based on this strategy, rod or tetrapod-shape nanocrystals with one or more chemical compositions have been successfully prepared and employed into various optoelectronic applications such as photodetectors,[32-33] nanoscopic pressure sensor,[34] or water splitting materials.[35]

The elimination of insulating ligands is also critical for successful exciton dissociation in semiconductor nanocrystal-based solar cells. In the semiconductor nanocrystal-based solar cells, the nanocrystals serve the carrier transport pathway by hopping mechanism. Under this mechanism, the insulating ligands on nanocrystals, introduced during chemical synthesis of semiconductor nanocrystals, acts as tunneling barrier for the wavefunction overlap between nanocrystals.[6, 68] Moreover, insulating ligands also hamper effective exciton dissociation at donor-acceptor or schottky junction interface. Recent publications using CdSe QDs as n-type acceptor in organic-inorganic hybrid solar cells show that the successful elimination of insulating surface ligands can largely improve photovoltaic performance even for spherical semiconductor nanocrystals.[69-70] Currently this finding is successfully applied to IV-VI QDs (i.e., PbS, PbSe, or PbTe) for all-inorganic solar cells covering IR region.[36, 71-74]

## 1.3 Applications of shape-controlled semiconductor nanocrystals

Shape-controlled semiconductor nanocrystals have been ceaselessly developed and optimized for the final applications. And several representative results in academia have already demonstrated the optimistic prospects of those materials for novel and unprecedented optoelectronic devices. In this section, some important results based on shape-controlled semiconductor nanocrystals will be briefly addressed and figured out the advantageous feature of semiconductor nanocrystals for them.

### 1.3.1 Quantum dot-based light emitting diodes (QD-LEDs)

QD-LEDs can commonly be classified as electroluminescence (EL) devices or down-conversion devices. The down conversion LEDs utilizes QDs as phosphors that converts part of high energy incident photons originating from substrate LEDs into lower energy ones (Figure 1.10b). For commercial applications, green and red-emitting QDs are dispersed in optically clear and thermally stable polymeric resins and those composite resins are deposited on top of blue-emitting LEDs to produce white light consisting of three discrete colors with high color purity (Figure 1.12). Several companies such as Nexxus Lighting, LG, or Samsung are now trying hard to adopt those passive devices in conventional liquid crystal displays as back light units. In contrast to down-conversion LEDs with single-phase QD composites, QD EL devices require multilayered device structures stacked with other semiconducting materials (i.e., hole transporting layer (HTL) or electron transporting layer (ETL)) in between electrodes (Figure 1.10a) for balanced and efficient

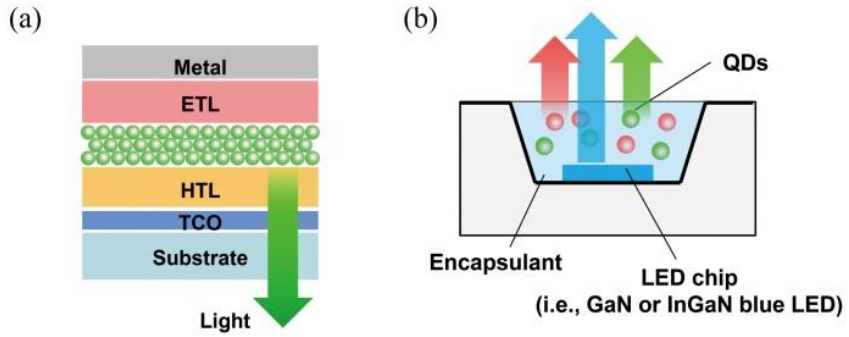


**Figure 1.10** Schematics on simplified device structures of (a) an electroluminescence device and (b) a down-conversion device based on QDs.

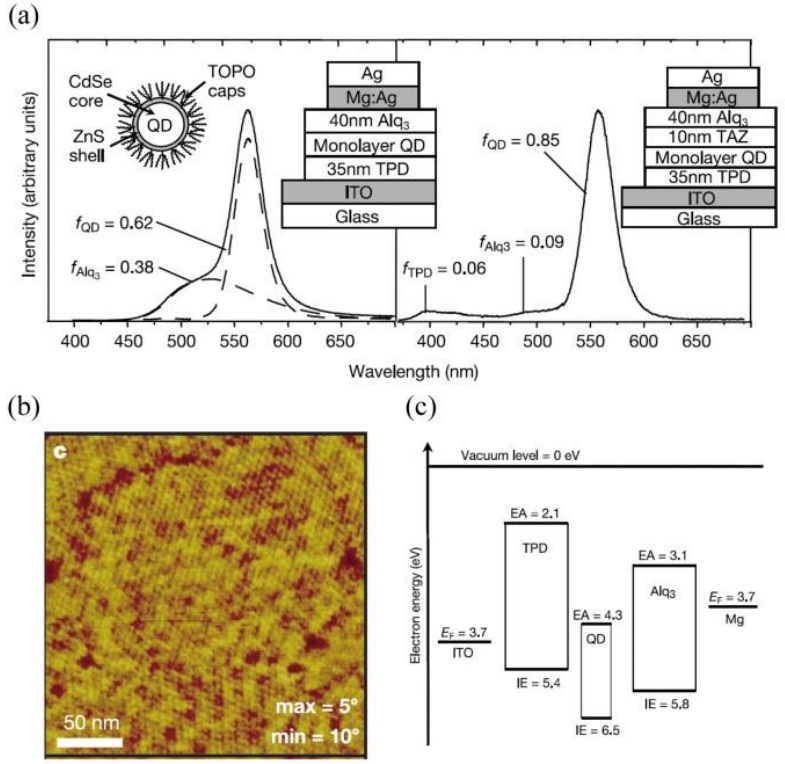


**Figure 1.11** (a) EL spectra and device structures of two kinds of QD-LEDs without TAZ (left) and with TAZ (right) layer as a hole-blocking layer. (b) An AFM phase image of a complete, hexagonally packed QD monolayer segregated from an underlying TPD layer. (c) A proposed energy level diagram of an EL device shown on the left of (a). Reprinted with permission from M. G. Bawendi et al. [75]. © 1998 Nature Publishing Group.

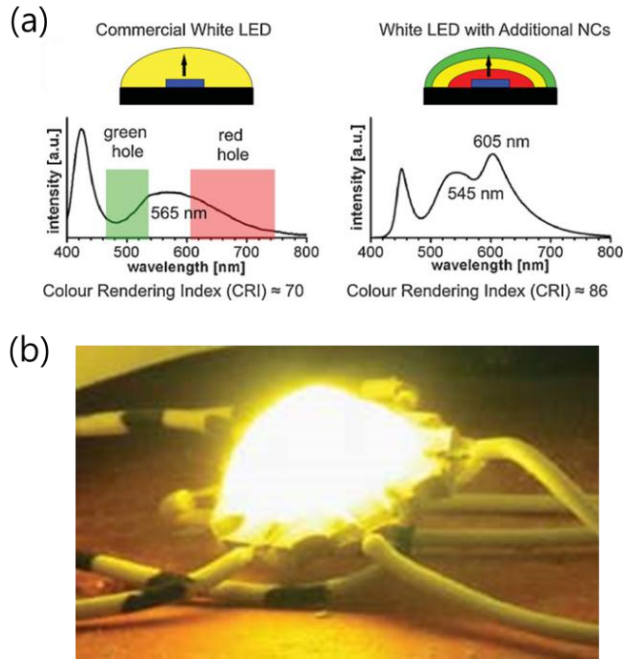


**Figure 1.12** (a) Comparision of (left) commercial LEDs and (right) LEDs with additional converter materials. (b) Photograph of a white-LED with QDs at 1000 mA. [76]

carrier injection into QDs.

The first QD-LEDs employed the multilayered structure of ITO as the low work-function cathode, conjugated polymer (poly(p-phenylenevinylene) (PPV)) as a hole transporting layer (HTL), CdSe QDs as emitting materials, and Mg as a low work-function cathode (ITO/PPV/CdSe QDs/Mg).[15] They displayed electroluminescence spectra clearly recognized as contributed by CdSe QDs, but device performance was not promising (i.e., EQE: 0.001 ~ 0.01 % and luminance: ~ 100 cd/$m^2$). Although material developments (i.e., CdSe/CdS[16] or CdSe/ZnS QDs[77]) improved both brightness by 10-fold of luminance and EQE up to 0.22 % in the same device structure, the QD-LEDs still suffered from low PL efficiency and stability and the parasitic EL spectra contributed by PPV layers. This poor device performance is mainly attributed to the imbalanced carrier injection and recombination of excitons.

The QD-LEDs containing HTL and ETL for balanced carrier injection was firstly realized by S. Coe et al[75]. They utilized N,N'-diphenyl-N,N'-bis(3-methylphenyl)-(1,1'-biphenyl)-4,4'-diamine (TPD) as HTL and (tris-(8-hydroxyquinoline)aluminium) ($Alq_3$) as ETL (ITO/TPD/QD/$Alq_3$/Mg) (Figure 11a). Their device structure (HTL/QD/EBL/ETL, EBL: electron blocking layer) demonstrated a significant improvement in QD-LEDs; they, for the first time, suggested the complete device structure to facilitate the carrier injection into QDs or the efficient Förster type energy transfer from neighboring organic layers to QDs and the recombination in the emission layer. In order to realize the multilayered device structure, they took

advantage of the phase segregation of QDs from organic molecule layer (i.e., TPD) for the HTL/QD layers, followed by consecutive thermal evaporation of EBL/ETL/cathode layers. Because of low miscibility between TOP/TOPO-capped QDs and TPD layers, QDs are excluded from the TPD matrix layer and migrate to the top surface with closely-packed morphology (Figure 1.11b). Although the QD monolayer realized in this report has several defects, causing parasitic emissions from the TPD layer, the introduction of a thin electron blocking layer (TAZ, 10 nm) considerably reduced the emission from organic layers (Figure 1.11c). As a result, this first complete device led to the significant improvement in terms of peak EQE (0.52 % at 10 $mA/cm^2$) and luminous efficiency (1.6 cd/A at 2000 $cd/m^2$), which was the 25-fold improvement compared with previously reported QD-LEDs.

After their demonstration of electroluminescence devices based on multilayered structures, rapid improvement in device structure and efficiency has been achieved after around 2000. The QD-LEDs reported in the recent publications already satisfy the minimal requirements for full-color displays (i.e., 100 ~ 500 $cd/m^2$ for mobile displays, over 1000 $cd/m^2$ for TVs) and color purity (FWHM below 40 nm). Moreover, the recent progress in EQE is breath-taking: the rapid increase in EQE reported by industry (i.e., QD Vision Inc.) and academia. Particularly, EQEs of red QD-LEDs are rapidly approaching to the 20 %, which is a theoretical limitation with the assumption of 20 % of extraction efficiency. Although green and blue QD-LEDs are still far from the commercialization level, rapid increase in EQE represents bright future of QD-LEDs for practical devices.

Because of the bright future of QD-LEDs, industries such QD Vision and Samsung Electronics have already paid keen attention to materials, device structures, and processing techniques involved in QD-LEDs to realize QD-based displays. Recently, they demonstrated mono- or full-color active matrix QD displays processed by the contact printing method.

### 1.3.2 Semiconductor nanocrystal-based photovoltaic devices

Recently, multilateral approaches on light absorbing materials, device structures, and economic fabrication processes have been attempted to realize highly efficient photovoltaic devices, due to the limited fossil fuels and social requirement for economic alternative energy sources. Among the various alternatives such as wind, tidal power, waterpower or solar energy, the use of solar energy have been regarded as the most economic and abundant energy resources to overcome the energy crisis. In order to use solar energy, highly efficient and economic photovoltaic devices should be developed and propagated for popular use, but the Si-based or inorganic based photovoltaic devices are still highly expensive. The alternative technologies (i.e., organic or dye-sensitized solar cells), called as the $3^{rd}$ generation photovoltaic devices, have been researched for replacing Si-based solar cells, but their efficiency and lifetime are still not enough to commercialize in spite of their economic processing.

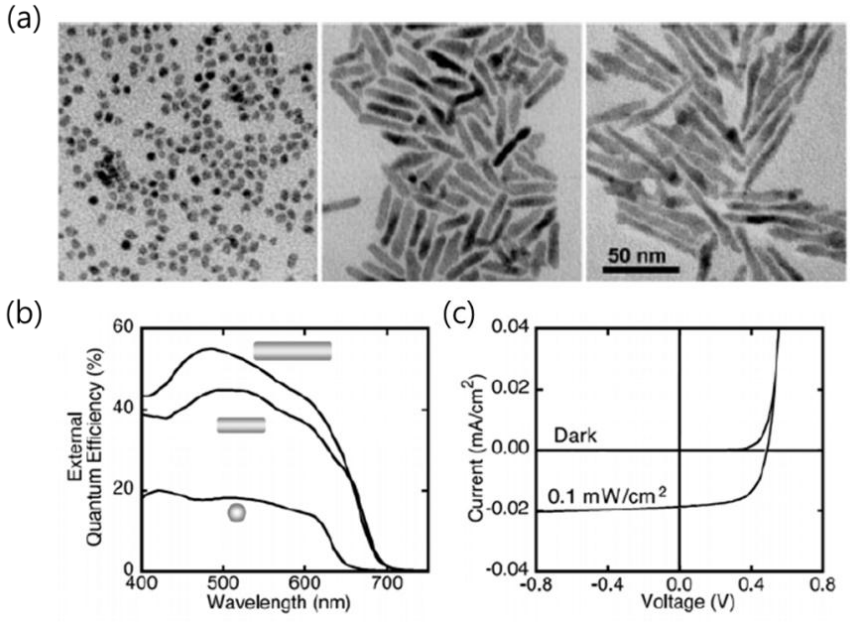


**Figure 1.13** (a) TEM images of shape-controlled CdSe nanocrystals: dots (7 nm x 7 nm), short rods (7 nm x 30 nm) and long rods (7 nm x 60 nm) from the left. (b) External quantum efficiency and (c) the current-voltage characteristics of photovoltaic devices comprising shape-controlled CdSe nanocrystals in (a). [26] © 2002 AAAS.

In order to overcome these shortcomings (namely, low efficiency and stability) and utilize the advantage of inorganic materials (i.e., wide absorption range and photophysical stability), the hybridization of semiconductor nanocrystals with conjugated polymers have been extensively investigated in the past two decades. The semiconductor nanocrystals are pursued as useful materials for light harvesting materials due to their wide absorption range, large absorption coefficient, excellent carrier mobility, solution processibility and stability under persistent illumination of light.

The first hybrid photovoltaic devices was successfully demonstrated by P. Alivisatos et al., who blended shape-controlled CdSe nanocrystals with poly(3-hexylthiophene) (Figure 1.13). From their research, the requirements for successful operation of hybrid photovoltaic cells were suggested; elongated shape for facilitated carrier transport, elimination of insulating surface ligands for exciton dissociation at the interface, and dispersion morphology of semiconductor nanocrystals for effective carrier extraction. Since their pioneering research was published, huge amount of research on cadmium chalcogenide nanocrystals/conducting polymer hybrid photovoltaic devices have been suggested with more advanced nanocrystal morphology, low bandgap conducting polymers and internal morphology control.

More recently, lead chalcogenide (i.e., PbS or PbSe) QD-based all-inorganic photovoltaic cells have been emerged for harvesting IR-range of solar spectrum as well as exploiting multiple exciton generation (MEG) in electricity generation.[36, 71-74] The multiple exciton generation (MEG) is opposite photophysical process to Auger recombination, which generate

multiple excitons from single photon with large energy above bandgap. In a case of lead chalcogenide QD-based photovoltaic devices the carrier mobility can be improved by eliminating surface ligands and passivating surface states with thiolate or halide ligands, and their device performance is reaching 7 %[74] under AM1.5G condition. Although the time and labor-consuming fabrication process (i.e., layer-by-layer deposition) and air-sensitive property of lead chalcogenides fade their advantages, their wide absorption range and huge potential to overcome theoretical efficiency limit have still attracted academia and industrial area to realize highly efficient photovoltaic devices.

### 1.3.3 Water splitting systems

Hydrogen is one of important energy resources replacing fossil fuels as well as huge amount of use in chemical industries. They are environmental-friendly energy without releasing carbon dioxide during combustion, useful chemicals for producing ammonia, and the essential fuel for fuel cells. In order to produce hydrogen avoiding steam reforming process, several method using solar energy have been suggested: electrolysis of water using solar cell, reforming of biomass, and artificial photosynthesis.

For the artificial photosynthesis, various metal oxide semiconductors such as $TiO_2$, $WO_3$, $SrTiO_3$ or $ZnO_2$ have been employed to induce reduction of hydrogen but their bandgap is too large to absorb visible light. In order to increase light absorption and hydrogen production, CdS nanorods or CdSe/CdS nanorods hybridized with metal nanoparticles was proposed by A. P. Alivisatos et al.[35] Although photocorrosion of cadmium ion is a major

constraint of cadmium chalcogenide-based system, the versatile controllability of exciton wavefunctions by tailoring spatial location and composition of additional semiconductors have attracted many researchers to synthesize efficient water-splitting photocatalysts.

# Chapter 2. Synthesis of Shape-Controlled Semiconductor Nanocrystals for Photon-Electron Conversion Materials

## 2.1 InP@ZnSeS, core@composition gradient shell quantum dots for efficient lumophors

### 2.1.1 Introduction

Great attention has been given to colloidal quantum dots (QDs) not only because of their unique and superb optical properties, such as broad absorption, narrow emission spectral bandwidth, and easy bandgap tunability, but also because of their wide application potentials as a new type of phosphors in light-emitting devices[78-83] and biomarkers.[84-87] However, most of previous fundamental studies and potential applications have been focused on II-VI QDs, which could impose critical constraints for practicable applications due to toxic elements (i.e., Cd and Hg) constituting QDs. In order to avoid the potential limitations, QDs with different elements, for example, III-V (i.e., InP[88-97] and InAs[98-101]) or IV (i.e., Si[102-105]) QDs have been investigated. Among the possible material choices, InP QDs, in particular, have gained significant attention due to their wide emission spectrum tunability ranging from visible to near IR region.

Recently, considerable progress in the synthesis of InP QDs has been made, but their optical properties as well as photo/chemical stability are much inferior to relatively well-developed II-VI QDs (i.e., CdSe). Their inferior

properties originate from harsh reaction control due to more covalent bonding character as well as the difficulty in the surface passivation: stronger bond formation as well as the lack of suitable buffer layer between InP core and ZnS shell. The obstacles in the reactivity control as well as problems with the surface passivation have recently been overcome through the delicate control of precursor ratio,[90-92] additives[92] or temperature control,[91] and thus considerable quantum efficiency (QE, up to 70 %) and color purity (FWHM below 45 nm) have been resulted.[91] However, compressive lattice strain and reduced QE due to lattice-mismatched ZnS shell surface passivation need to be resolved. Lattice strain with ZnS shell limits a shell thickness below 1 nm. Such thin shell is quite vulnerable against degradable conditions, leading to reduction in long-term photo- and chemical stability. In order to improve stability of InP-based QDs, the shell thickness should be increased with a lattice adaptor, such as alloyed or intermediate shell, in such a way alleviating the lattice strain with gradual change in shell lattice constant.[106-109] Among available materials, ZnSe is regarded as a proper choice for InP-based QDs thanks to the low toxicity as well as suitable lattice parameter.

In order to integrate ZnSe (alleviating lattice strain) and ZnS (protecting from degradation) and to achieve QDs with high QE and photo/chemical stability, we introduce thick and uniform ZnSeS shells onto InP cores (InP@ZnSeS) in the form of the composition gradient in a radial direction. Utilizing the reactivity difference between TOPSe and TOPS, the ZnSeS shells with the composition gradient were grown on InP cores where Se is dominantly located close to the InP cores while S content increases

along the radial direction of the shell. In the resulting ZnSeS shells, ZnSe alleviated lattice strain and ZnS protected QDs from degradation so that we achieved QDs with high QE and photo/chemical stability. In terms of systematic investigation on the relationship between the shell nanostructure and QD stability, we demonstrated that QDs with thick gradient shells exhibited considerable QE and much enhanced stability against the shell degradation under UV irradiation, ligand exchange, or rigorous purification. This enhanced stability of InP@ZnSeS QDs is attributed to the improved uniformity of composition gradient shells, the efficient confinement of exciton wavefunctions, and the minimized surface oxidation and non-radiative decay via surface states generated by photo-oxidation or ligand exchange.

### 2.1.2 Experimental section

**Materials** For the synthesis of InP@ZnSeS QDs**,** indium acetate ($In(ac)_3$, 99.9 %), zinc acetate ($Zn(ac)_2$, 99.9 %), sulfur (99.9 %, powder), selenium (99.9 %, powder), n-trioctylphosphine (TOP, 90 %), oleic acid (OA, 90 %), 1-octadecene (ODE, 90 %), and 3-mercaptopropionic acid (MPA, 99.8 %) were purchased from Aldrich. Tris(trimethylsilyl)phosphine ($(TMS)_3P$, 10 wt % in hexane) was obtained from Strem Chemicals, Inc. All chemicals were used as purchased.

**Preparation for Stock Solution** For $In(OA)_3$ stock solution, 4 mmol of $In(ac)_3$, 12 mmol of OA, and 36.2 mL of ODE were placed in an 100 mL 3-neck round flask coupled with a condenser. The mixture was heated to 120 °C under vacuum below 200 mTorr for 1 hr. After the mixture was optically clear, the round flask was cooled down to room temperature, followed by backfilling with $N_2$ gas. For $Zn(OA)_2$ stock solution, 20 mmol of $Zn(ac)_2$, 40 mmol of OA, 37.4 mL of ODE were loaded in an 100 mL 3-neck round flask and the same procedure as for the preparation of the $In(OA)_3$ stock solution was followed. $In(OA)_3$ and $Zn(OA)_2$ stock solutions were kept in glove box and gently heated to melt when they were solidified. A TOPSe stock solution was prepared by the dissolution of 4 mmol of Se powder in 4 mL of TOP. A TOPS stock solution was prepaed in the same procedure as TOPSe except for the 4 mmol of S instead of Se.

**Synthesis of InP Cores Passivated with $Zn(OA)_2$** Modified synthetic procedure[91] without 1-dodecanethiol was introduced to prepare InP cores without ZnS shell. 1 mL of $In(OA)_3$ stock solution, 0.25 mL of $Zn(OA)_2$ stock

solution, and 8.75 mL of ODE were loaded into 3-neck round flask and degassed at 120 °C for 1 hr to remove water and oxygen. When the degassing was finished, it was cooled down to room temperature and filled with $N_2$ gas, then 0.1 mmol of $(TMS)_3P$ was injected. Next, the mixture was heated up to 300 °C within 10 min. The color was changed from yellow to orange, and the first exciton peak was found to be around 450 nm.

**Synthesis of InP@ZnSeS Core@Composition Gradient Shell QDs** For a typical synthesis of InP@ZnSeS QDs with n = 2 and r = 0.05, 5 mL of $Zn(OA)_2$ stock solution, 0.1 mL of TOPSe stock solution, and 1.9 mL of TOPS stock solution were sequentially added into InP core-containing solution which was cooled down to 220 °C beforehand, and were heated up to 300 °C with a rate of 10 °C / min for 20 min. Aliquots of QDs were taken time to time during the reaction to investigate the spectral evolution of QDs (the temporal evolution of absorption and emission spectra were shown on the right graph). To purify the product, 2 mL of chloroform, 1 mL of ethanol, and an excess amount of acetone were added into the resulting solution until the solution became turbid, which was precipitated by centrifugation at 10,000 rpm. After the centrifugation the supernatant was decanted and the precipitate was redispersed in organic solvent such as chloroform, toluene, or hexane. The purification process, precipitation and redispersion, was repeated until the QDs were sufficiently purified (about five times).

**Characterization** Room temperature UV-Vis. absorption spectra and photolumninescence spectra were measured with an Agilent 8454 UV-Vis diode array spectrometer and an ACTON spectrometer, respectively. A

photoluminescence quantum efficiency (PL QE) was characterized in the comparison of their fluorescence intensities with those of primary standard dye solution (coumarin 545, quantum yield = 95 % in ethanol) at the same optical density (below 0.05) at the same excitation wavelength (400 nm). The high-resolution TEM images and elemental analysis of the QDs were acquired through JEOL JEM-3011 combined with Link Oxford ISIS 310.

**Photo-stability Test** The photostability of prepared core@shell QDs was tested by measuring the PL QE of QDs obtained after a UV irradiation. The QDs dispersed in hexane were exposed under continuous UV (354 nm) irradiation with 2 $W/cm^2$ in air.

**Chemical Stability Test by Ligand Exchange** The ligand exchange of OA-capped QDs with MPA was performed as follows: 10 mg of QDs dispersed in 5 mL of chloroform was placed in a 20 mL vial, and 0.5 mL of MPA was added to the QD dispersion. Then, the resulting mixture was sonicated for 30 min. After the ligand exchange, MPA-capped QDs were centrifuged at 4000 rpm and purified twice with water (pH 9) and acetone. The resulting MPA-capped QDs were optically clear in water.

### 2.1.3 Results and Discussion

To integrate ZnSe (alleviating lattice strain) and ZnS (protecting from degradation) and achieve QDs with high QE and photo/chemical stability, we introduce thick and uniform ZnSeS shells onto InP cores (InP@ZnSeS) in the form of the composition gradient in a radial direction. Because of the faster reaction rate of TOPSe than TOPS,[106-109] the composition gradient shells, where ZnSe is preferentially formed close to the InP core and the composition of ZnSe in the shell gradually decreases in the radial direction, are easily achieved through a simple addition of Se and S precursors all together (see Figure 2.1.1a), since the reactivity difference in precursors plays a role, and thus reproducibility is remarkable. The composition and thickness in the shell were readily controlled by the amount of shell precursors (In:P:Zn:(Se + S) = 0.1:0.1:*n*:*n* (mmol), where $n$ = 1, 2, and 4) as well as the molar ratio of TOPSe, $r$ (here, $r$ is defined as TOPSe/(TOPSe + TOPS), where $0 \leq r \leq 1$) in the precursor solutions. Temperature control, heating up from 200 to 300 ℃, facilitates the formation of composition gradient ZnSeS shells.

The existence of ZnSe in the ZnSeS shell is easily confirmed from the emission spectra (larger red shift with InP@ZnSeS QDs, compared with InP@ZnS QDs), but the spatial distribution of ZnSe cannot be accurately determined. InP@ZnSeS and InP@ZnS QDs were made from the same pristine InP cores (Figure 2.1.2). To reveal the actual location and composition of Se, energy-dispersive X-ray analysis was conducted, as a function of reaction time (see Figure 2.1.1b and Table 2.1.1). If ZnSe is assumed to be uniformly located in the ZnSeS shell, the atomic ratio of Se in the shell,

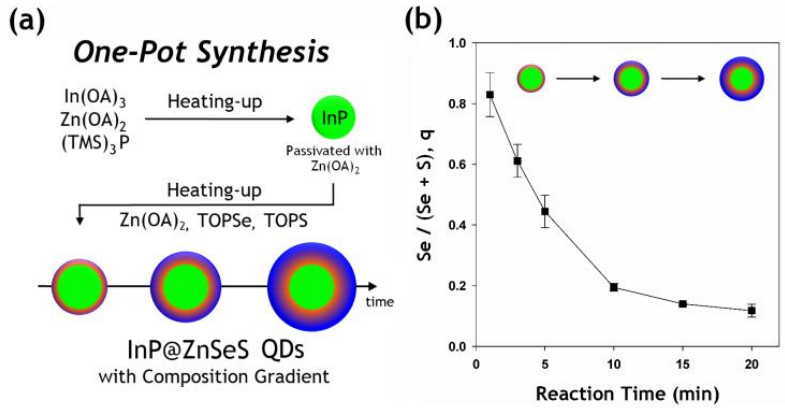


**Figure 2.1.1** (a) A schematic on the synthetic procedure of InP@ZnSeS QDs. (b) Temporal evolution of the atomic ratio of Se (Se / (Se + S)) during the shell growth in InP@ZnSeS QDs with n = 2.

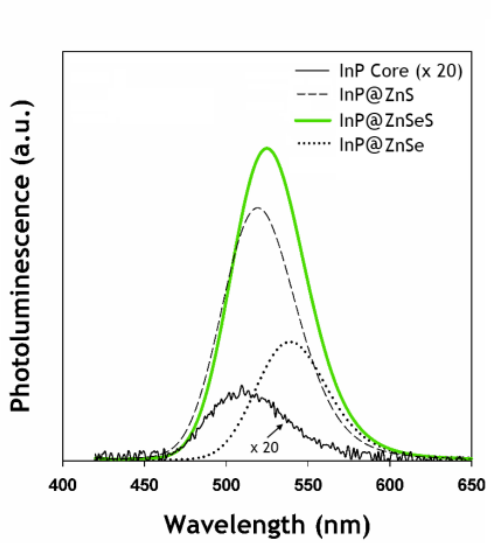


**Figure 2.1.2** Photoluminescence (PL) spectra for InP core only (solid line), InP@ZnS (dashed line), InP@ZnSe (dotted line), and InP@ZnSeS (bold green line, r = 0.05) solutions with n = 2.

**Table 2.1.1** Temporal change in atomic contents for InP@ZnSeS QDs with n = 2 and r = 0.05. (Values in bracket mean standard deviations in estimation)

| Time (min) | Atomic Content (%) | | | | |
|---|---|---|---|---|---|
| | **In** | **P** | **Zn** | **Se** | **S** |
| **1** | 33(3) | 32(2) | 24(3) | 9(1) | 2.0(9) |
| **3** | 26(2) | 24(3) | 27(2) | 14(1) | 9(2) |
| **5** | 22(2) | 18(3) | 25(8) | 16(2) | 19(3) |
| **10** | 10.2(3) | 8.0(6) | 42(1) | 7.7(4) | 32(1) |
| **15** | 7.5(6) | 6.3(3) | 43.1(6) | 6.0(2) | 37.0(3) |
| **20** | 7.0(7) | 6.7(7) | 39(3) | 6(1) | 42(2) |

*q*, which is defined as Se/(Se + S) in the shell, should be constant during the entire reaction time. (cf, *r* is defined as TOPSe/(TOPSe + TOPS) in the precursor solution). However, the gradual decrease in the Se atomic ratio (*q*) was observed, implying that Se is dominantly located near the InP core, whereas S increases in the radial direction of the shell. At the end of reaction, the Se atomic ratio (*q*) in the ZnSeS shell formed with $r = 0.05$ and $n = 2$ precursor solution was found to be 0.12, probably due to the lower reactivity of TOPS, compared with that of TOPSe. Since, in the present study, we did not observe any noticeable blue-shift of the UV–Vis or PL spectra during the reaction at 300 ℃, the alloying of InP cores with shell components (i.e., Zn, Se or S) did not occur in the present reaction conditions, or was unnoticeable even if it occurred.

In conjunction with the relationship between lattice mismatch and shell growth behavior, the QDs formed with a high TOPSe molar ratio (*r*) should exhibit the highest QE at the end of reaction, because of the minimized lattice mismatch (for example, 3.4% for ZnSe and 7.7% for ZnS). However, we found that the optimal molar ratio of TOPSe (*r*) for the highest QEs were located in a narrow range (the dotted circle in Figure 2.1.3a) and that the QEs of InP@ZnSeS QDs at the optimal *r* values were approximately twice as high as those of InP@ZnSe QDs. Moreover, the optimal molar ratio of TOPSe (*r*) remained in a narrow range and hardly changed ($0.05 \leq r \leq 0.2$), even if the amount of shell formation precursors (i.e., *n*) was increased. To clarify these unexpected results, we investigated the temporal evolution of QEs for three

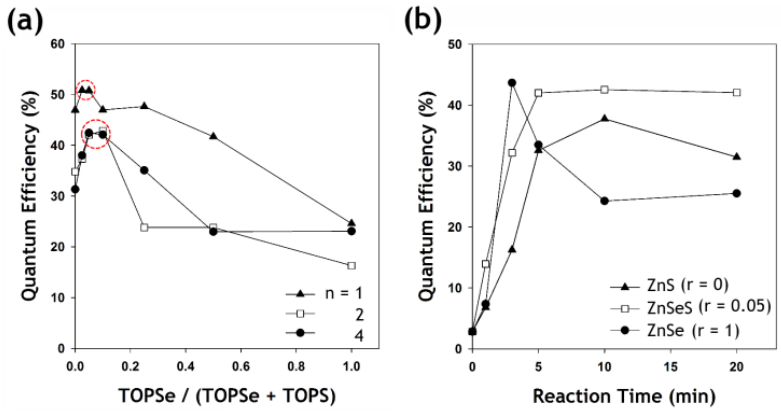


**Figure 2.1.3** (a) PL QEs after the termination of reaction for InP@ZnSeS QDs as a function of the amount of shell precursors (n) as well as the ratio of TOPSe (r) in the shell precursor solution. Dotted red circles represent the optimal points for r for a given n. (b) Temporal evolution in PL QE for InP@ZnS (filled triangles), InP@ZnSe (filled circles), and InP@ZnSeS QDs (open squares) with n = 2.

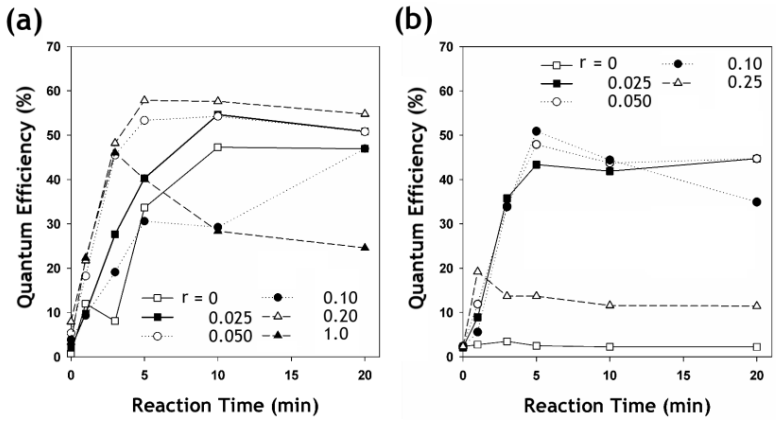


**Figure 2.1.4** Temporal change in PL QE for InP@ZnSeS QDs as a function of the molar ratio of TOPSe (r) with (a) n = 1 and (b) n = 4.

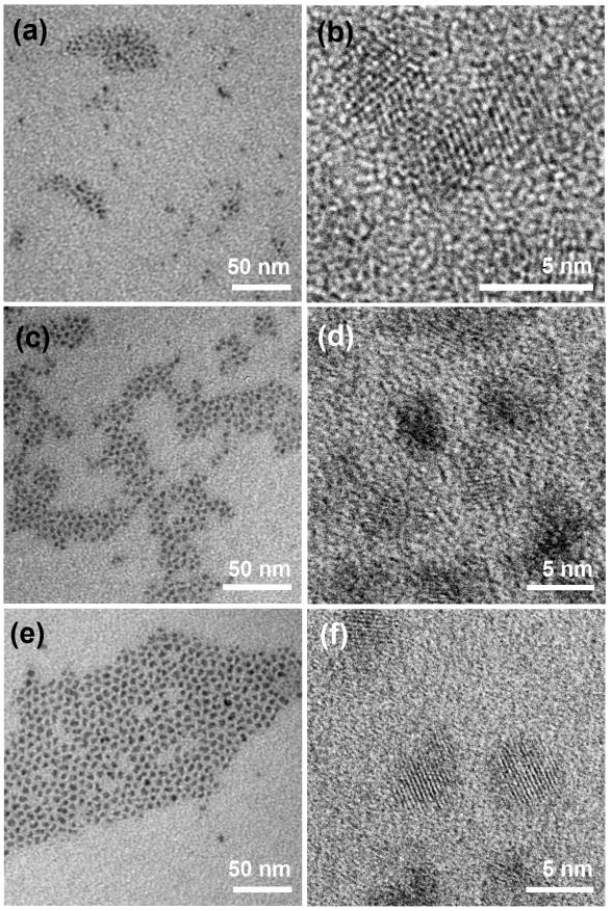


**Figure 2.1.5** TEM images of InP@ZnSeS QDs with (a, b) n = 1, (c, d) n = 2, and (e, f) n = 4 with optimal Se ratio (r).

different shells (i.e., ZnS, ZnSeS, and ZnSe) made from $r$ = 0, 0.05, and 1 with $n$ = 2 fixed, as shown in Figure 2.1.3b. The gradual decrease after the maximum QE is observed in both cases of InP@ZnSe and InP@ZnS QDs, whereas InP@ZnSeS QDs, which are prepared with $r$ = 0.05 and $n$ = 2, do not exhibit any significant reduction in QE after the maximum value. The same tendency was also observed with smaller and larger $n$ values, and the extent of QE reduction of both InP@ZnSe and InP@ZnS QDs becomes more pronounced as $n$ increases (Figure 2.1.4). The gradual decrease in QE after 5–10 min of reaction is usually observed. Based on the high-resolution TEM images in Figure 2.1.5 and the core size estimated from the first exciton peak, ZnSeS alloy shells in the optimal condition turn out to be consist of ~0.6 monolayers of ZnSe shell near the core and ~4.5 monolayers of ZnS outershell (Table 2.1.2). The thickest ZnSeS shell with an optimal molar ratio of TOPSe was estimated to be grown up to 1.9 nm in thickness (see Figure 2.1.5 and Table 2.1.2). This estimated thickness is larger than the previously reported value (i.e., typical QDs with ZnS shells have shell thicknesses of < 1 nm). Even with a rather thick shell, we minimized the lattice mismatch based on the composition gradient shells and, as a result, shells almost twice as thick were overgrown without causing significant reduction in PL QE. The enhanced QE in the narrow range of the molar ratio of TOPSe ($r$) seems to originate from the uniformity of the shells. Ideally, the uniform shell growth can be achieved via thermodynamically controlled growth with materials lattice-matched to the core.[110] Although ZnSe is more relevant than ZnS, in terms of the lattice match, the faster growth of ZnSe shells than ZnS shells

**Table 2.1.2** Estimated shell thicknesses of core@shell QDs with an optimal ratio of TOPSe (r).

| n | r | Core (nm) | Core@Shell (nm) | ZnSeS Shell Thickness in Thickness (nm) | ZnSeS Shell Thickness in Monolayer Unit |
|---|---|---|---|---|---|
| 1 | 0.2 | 1.43 | 3.9 | 1.2 | 4.6 |
| 2 | 0.1 | 1.52 | 4.3 | 1.4 | 5.1 |
| 4 | 0.05 | 1.46 | 5.3 | 1.9 | 7.1 |

seems to be controlled kinetically at a high concentration. Thermodynamically controlled growth is favored for the uniform shell growth. ZnS shell is favored thermodynamically but the uniform shell with it is difficult to achieve, because of a large lattice mismatch. We can guess that only a small fraction of TOPSe is needed to obtain the conformal growth of the ZnSeS composition gradient shells, with ZnSe acting as a lattice adaptor. In addition to the shell uniformity, it is also thought that insufficient conduction band offset between InP core and ZnSe shell (0.2–0.3 eV for green-emitting InP core and ZnSe) is responsible for the decreased QE in cases of large $r$, for the undesired delocalization of electron wave function to QD surface resulting nonradiative decay. This argument is supported by the fact that increasing $r$ leads to a dramatic red-shift of PL spectra (see Figure 2.1.6) and corresponding low QEs.

The luminescent properties of QDs with a thick composition gradient shell are expected to be maintained under degradable conditions, such as surface oxidation by UV irradiation, rigorous purification, or surface modifications frequently done for practical usages. In order to investigate the enhancement in photo/chemical stability of QDs with the composition gradient shells, we treat them with rather harsh UV irradiation in the presence of oxygen, as shown in Figure 2.1.7a and carry the ligand exchange on InP@ZnSeS QDs (with a shell thickness of $t \approx 1.9$ nm), conventional InP@ZnS QDs ($t \approx 0.9$, 1.5 nm), and InP@ZnSe QDs ($t \approx 1.7$ nm) with 3-mercaptopropionic acid (MPA), respectively, shown in Figure 2.7b. We can notice that (i) InP@ZnSeS QDs exhibit the best QE under such illumination and surface modification stresses among other QDs and (ii) their QE

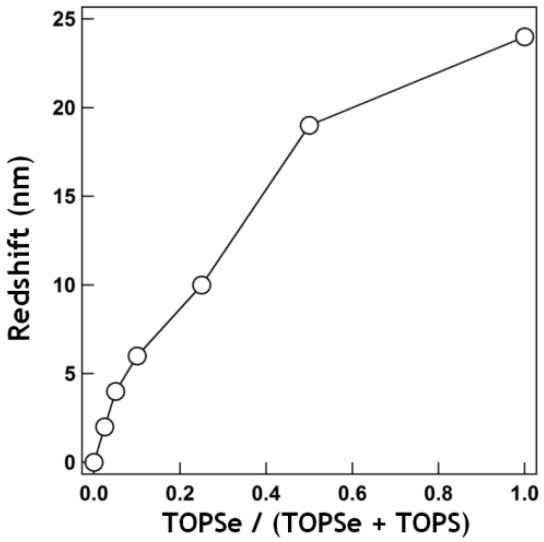


**Figure 2.1.6** The PL redshift of InP@ZnSeS QDs as a function of the molar ratio of TOPSe (r) with n = 4.

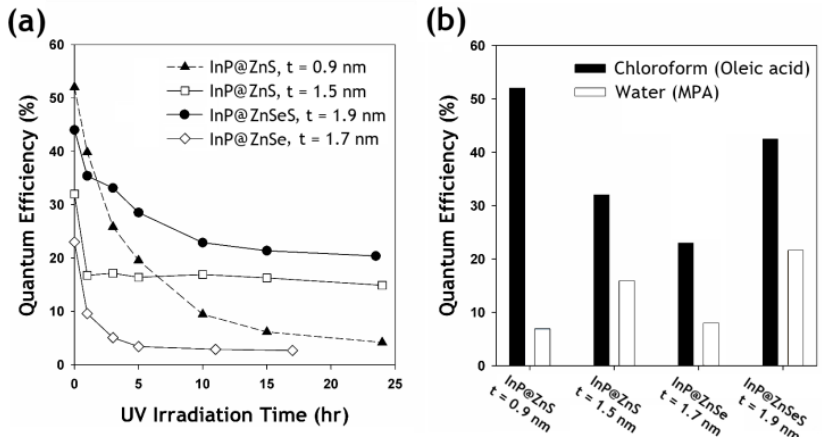


**Figure 2.1.7** The effect of shell composition and thickness on QE against (a) UV irradiation in air (with 2 mW / $cm^2$ at 352 nm) and (b) ligand exchange with MPA.

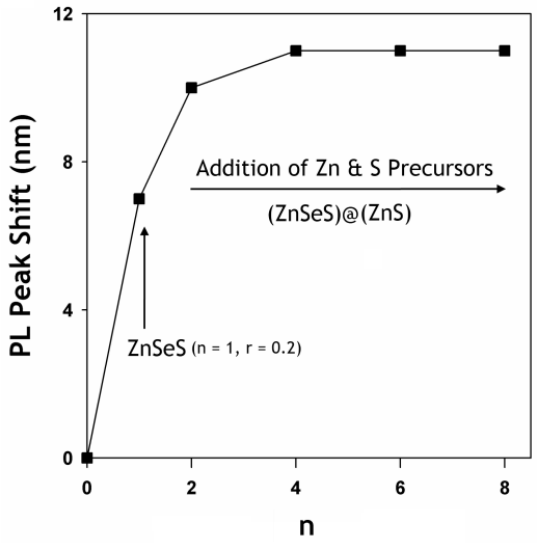


**Figure 2.1.8** The PL redshift of InP@ZnSeS@ZnS QDs as a function of the amount of shell precursors. To investigate the effect of shell thickness on the confinement of exciton wavefunctions, $Zn(OA)_2$ and TOPS precursors were sequentially added into the InP@ZnSeS QD solution (n = 1, r = 0.2) with a standard shell growth procedure.

reduction rate is significantly lower than that of other QDs. We think that the enhanced stability is due to the improved uniformity of composition gradient shells, the efficient confinement of exciton wave functions, and the minimized surface oxidation and nonradiative decay via surface states generated by photo-oxidation or ligand exchange. InP@ZnS QDs with thin shells and InP@ZnSe QDs with small conduction band offset show lower QE and stability, probably because of the thinner shell and the lower potential barrier, respectively. This is again ascertained by repeated shell growth experiments, as shown in Figure 2.1.8. No considerable red shift is observed after the growth of ZnS shells over existing ZnSeS shells with $n = 4$, implying the efficient confinement of exciton wave functions. InP@ZnSeS QDs with the composition gradient shells also retained the same QE against rigorous purification steps (for eight precipitation and redispersion cycles), whereas InP@ZnS QDs with thin shells significantly changed from initially high QE (>50%) to 30% below, even after three purification step cycles.

### 2.1.4 Conclusions

In summary, by utilizing the reactivity difference between TOPSe and TOPS, we synthesized InP@ZnSeS QDs with a composition gradient in a radial direction. In terms of systematic investigation on the relationship between the shell nanostructure and QD stability, we demonstrated that QDs with thick gradient shells exhibited high QE and much-enhanced stability against the shell degradation under UV irradiation, ligand exchange, or rigorous purification. This enhanced stability of InP@ZnSeS QDs is attributed to the improved uniformity of composition gradient shells, the efficient confinement of exciton wave functions, and the minimized surface oxidation and nonradiative decay via surface states generated by photo-oxidation or ligand exchange. Although the current status of InP@ZnSeS QDs is not fully optimized to realize practical optoelectronic devices, the approach taken in the present study (i.e., the composition gradient shell structure naturally made from reactivity difference in precursors) will give clues to facilitate the synthesis of InP QDs with advanced nanostructures. Furthermore, the exploration of novel shell materials, such as Group III–V semiconductors (i.e., GaP or GaN), is underway to eliminate the charge imbalance between Group III–V cores and Group II–VI shells and, thus, improve the emission properties of InP-based QDs.

## 2.2 Scalable and Controllable Synthesis of CdSe Tetrapods with High Morphological Uniformity by Persistent Kinetic Growth and Halide-Mediated Phase Transformation

### 2.2.1 Introduction

Shape- and size-controlled semiconductor nanocrystals have recently drawn keen attention due to their tunable optical and electrical properties. Precise control in their dimension and spatial chemical composition (i.e., dot, rod, or tetrapod structure with homogeneous or multi-compositions) enables us to manipulate their electronic states,[14, 111] exciton relaxation dynamics,[112-114] and transport phenomena,[115-116] governing the photophysical processes of carriers within nanocrystals or nanocrystals arrays.[31, 117] Beyond the fundamental understanding, these shape- and size-engineered nanocrystals have been widely utilized as essential building elements in various optoelectronic applications such as solar cells,[27, 29-31, 115] single-electron transistors,[116] water-splitting systems,[35] or nanoscopic stress gauge.[34]

Among various candidates, cadmium chalcogenides tetrapod nanocrystals[118-120] have been investigated to exploit their unique structure enabling good charge carrier separation at the surface, efficient carrier transport along interconnected branches, and their broad bandgap tunability. Despite all those advantages, the in-depth study of optoelectronic properties and their utilization has been limited because of the difficulty in controlling their size and shape uniformly as well as producing them in large quantity. As a result, the scalable synthesis of tetrapods with high morphological

uniformity and crystallinity is largely required not only for the better understanding of the structure-property relationship in nanoscopic systems but also for their practical use in various optoelectronic applications.

Herein, we present simple, controllable, and scalable synthesis of CdSe tetrapods enabled by the "continuous precursor injection (CPI)" approach using halide ligands. The CPI approach involves the successive injection of precursors into the seed solution at a controlled rate so that the reaction condition remains in the kinetic growth regime for the anisotropic growth (Scheme 2.1.1). This approach is distinguishable from the previous synthesis in terms of nanocrystal growth, which mainly aims for spherical core or core/shell nanocrystals under the thermodynamic growth regime. In the present study, by contrast, we increase the injection rate at much higher level to maintain the large precursor flux, driving the asymmetric growth of nanocrystals under the kinetic growth regime. The kinetic growth is maintained through the continuous injection of precursors with controlled injection rate, thus complicate and subtle control in ligand ratio or reaction quenching is not required for the shape control of tetrapods; longer reaction time yields the tetrapods with longer and thicker arms and the simple variation in reaction temperature and injection rate widen the control window of morphology. This excellent controllability and processibility are far superior to the previous synthetic method.[118-121] Moreover, the halide ligand compounds, the source of halide ligands, were introduced as a substitute for conventional alkylphosphonic acids, in order to initiate the structural development of CdSe tetrapods in economic way.

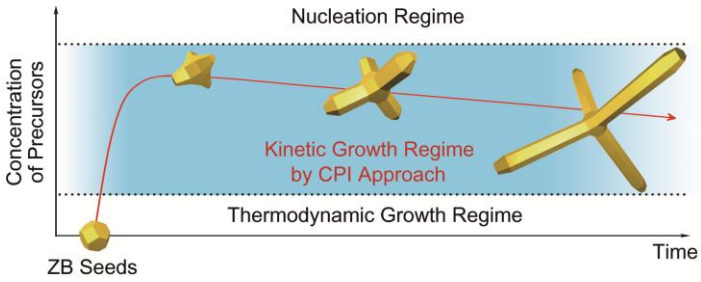


**Scheme 2.1.1** A schematic illustration on the CPI approach.

### 2.2.2 Experimental section

**Materials** For the synthesis of CdSe tetrapods, cadmium oxide (CdO, 99.95 %) was purchased from Alfa Aesar. Selenium (99.99 %, powder), n-trioctylphosphine (TOP, 90 %), oleic acid (OA, 90 %), 1-octadecene (ODE, 90 %), cetyltrimethylammonium bromide (CTAB, 99+ %), sodium bromide (NaBr, 99+ %), ammonium bromide ($NH_4Br$, 99.0 %), tetrabutylammonium bromide (TBAB, 98.0 %), tetrabutylammonium chloride (TBAC, 97.0 %), tetrabutylammoniu iodide (TBAI, 98 %), and methoxyacetone (95 %) were purchased from Sigma Aldrich. All chemicals were used as purchased.

**Preparation of injection solution.** For the preparation of cadmium oleate ($Cd(OA)_2$) solution, 10 mmol of CdO, 7.8 mL of OA, 6.2 mL of ODE, and 1 mL of TOP were placed in an 100 mL 3-neck round flask coupled with a condenser. The mixture was heated to 280 °C under $N_2$ flow for 20 min. After the mixture was optically clear, the round flask was cooled down to 50 $^oC$ and added 0.14 mmol of CTAB under $N_2$ flow. Separately, 12 mmol of Se and 6 mL of TOP were mixed in a 50 mL 2-nect round flask with a condenser and heated at 200 $^oC$ until the mixture became transparent solution. After the TOPSe was cooled down to room temperature, 5 mL of TOPSe solution was added to $Cd(OA)_2$ solution and the mixed solution was stirred them for 5 minutes.

**CdSe seeds with zincblende crystal structure**. Modified synthetic procedure[122] was employed to prepare CdSe seeds with zincblende crystal structure. Firstly, 0.5 mmol/mL of $Cd(OA)_2$ solution was prepared by reacting 5 mmol of CdO, 5 mL of OA, and 5 mL of ODE with the same reaction

condition described above. Next, 1 mmol of Se and 10 mL of ODE were loaded into 100 mL 3-neck round flask and heated up to 300 $^{o}$C under $N_2$ flow. When the Se/ODE solution become optically clear, 4 mL of $Cd(OA)_2$ solution (2 mmol) was rapidly injected into the solution and reacted at 270 $^{o}$C for 15 min. Finally, 6 mL of ODE was added into the seed solution and cooled down to room temperature. In common, the 1$^{st}$ exciton peak was located around 630 nm (Agilent 8454 UV-Vis diode array spectrometer), which yields spherical CdSe seeds with ~ 5 nm of diameter, and the concentration was 60.5 μmol/L estimated from 1$^{st}$ exciton peak – diameter – absorption coefficient correlation.[123] For the crude ZB CdSe seed solution, the absence of purification process doesn't affect the quality of final product if the amount of seeds is same.

**Representative synthetic procedure for CdSe tetrapods in terms of CPI Approach** 5 ml of seed solution, 2.25 mL of OA, 1.5 mL of TOP, 21.25 mL of ODE, and 0.21 mmol of CTAB (or other halide ligand sources in Table S1) were placed in 3-neck round flask with condenser, followed by heating up to 260 $^{o}$C. When the temperature is reached at 260 $^{o}$C, 20 mL of injection solution was added into the seed solution with 0.4 mL/min of injection rate for 50 min. Small amount of aliquots of samples were taken time to time during the reaction to acquire the spectral and shape evolution of tetrapods (Carl Zeiss LIBRA 120 and JEOL JEM-3011). To purify the product, 2 mL of chloroform and an excess amount of acetone were added into the resulting solution until the solution became turbid, which was precipitated by centrifugation at 3,000 rpm. After the centrifugation the supernatant was

decanted and the precipitate was re-dispersed in organic solvent such as chloroform, toluene, or hexane. The precipitation and re-dispersion was repeated until the samples were sufficiently purified.

**Control in Arm Length and Diameter** In order to control in arm length (Figure 2.2.4c), the injection rate was stepwisely changed as follows: From 0.4 (for 5 min), 0.5 (for 4 min), 0.7 (for 5.7 min) to 1 mL $min^{-1}$ (for 2 min) at 260 $^{o}$C. It gave 43, 61, and 83 nm of arm length at 9, 11.8, and 13.8 min of elapsed reaction. Besides, the control in arm diameter (Figure 2.2.4d) was achieved by changing injection rate from 0.5 to 0.2 mL $min^{-1}$ after 12 min of elapsed reaction, which yields 4.7, 5.8, and 9.4 nm of arm diameter at 22, 52, and 122 min of elapsed reaction. For the CdSe tetrapod with stepwisely-varying arm diameter (Figure 2.2.4e), the reaction temperature was varied as follows: from 280 (for 33.3 min) to 210 $^{o}$C (transition time: 20 min, reacted at 210 $^{o}$C for 13.3 min) with 0.3 mL $min^{-1}$ of precursor injection rate.

**Investigation on Ripening Kinetics** Firstly, 0.2 mmol of CdO, 0.33 mL of OA (0.13 mL for the formation of $Cd(OA)_2$ and 0.2 mL as excess), and 9.17 mL of ODE were placed in 3-neck round flask equipped with a condenser, and reacted at 280 $^{o}$C for 20 min. After the flask was cooled down, 0.1 mmol of elemental Se was added and the mixture was heated up to 240 $^{o}$C for 15 min. When the temperature is reached to 240 $^{o}$C, 0.5 mL of TOP and 2 mL of ODE containing certain amount of CTAB and OA were injected into flask (For instance, 0.135 mmol of CTAB and 0.2 mmol of OA were mixed with ODE for p = 0.15. 0.65 mmol (0.2 mL) of OA was already contained when the $Cd(OA)_2$ solution was prepared.). From this time, small aliquots were

extracted time to time during the reaction to measure the 1st exciton peak. The average size was estimated from the 1st exciton peak – diameter correlation report.[123]

**XPS Measurement** XPS spectra were measured with a KRATOS AXIS-His, referenced to the binding energy of Au 4f electrons. Quaternary ammonium halides and CdSe nanocrystals induced by those compounds were placed on the substrate (Au thin film with 30 nm of thickness on Si wafer) and dried overnight under vacuum. Signals were obtained around the peak of interest with the pass energy of 20 eV with 120 meV of interval at ~ 5 x $10^{-10}$ Torr.

**Estimation on the Amount of Oleate Ligands using $^1$H NMR** Firstly, 165 μmol of spherical CdSe QDs (diameter: 5.3 nm) was dispersed in 5 mL of ODE and 0.5 mmol of TOP, then certain amount of OA and CTAB (1 mmol in total, for example, 0.5 mmol of OA and 0.5 mmol of CTAB were added for p = 0.5) were also added. Then, their temperature was elevated up to 200 $^o$C and kept for 30 min. After the reaction was terminated, the crude solution was purified three times and dried under $N_2$ for 5 min. Next, the resulting powder was dispersed in 0.8 mL of $CDCl_3$ containing methoxyacetone (0.11 M, serving as a concentration reference) and measured a $^1$H NMR spectrum. The total amount of oleate ligands in the sample ($M_p$) was calculated from the ratio between the integration area (A) of methine peak (at 5.29 ppm, from two protons) and methoxyacetone peak (at 3.97 ppm, from two protons) as follows:

Total amount of oleate ligands in the sample ($M_p$)

$$= (A_{methine} / A_{methoxyacetone}) \times 0.11 \text{ mmol/mL} \times 0.8 \text{ mL}$$

In order to correct the loss of QDs during purification and sampling steps, 0.05 mL of QD dispersion was extracted from each sample and diluted to 1/1010 with 50.45 mL of $CHCl_3$. From the optical density (OD) at the 1st exciton peak, the correction factors ($c_q$, defined as $OD_{control}$ (p = 0.5, 0.33, 0.25, 0) / $OD_{reference}$ (p = 0)) were obtained, where the 1st exciton peaks were deviated from the original value, below 1 nm. Finally, the actual amount of oleate ligands ($M_c$) was calculated by following calculation.

Corrected amount of oleate ligands in the sample ($M_c$) = $M_p$ / $c_p$

### 2.2.3 Results and discussion

For the representative synthesis of CdSe tetrapods, zincblende (ZB) CdSe seed nanocrystals (diameter of 5.1 nm) were continuously fed with a mixed solution of arm-constituting precursors (i.e., cadmium oleate and TOPSe) and secondary ligands (i.e., cetyltrimethylammonium bromide (CTAB) dissolved in 1-octadecene) at a constant injection rate (e.g., 0.4 mL/min). Surprisingly, as-synthesized CdSe tetrapods exhibit more than 93% of shape selectivity over other shapes (shape selectivity defined as the number of tetrapods divided by the total number of nanocrystals of different shape, see Figures 2.2.1 and 2.2.2) without further post size- or shape-selection procedures. Distinct multiple excitonic features in the ensemble absorption spectra (Figure 2.2.1a) support that as-synthesized CdSe tetrapods possess high uniformity in their arm diameter, in agreement with the TEM analysis (Figure 2.2.1b-g). In addition, the wurtzite (WZ) arms are highly crystalline and directional, as manifested by the stacking sequences along [000 $\bar{1}$ ]-direction in the HRTEM image as well as the sharpened (002) diffraction peak in the powder X-ray diffractogram (Figure 2.2.3). These high quality tetrapods can be easily scaled-up in multi-gram quantity (i.e., 1.8 g shown in the inset of Figure 2.2.1g without the deterioration of morphological uniformity.

In a detailed observation on the evolution of CdSe tetrapods, the arms showed two distinctive stages as below: the burst arm elongation (stage I) followed by its steady growth (stage II) in contrast to the linear growth of arm diameter (Figure 2.2.4). We could explain the different growth behavior of arms in both length and diameter in terms of surface reactivity

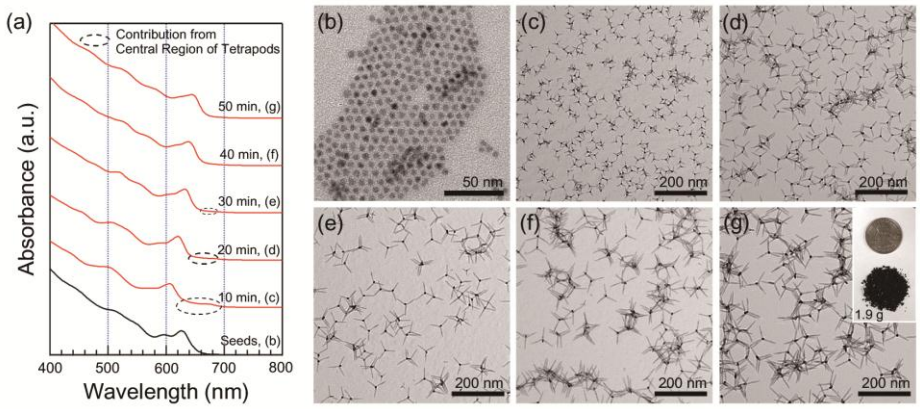


**Figure 2.2.1** (a) Ensemble absorption spectra of CdSe seeds (black) and CdSe tetrapods (red) prepared by the CPI approach. Distinct multiple excitonic features observed in absorption spectra support excellent uniformity of the arm diameter of prepared CdSe tetrapods. TEM images of at (b) 0 (seeds), (c) 10, (d), 20, (e) 30, (f) 40, and (g) 50 min of reaction elapsed. The inset in (g) is the final product obtained from a single batch of reaction. A coin in the picture is a US quarter.

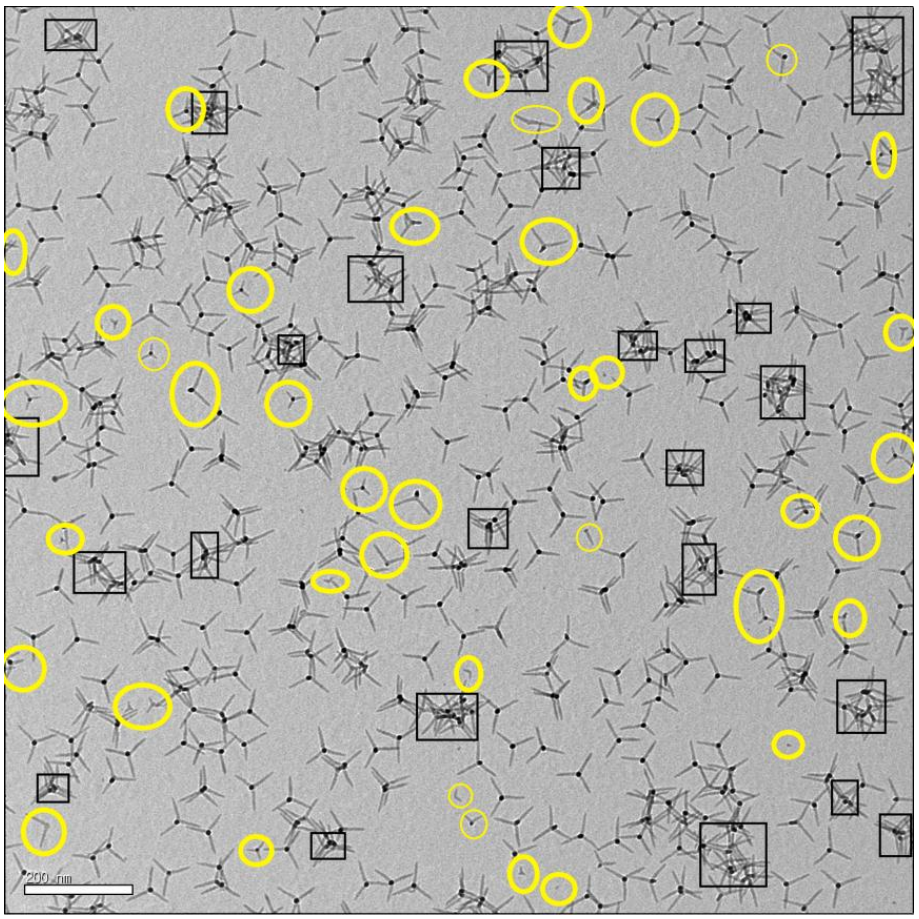


**Figure 2.2.2** A low magnification TEM image of CdSe tetrapods given in Figure 1b. Aggregates (black boxes) are excluded in the counting when we consider the shape selectivity of CdSe tetrapods. Yellow circles represent defective nanocrystals (i.e., dots, mono-, bi-, tripods, and tetrapods with short arms).

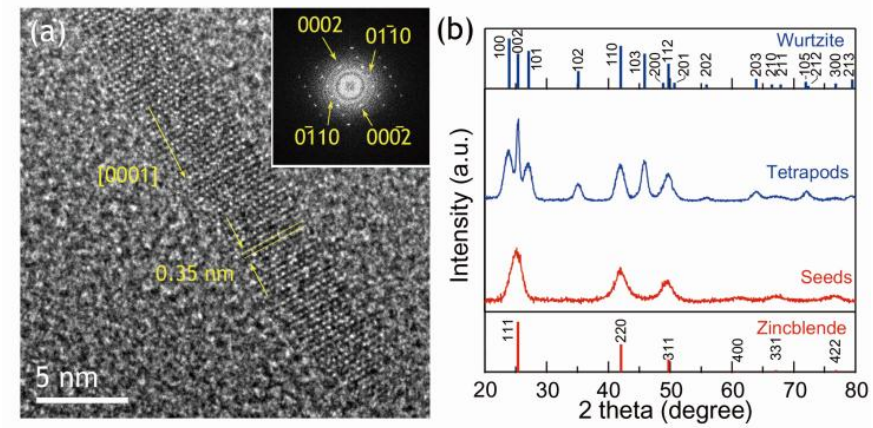


**Figure 2.2.3** (a) A HR-TEM image of an arm region with a FFT pattern (inset). (b) Powder X-ray diffractograms of ZB CdSe seeds (red) and tetrapods with WZ-arms (blue), referenced to JCPDS 08-0459 for wurtzite CdSe as well as 19-0191for zincblende CdSe.

and precursor concentration.[124] In the early reaction stage (Stage I), the precursor flux supplied to the surface is high enough that the most reactive $(000\bar{1})$-facet determines the anisotropic growth of the WZ arm along the $[000\bar{1}]$-direction (*i.e.*, the kinetic-controlled growth). As the reaction proceeds (Stage II), the relative precursor flux supplied to the unit surface area decreases as a result of the increase in entire reaction volume/surface area and, as a result, the diffusion rate of precursors limits the surface reaction on the $(000\bar{1})$ facet (*i.e.*, the diffusion-controlled growth). This spontaneous change in the growth mode along the $[000\bar{1}]$-direction leads to the alteration in the growth rate of arm length. In contrast, the surface reactivity responsible for the radial growth (*i.e.*, $(11\bar{2}0)$- and $(10\bar{1}0)$-facets) is considerably lower by an order of magnitude than that of $(000\bar{1})$-facet, so the growth mode of arm diameter remains as constant in the precursor-concentration variation selected in the present study. This implication is clearly observed in Figure 2.2.4b, where the high injection rate and low reaction temperature result in the tetrapods with high aspect ratio (L/D). However, it is important to note that the undesired nucleation of seeds or the dissolution of WZ arms took place at much higher injection rate (over 1.0 mL/min at 260 $^{o}$C) or at very high reaction temperature (300 $^{o}$C with 0.6 and 0.3 mL/min of injection rate), meaning that these kinds of reaction conditions should be avoided.

Based on these kinds of synthetic strategies, the stepwise variation of injection rate yielded a series of arm length-controlled or diameter-controlled tetrapods (Figures 2.2.4c and 2.2.4d). Moreover, the abrupt change in

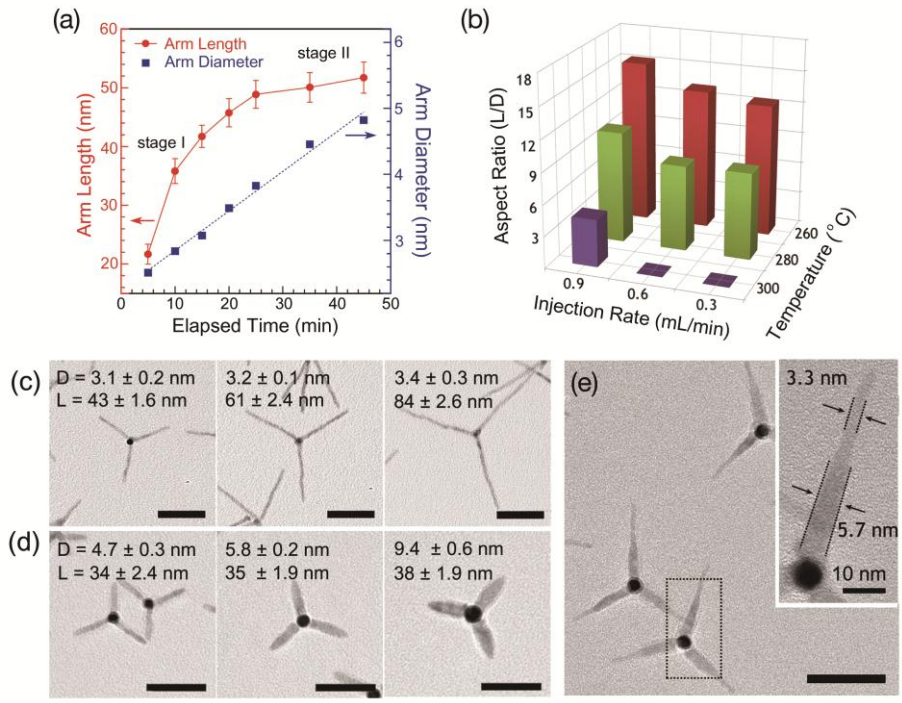


**Figure 2.2.4** (a) Representative growth behavior of CdSe tetrapods (arm length (●) and diameter (■)) as a function of reaction time. Arm diameter was estimated from the excitonic transition absorption peak in correlation with TEM images (Figure 2.2.5). (b) The effect of injection rate and reaction temperature on the aspect ratio of arms (L/D) obtained at 10 min of elapsed reaction. TEM images of (c) arm length-controlled CdSe tetrapods and (d) diameter-controlled CdSe tetrapods. (e) A TEM image of CdSe tetrapods with stepwise-varying arm diameter. The inset is a high magnification image of arm region. All the scale bars are 50 nm.

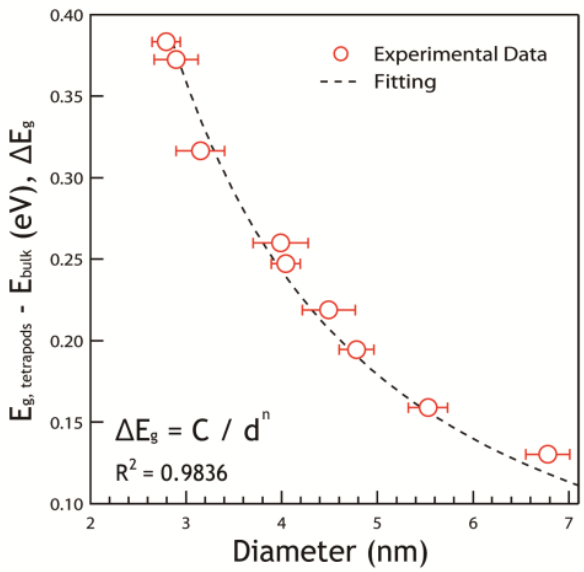


**Figure 2.2.5** A plot of theoretical $\Delta E_g$ ($E_{g,\ tetrapod} - E_{bulk}$) values against arm diameter (d) of CdSe tetrapods. The tetrapods with long arms ranging from 20 nm to 50 nm were chosen to minimize the influence of central cores. Empirical least-squares fitting to the equation, $\Delta E_g = C / d^n$, gave $C = 1.60 \pm 0.02$ eV $nm^{1.36}$ with a fixed n of 1.36.

diameter within one arm is also possible by controlling the reaction temperature stepwise fashion (Figure 2.2.4e). Although both injection rate and reaction temperature could be the major parameters to control arm length and diameter of tetrapods, we found that the reaction temperature is more dominant for the growth of arm diameter.

The exceptional shape selectivity in the present study is a unique distinguishiable feature and cannot be solely interpreted by the CPI approach. In the previous research, it was found that the phase stability of ZB seeds determines the successful synthesis of tetrapod nanocrystals. The transformation of ZB seeds to WZ crystals often causes the formation of rod-shaped nanocrystals, resulting in the reduction of shape selectivity.[125] For the case of CTAB for tetrapods, S. Asokan *et al*. proposed that the charge interaction between CTAB and nanocrystal surface suppresses the formation of WZ seeds and induces the shape development of CdSe tetrapods.[126] However, the detailed reaction mechanism and the transformation of crystal structure by halides have remained to be resolved.

In order to solve the origin of the exceptional shape selectivity of CdSe tetrapods, we investigated the effect of halide ligands on the CdSe nanocrystals. We selected two groups of halide ligand compounds as follows: group I) bromide compounds with different ammonium cations (i.e., $NH_4Br$, tetrabutylammonium bromide (TBAB), and CTAB); group II) different halide compounds with the same tetrabutylammonium cation (i.e., tetrabutylammonium chloride (TBAC) /bromide (TBAB) /iodide (TBAI)). Interestingly, under the same reaction conditions, all of the bromide

compounds (group I) resulted in the branched nanocrystals regardless of cations. Moreover, chloride and iodide also produced the same morphology as the bromide case, when tested with halide ligand group II. All the results are summarized in Figure 2.2.6 and Table 2.2.1. These results indicate that the shape evolution of CdSe tetrapods is not directly related to the bulkiness of cations but, instead, highly correlated with halides. The decisive evidence comes from X-ray photoelectron spectroscopy (XPS) results which confirm the presence of halides on the surface of CdSe tetrapods (Figure 2.2.7). Comparative XPS analysis clearly shows that the binding energy of Br 3d electrons is shifted from 66.9 eV (black, TBAB) to 69.2 eV (red, Br-bound CdSe tetrapods processed with TBAB) similar to the value of bulk $CdBr_2$, revealing that bromides are bound to the surface Cd atoms of CdSe tetrapods.[127] The binding energies of Cl 2p electrons and I $3d_{5/2}$ electrons in the CdSe tetrapods formed with halide ligand compounds TBAC and TBAI, also coincide with those of bulk $CdCl_2$ and $CdI_2$, respectively.[128] Quantitative $^1H$ NMR study on the amount of oleate ligands bound to the CdSe nanocrystals reveals that the amount of oleate ligands decrease with the increase in the halide content (Figure 2.2.8a and Table 2.2.2), supporting that the halides introduced are selectively bound to the surface Cd atoms by replacing the oleate ligands and thus induce the anisotropic growth. This oleate-halide exchange can be interpreted by the hard and soft acid and base theory. In this framework, $Cd^{2+}$ is a soft acid and the oleate (i.e., carboxylate) is a hard base. The soft acids react more effectively with soft bases, thus iodide (soft base), bromide, and chloride (borderline base) can be more

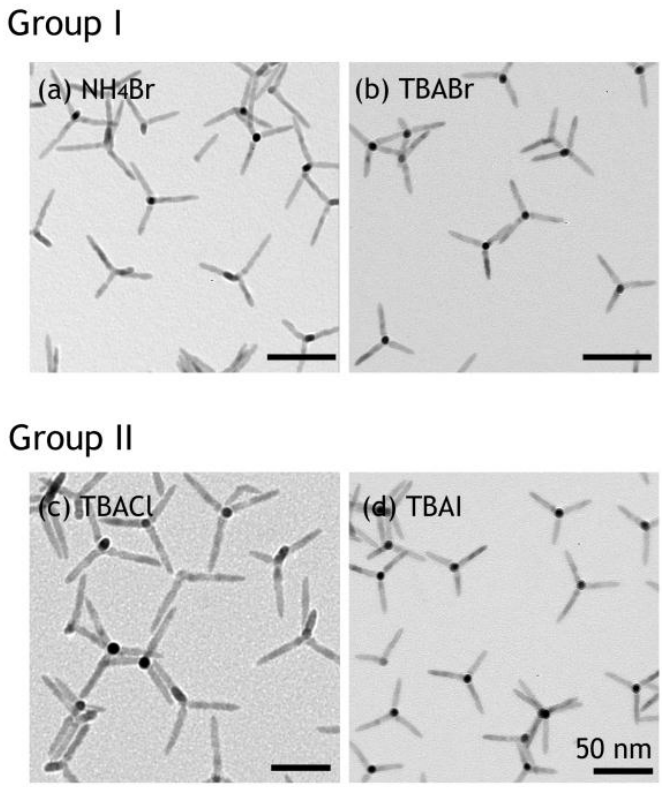


**Figure 2.2.6** TEM images of CdSe nanocrystals obtained with: (a) ammonium bromide ($NH_4Br$), (b) tetrabutylammonium bromide (TBAB), (c) tetrabutylammonium chloride (TBAC), and (d) tetrabutylammonium iodide (TBAI). All the samples were prepared the same reaction condition (see Experimental Section) except for the halogen ion sources.

**Table 2.2.1** The effect of various types of branching agents on the shape of CdSe nanocrystals: group I) bromine compounds with different counterparts (i.e., $NH_4Br$, tetrabutylammonium bromide (TBAB), and CTAB); group II) halide compounds with the same cation part (i.e., tetrabutylammonium chloride (TBAC), TBAB, and tetrabutylammonium iodide (TBAI)) (T: tetrapods).

| Group I | | Group II | |
|---|---|---|---|
| Additives | Major Shape (Multipods/Total) | Additives | Major Shape (Multipods / Total) |
| $NH_4Br$ | T (~ 99 %) | TBAC | T (~ 99 %) |
| CTAB | T (~ 99 %) | TBAI | T (~ 99 %) |
| TBAB | T (~ 99 %) | | |

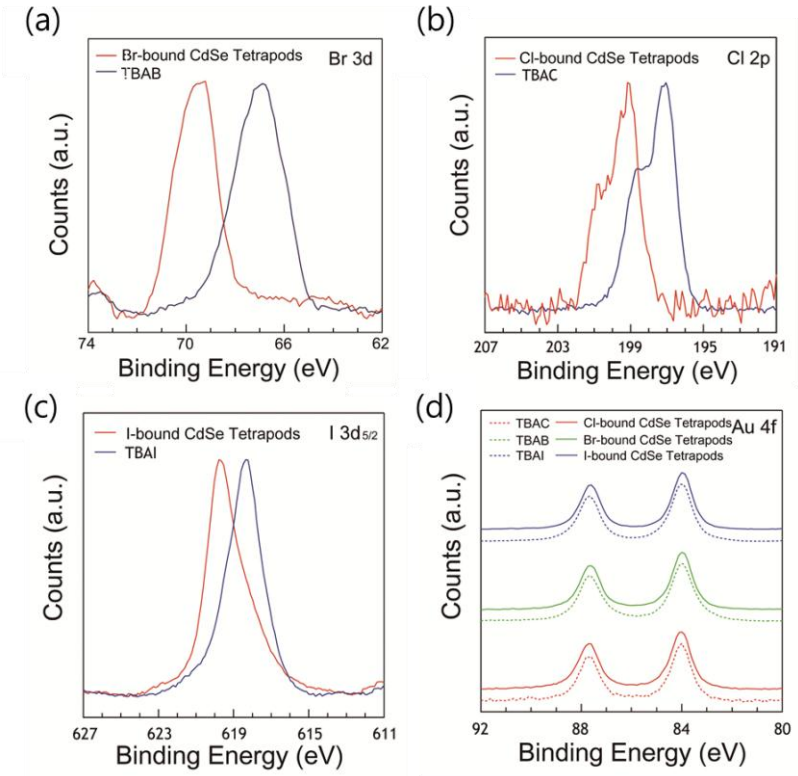


**Figure 2.2.7** (a) Binding energies of 3d electron from Br, (b) 2p electrons from Cl and (c) $3d_{5/2}$ electrons from I, bound to CdSe tetrapods (red) and from TBAB, TBAC and TBAI (blue) measured by XPS. (d) Au 4*f* binding energies of the substrates used as an internal reference: TBAC (red, dashed line), Cl-bound CdSe tetrapods (red, solid line), TBAB (green, dashed line), Br-bound CdSe tetrapods (green, solid line), TBAI (blue, dashed line), and I-bound CdSe tetrapods (blue, solid line).

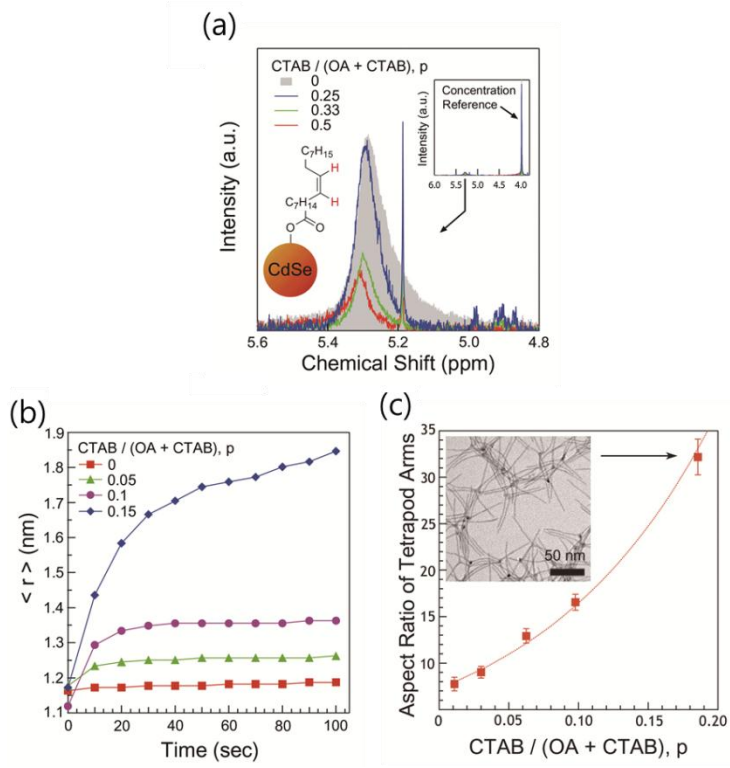


**Figure 2.2.8** (a) The $^{1}$H NMR peaks from the alkene protons of oleate ligands bound to spherical CdSe nanocrystals (denoted in the molecular structure), as a function of p, defined as CTAB / (OA + CTAB). A sharp peak at 5.19 ppm is due to impurities contained in methoxyacetone (served as a concentration reference, inset), contributing less than 1 % of the total integration area. (b) Temporal change in the average radius of CdSe dots (<r>) as a function of p at 240 $^{o}$C. (c) The effect of p on the aspect ratio of CdSe tetrapod arms (L/D) taken at 10 min of elapsed reaction. The inset in d) is the TEM image obtained at the highest p, denoted as an arrow.

**Table 2.2.2** Amount of oleate ligands on spherical CdSe nanocrystals depicted in Figure 2.2.8a.

| **CTAB / (OA + CTAB), p** | **Relative Integration Area at 5.29 ppm (a.u.)** | **$M_c$ (x $10^{-2}$ mmol)** |
|---|---|---|
| 0 | 1 | 3.5 |
| 0.25 | 0.94 | 3.3 |
| 0.33 | 0.38 | 1.3 |
| 0.5 | 0.28 | 0.97 |

effectively bound to Cd site on the nanocrystals. In spite of the stronger bonding strength between Cd and halides than oleate, the negligible difference in the final morphology of tetrapods implies that the formation of Cd-halides bond does not act as a major factor for the structural development and growth kinetics of tetrapods, but connected to the unknown reaction pathway instigated from the surface.

In order to investigate the effect of Cd-halide bond on the change in surface chemistry in more detail, we designed a ripening experiment in a presence of halides and oleic acid (Figure 2.2.8b). Interestingly, the average size of CdSe dots significantly increased with an increasing mole fraction of CTAB (p, defined as CTAB / (OA + CTAB), where OA is remnant oleic acid). This observation is attributed to the dissolution of cadmium halides from the surface and the following ripening process, reported by Saruyama *et al*.[129] The dissolution of cadmium halides from the surface of CdSe nanocrystals generates ligand-free sites with high surface energy, facilitating Ostwald ripening process. Intriguingly, the exposure of ligand-free sites affects the difference in the surface reactivity of WZ facets (i.e., $(000\bar{1})$ and the others). Figure 4d shows the aspect ratio (L/D) of tetrapod arms as a function of the mole fraction of bromide compounds. For a given amount of CTAB (6.9 mmol/L), the remarkable rise in the aspect ratio over 30 with the increasing p (i.e., the increase in the surface coverage of bromide) was resulted (inset in Figure 2.2.8c). With the decreasing p, the aspect ratio of tetrapod arms was drastically reduced, and, eventually, tetrapods or branched morphologies were not observed below 0.01 of p.

The proposed ligand exchange and elimination pathway is summarized as follows: 1) alkylphosphonium halides ($R_4P^+$(halide)$^-$ where R = alkyl chain), formed from reaction between alkylhalides (thermal decomposition product[130]) and neat n-trioctylphospine (TOP), or quaternary ammonium halides transfer halide ligands[73] to surface Cd sites via the ligand exchange reaction, and 2) halide-bound Cds are dissolved by forming $(R_3P)_2Cd(halide)_2$ or $(R_4P)_2Cd(halide)_4$. This proposed reaction pathway is supported by the facts that the shape evolution to tetrapods only occurs in the presence of TOP and that quaternary alkyl ammonium bromides can be replaced with 1-bromodecane (probable thermal decomposition products formed from quaternary alkyl ammonium bromide).

By all accounts, increase in the surface energy by ligand elimination causes the formation and growth kinetics of WZ arms. The clue to the reaction mechanism of present system can be found from the relationship between surface ligands and the crystal structures of nanocrystals. In a case of bulk CdSe, the crystal structure is transformed from ZB to WZ around 100 $^oC$[131] and this is facilitated by decreasing the grain size due to the contribution of surface energy.[132] However, CdSe nanocrystals synthesized with oleic acid are commonly existed as ZB crystal structure because of the stabilization effect of oleate ligands. Thus, if the surface coverage oleate ligands are decreased, then the original ZB nanocrystals or newly-growing phase is likely to be derived to WZ, particularly under high temperature over 100 $^oC$. As well, once after the WZ phase was induced, the inherent difference in surface energy between $(000\bar{1})$ and other facets[133] brings on the anisotropic growth

under kinetic growth regime. Such difference in surface reactivity is amplified with the decreasing amount of oleate ligands, because the oleate ligands stabilize the surface of nanocrystals. A growth trend in Figure 2.2.8c supports this argument.

In this context, the high shape selectivity of the present system looks discrepant. Certainly, the large amount of halide ligands brought about the transformation of ZB seeds to WZ and deteriorated the shape selectivity. However, this undesired process was prevented by the delicate optimization of the amount of halide ligands. In the representative synthesis, the concentration of halide ligands is varied below 10 mM (~ 50 times less than oleic acid). Such small amount of halide ligands is not enough to initiate the transformation of ZB seeds, but affect the embryonic CdSe phase on [41]-facets of ZB seeds. In the initial stage, the newly-generated CdSe phase necessarily has very small domain size (see sharp end of WZ arms in Figure 2.2.9) and is easily transformed to the WZ crystal structure on {111}-facets owing to the increased surface energy contributed by halide exchange and dissolution and favorable hexagonal WZ-stacking on {111}-facets (Figure 2.2.9). As a result, WZ phase can be successfully formed on the ZB seeds and the CPI approach assists the perfect formation and growth of four arms on one ZB seeds with small arm-length deviation by slow arm growth condition.

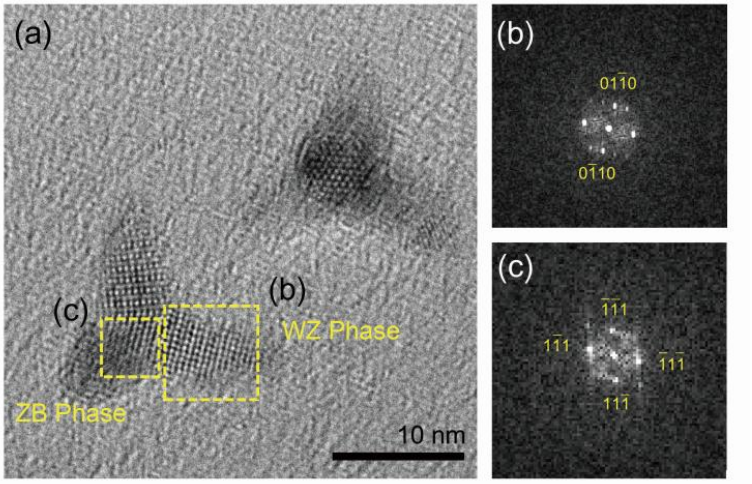


**Figure 2.2.9** A HR-TEM image of CdSe tetrapods at 100 sec of elapsed reaction and their fast Fourier transform (FFT) patterns at (b) ZB seed and (c) WZ arm region (denoted as dotted boxes). The ZB phase is viewed along a [001]-zone axis and the WZ phase is observed with a $[11\bar{2}0]$-zone axis.

### 2.2.4 Conclusion

In summary, we present a controllable, scalable, and simple method to produce CdSe tetrapods with excellent morphological uniformity, and also figure out the origin of morphology development by halide ligands. The halide ligands eliminate surface oleate ligands and destabilize CdSe nanocrystals, resulting in the formation of WZ-phase. By optimizing the amount of halide ligands, ZB CdSe seeds were successfully stabilized and only newly-generating CdSe phase was grown in a form of WZ-arms. Based on this stable ZB seeds and controllable kinetic growth behavior by CPI approach, the CdSe tetrapods with controlled the arm length and diameter could be produced in large scale. Our findings here will make significant contributions toward the economic, large quantity preparation of well-defined 3-dimentional semiconductor nanocrystals and prompt to realize advanced optoelectronic nanodevices.

# Chapter 3. Fabrication of InP Quantum Dot-Based Light Emitting Diodes

## 3.1 Introduction

Quantum dot-light emitting diodes (QLEDs) based on electroluminescence (EL) mechanism have attracted great attention to household lightings as well as full-color display applications. Including talented device properties in terms of light weight, thin, low operation voltage, and high response, exceptional color purity and spectral purity of QDs opens a new opportunity for next generation display technology with vivid and natural colors or lightings with various form factors. Since the basic guidelines on QLEDs are established,[134-135] multilateral efforts on the preparation of efficient and monodisperse QDs, [46, 52-53, 55, 136-137] carrier transporting materials, [18, 138-141] novel device architecture, [140, 142] and fabrication processes[143-145] have been continued to realize the QLEDs to the practical applications. On the basis of accumulated knowledge, recently, QD-vision and Samsung electronics recently developed the full-color all-QD displays by integrating high quality Cd-based QDs on metal oxide thin-film transistor arrays via transfer printing.[146],[143] In terms of device performance, the external quantum efficiency (EQE) of QLEDs is rapidly improving, and even, their maximum luminance is currently comparable to the fluorescence-based organic light emitting diodes.

In spite of the drastic improvement in device performance and positive outlook, however, the commercialization of QLEDs would be inevitably limited by the social restriction for environmental and human safety. Most research on QLEDs has utilized Cd-based QDs due to their high quantum efficiency and well-established synthetic process. Unfortunately, Cd is highly detrimental to environment and the accumulation of that causes irreversible damages to human organs (i.e., liver and kidney), bone, muscles, and finally, fatal disease. To prepare against the probable risk of Cd-based QDs to humans and environment, Cd-free nanocrystal phosphors such as chalcopyrites (i.e., $CuInSe_2$ or $CuInS_2$),[147-149] doped nanocrystals,[150-153] or InP QDs[55, 137, 154-156] have been suggested for light emitting diodes so far. In the visible and near infrared region, those nanocrystals have exhibited controllable emission spectra as well as high fluorescence quantum efficiency reaching ~ 70%, comparable to the Cd-based QDs. However, spectral bandwidth of chalcopyrites and doped nanocrystals is far inferior (~ 100 nm) to the II-VI or III-V QDs (30 ~ 60 nm) so that their utilization has been restricted to the white LEDs[157] or biomarkers,[147] demanding wide emission bands or near infrared emission. Consequently, InP QDs have been regarded as peerless alternatives to environmentally-benign and efficient phosphors with high color purity for realizing full-color QD display.

Requirements on environmentally-benign and efficient LEDs with high color purity have initiated the research on InP QD-based LEDs (InP QLEDs). However, InP QLEDs have shown poor device performance than Cd-based one, in spite of comparable photoluminescence quantum efficiency

(PL QE) between two kinds of QDs. For instance, broadened emission spectrum,[154] considerable parasitic peaks,[155] low EQE (up to 0.26 %), and poor maximum brightness (~ 700 cd/m$^2$)[158] were recorded based on the similar device structures with Cd-based ones, sandwiched QD layer between carrier transport layer. It is evident that the intrinsic difference between CdSe and InP results in those gap, such as electronic property or bandgap position. But curiously, considerations on the difference in material properties and corresponding reconstruction of device structure or QD formulation have not been conducted yet.

Herein, we demonstrate the green light emitting diodes based on InP QDs exhibiting highly improved device performance. Based on the inverted device structure, we designed the optimized core@shell structure of InP QDs as well as electron transporting layer (ETL). Thin [(9,9-bis(3′-(N,N-dimethylamino)propyl)-2,7-fluorene)-alt-2,7-(9,9-ioctylfluorene)] (PFN) layer was introduced on the ZnO layer to faciltate electron injection into QD and achieve balanced recombination. The optimized InP-based QD-LEDs showed 3.46 % of external quantum efficiency (EQE) and maximum brightness of 3,900 cd/m$^2$, comparable performance those from Cd-based QD-LEDs.

## 3.2 Experimental section

**Chemicals** zinc acetate ($Zn(ac)_2$, 99.9%), sulfur (99.9%, powder), selenium (99.9%, powder), n-tributylphosphine (TBP, 97%), n-trioctylphosphine (TOP, 90%)oleic acid (OA, 90%), 1-octadecene (ODE, 90%), and 1-dodecanethiol (DDT, 99.8%) were purchased from Aldrich. Indium chloride ($InCl_3$, 99.99%) and Tris(trimethylsilyl)phosphine ($(TMS)_3P$, 10 wt% in hexane) was obtained from Strem Chemicals, Inc. For the fabrication of LEDs, 4,4',4"-Tri(9-carbazoyl)triphenylamine (TCTA) and [(9,9-bis(3′-(N,N-dimethylamino)propyl)-2,7-fluorene)-alt-2,7-(9,9-ioctylfluorene)] (PFN) were purchased from Lumtec Inc. and 1-science Inc., respectively. All chemicals were used as purchased.

**Synthesis of InP quantum dots with multiple ZnSeS composition gradient shells** Prior to the synthesis of InP QDs, zinc oleate ($Zn(OA)_2$) and TOPSe were prepared as shell-forming precursors. For the $Zn(OA)_2$, 30 mmol of zinc acetate and 19 mL of OA were placed in 100 mL 3-neck flask with a condenser and heated to 120 ℃. The mixture was degassed under 100 mTorr for 20 min, filled with $N_2$ gas, then added with 41 mL of 1-ODE. The final solution was cooled down and kept at 100 $^{o}$C. The TOPSe solution was prepared by dissolving 1 mmol of elemental selenium in 0.5 mL of TOP and 0.5 mL of ODE, under $N_2$ atmosphere.

InP QDs with multiple ZnSeS shells were prepared by multiple overcoating process. 0.1 mmol of $InCl_3$ in 1 mL of tetrahydrofuran, 2 mL of $Zn(OA)_2$ and 8 mL of 1-ODE were loaded in 100 mL flask with a condenser and degassed for 30 min to remove water and oxygen species. Then, the

temperature was rapidly elevated to 300 $^{o}$C and a mixture of 0.1 mmol of $P(TMS)_3$ and 0.4 mmol of STBP (0.4 mmol of sulfur dissolved in 0.5 mL of TBP and 0.5 mL of 1-ODE) was rapidly injected into the reactor. After 20 sec, 0.1 mL of SeTOP was dropwisely added for 20 sec and reacted at 280 $^{o}$C for 10 min. Next, 4 mL of $Zn(OA)_2$, 0.43 mL of 1-dodecanethiol and 0.1 mL of SeTOP were sequentially added and the temperature of mixture was set to 300 $^{o}$C after 10 min of reaction progressed. After 90 min of reaction elapsed, 6 mL of $Zn(OA)_2$ and 0.72 mL of 1-dodecanethiol were added and the mixture was reacted for 120 min. Finally, the mixture was cooled down to room temperature to terminate reaction. For the purification of QDs, precipitation/redispersion method was employed; the crude solution was precipitated with excess amount of acetone and redispersed with toluene. After repeated purification process (typically 4 times), the precipitated QDs were dried under $N_2$ flow for 5 min and dispersed in hexane (around 50 mg/mL). Before use they were kept in a glove box.

**Synthesis of ZnO nanoparticles** ZnO nanoparticles were synthesized by modifying the method reported by Pacholski *et al.*[159] Firstly, 3 g of $Zn(ac)_2 \cdot 2H_2O$ and 120 mL of methanol were placed in 3-neck round bottom flask and heated to 60 $^{o}$C. At that temperature, 60 mL KOH solution containing 1.51 g of KOH was added dropwise into the $Zn(ac)_2 \cdot 2H_2O$ solution with strong agitation. The reaction mixture was kept at 60 $^{o}$C for 2 hr 15 min. At the end of reaction, the product appeared as a milky solution. After precipitating the product by centrifugation at 4,000 rpm, the product was

washed with methanol twice. Finally, the product was centrifuged again and redispersed in 5 mL of butanol.

**Device Fabrication and Characterization** QD-LEDs were fabricated on patterned ITO glass substrates that were cleaned with isopropanol, acetone, and methanol in an ultrasonic bath. Firstly, 20 mg/mL of the ZnO solution was spun on a patterned ITO substrate at 2000 rpm for 60 sec and baked at 90 $^{o}$C for 30 min in $N_2$ atmosphere. The resulting film thickness was 45 nm. Subsequently, 0.5 mg/mL of PFN solution in methanol/acetic acid solution (methanol : acetic acid = 2 μL : 1 mL) was spun to a ZnO layer and dried for 30 min under vacuum. Then, the QD layer was deposited by spin-casting at 4000 rpm for 30 sec. Finally, TCTA (50 nm), $MoO_3$ (10 nm), and Al (100 nm) were sequentially evaporated with a deposition rate of 0.5–1 Å sec$^{-1}$, 0.2 Å sec$^{-1}$, and 3–5 Å sec$^{-1}$, respectively. The current–voltage–luminance characteristics were measured using a Keithley 236 source-measure unit and a Keithley 2000 multimeter coupled with a calibrated Si photodiode. Electroluminescence spectra of the QLEDs were obtained using a Konica-Minolta CS-1000A spectroradiometer.

## 3.3 Results and discussion

Green-emitting InP QDs with multiple ZnSeS composition gradient shells were prepared by modified synthetic procedure by J. Lim et al.[155] The composition gradient is such that Se is dominantly located close to the InP cores while S content increases along the radical direction of the shell. The presence of Se mitigates compressive lattice strain between InP core and ZnS shell phases and facilitates uniform growth of ZnS shells, leading to the enhancement in PL QE as well as stability against various stresses deteriorating QDs (i.e., heat, UV-irradiation, ligand exchange, or purification). On InP cores with ~ 1.1 nm of diameter, we overcoated double ZnSeS composition gradient shells using TOPSe, 1-dodecanethiol, and zinc oleate at 300 $^{o}$C (hereafter referred to as InP@$GS_2$, where 2 is a number of composition gradient shells). At high temperature, low precursor reactivity and low concentration level of precursors assists non-preferential growth of shells on the nanocrystals' facets and following uniform growth. Due to the enhanced uniformity and minimized lattice strain by Se, as-synthesized InP@$GS_2$ yielded (Figure 3.1b) over 70% of PL QE with bright green emission (FWHM ~ 50 nm, $\lambda_{max}$: 500 nm ~ 520 nm), ), even though shell thickness increased up to 1.7 nm (over 6 monolayers). This is one of successful achievement among previous InP QDs, which has reported 40 ~ 70% of PL QE for thin shells below 1 nm.[55, 154] The bandgap position of InP@$GS_2$ was estimated by ultraviolet photoelectron spectroscopy (UPS) and absorption spectra: ~ 5.9 eV for valence band and ~ 3.5 eV for conduction band, respectively. The effective bandgap position of InP@$GS_2$ was higher than Cd-based QDs,

reflected from i) closer bandgap position of InP to vacuum level compared with CdSe,[160] ii) increase in conduction band of InP core by quantum confinement effect,[161] and iii) ZnSeS shell phases.[162]

Using the improved green InP@$GS_2$ QDs above, the inverted device structure with transparent ITO electrodes as a bottom cathode and Al as a top anode was adopted for InP QLEDs (Figure 3.2a). This inverted device structure has recently been utilized in current-driven organic LEDs as well as QLEDs, because of the better device stability,[163] the easy integration of unit devices with thin film transistor (TFT) backplanes, and the facile selection of hole transporting materials by thermal evaporation.[140] However, previous inverted structure using ZnO ETL has a limitation for an electron injection into the InP@$GS_n$ QDs. As shown in Figure 3.2b left, ~ 0.7 eV of the conduction band offset between ZnO and InP@$GS_2$ is likely to act as electron injection barrier. We solved this large band offset between ZnO and QDs by introducing conjugated polyelectrolytes, the solution-processible interfacial dipole layer (Figure 3.2b, right).[164],[163],[165],[166] Cao *et al.* reported that the conjugated polyelectrolytes lowered the work function of electrodes, probably due to the vacuum level shift by the interfacial dipole.[167] [168] In addition, importantly, good solubility of conjugated polyelectrolytes in polar solvents enables us to fabricate multilayered structures (i.e., ZnO nanocrystals/conjugated polyelectrolytes/colloidal QDs) by orthogonal solution processing. On the basis of versatility on HTL engineering as well as orthogonal processing capability, we fabricated InP QLEDs with the fully-tailored energy levels as follows; on top of ITO bottom cathode, ZnO

nanoparticles, PFN (conjugated polyelectrolytes chosen in the present study), and InP QDs are sequentially spin-coated. And then, 4,4',4''-tris(N-carbazolyl)-triphenylamine (TCTA), molybdenium oxide ($MoO_3$), and Al electrode were successively evaporated. TCTA was chosen as the hole transporting materials, owing to the suitable low highest-occupied molecular orbital (HOMO) level (5.7 eV)[140] adjacent to the valence band of InP@$GS_2$ QDs.

The formation of interfacial dipole and corresponding shift of vacuum level ($\Delta$) by PFN were confirmed from UPS measurement, as depicted in Figure 3.4a. Investigation of high binding energy cutoff regions of ITO/ZnO/PFN thin films allowed us to confirm the interfacial dipole that was gradually increased and saturated to ~ 0.6 eV at 1.5 mg $mL^{-1}$ of PFN solution (Figure 3.3a, inset). This concentration dependence and saturation behavior seemed to be related to the surface coverage of PFN chains on ZnO nanocrystals. Negligible change in surface morphology and roughness observed by atomic force microscopy in Figure 3.3 implies that PFN covers each ZnO nanocrystal in molecular level, rather than forming tens of nanometer-thick films. Nevertheless, the change in water contact angle clearly reflects the increasing amount of hydrophobic PFN chains on ZnO nanocrystals with increasing concentration of PFN solution. The extent of interfacial dipole and its arrangement were similar with the previous reports (i.e., ITO/PFN[163] or ITO/ZnO/quaternized PFN[169]) and effectively reduced the electron injection barrier between ZnO and InP QDs.

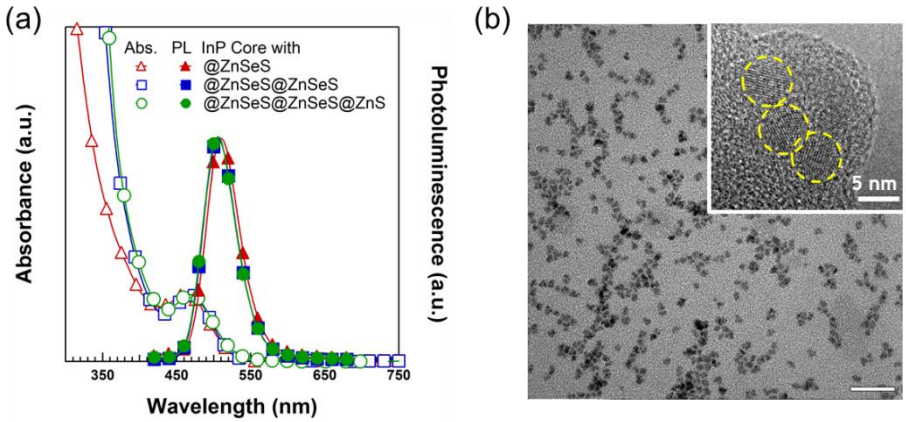


**Figure 3.1** (a) Absorption (open) and photoluminescence (filled) spectra of InP QDs with single (red), double ZnSeS shells (blue), and final QDs (green) (b) A TEM image of final InP QDs. Inset is a high-resolution TEM image of (b) (avg. d = 4.6 nm).

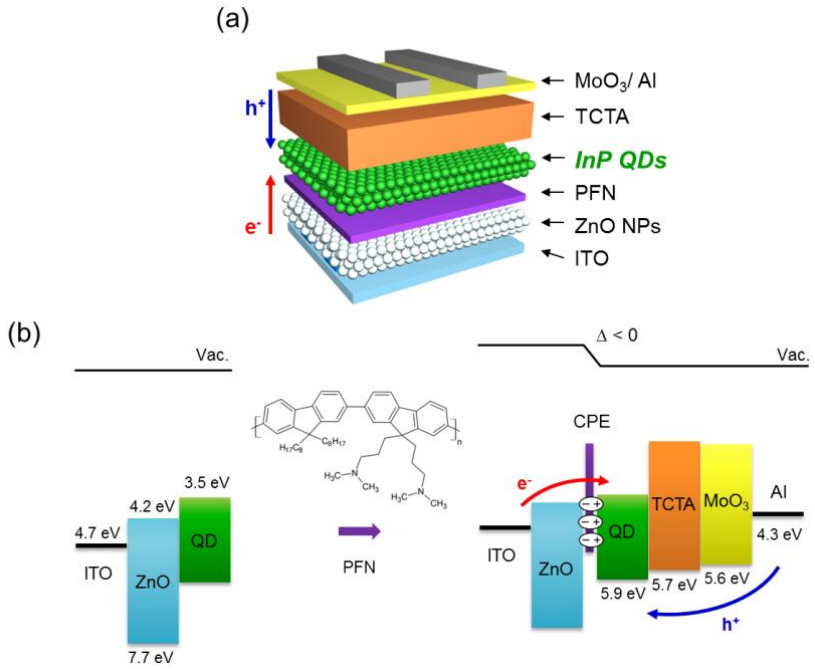


**Figure 3.2** (a) Schematic on InP QLEDs based on the ZnO/PFN electron injection layer. (b) A HR-TEM image of InP QDs with optimal ZnSeS composition gradient shells (InP@$GS_2$). (c) Schematic energy-level diagrams near the ZnO/QD interface with and without the PFN layer.

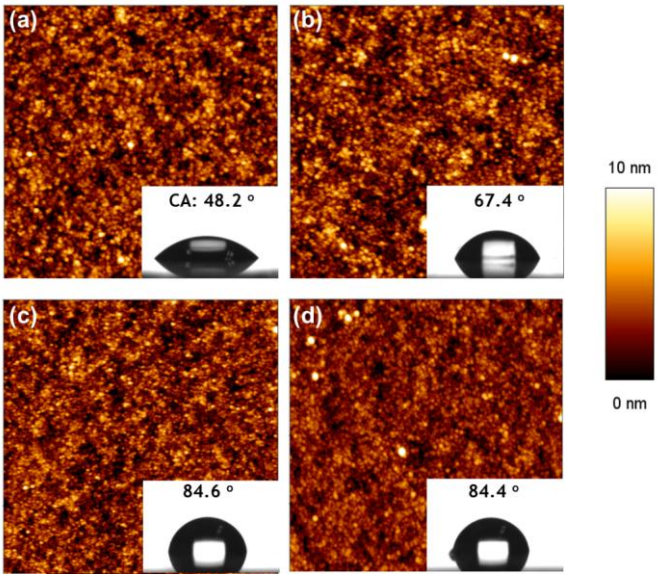


**Figure 3.3** AFM height images and water contact angle (inset) of ZnO/PFN thin films fabricated with (a) 0, (b) 0.5, (c) 1.0, and (d) 1.5 mg $mL^{-1}$ of PFN solutions.

To investigate the effect of vacuum level shift on electron injection behaviors, turn-on voltage ($V_{ON}$) and current density (*J*)–voltage (*V*)–luminance (*L*) characteristics of InP@$GS_2$-based devices were examined as a function of the concentration of PFN solution (Figure 3.4b). Interestingly, the 0.5 mg $mL^{-1}$ of PFN considerably lowered $V_{ON}$ from 2.8 V to 2.2 V and increased *J* and *L* compared with a PFN-free device, but instead, further increase in the amount of PFN led to the opposite effect in spite of the reduced electron injection barrier. This reciprocal tendency of $V_{ON}$ originates from lowest unoccupied molecular orbital (LUMO) of PFN, locating ~ 1.6 eV higher than ZnO. As a result, increase in PFN on ZnO nanocrystals acts as a resistance and strongly impedes the electron injection from ZnO to InP@$GS_2$ QDs. Consequently, the lowest $V_{ON}$ by small amount of PFN was resulted from the complementary effect of i) reduction in the electron injection barrier between ZnO and InP@$GS_2$ and ii) increase in the resistance by PFN.

Careful optimization of the PFN layer resulted in the considerable improvement in EQE of InP QLEDs. As shown in Figure 3.4c, the presence of PFN distinctively reduced the electron injection barrier, and consequently, improved the formation of excitons in InP QDs through the direct carrier injection in entire operation range. Although further increase in the concentration of PFN beyond optimal condition also enhanced EQE at low current density regime, raise in the resistance by PFN layer lowers an overall EQE level and luminance of devices. Reversal of EQE between the devices without PFN and with large amount of PFN (at ~ 10 mA $cm^{-2}$, blue and yellow markers in Figure 3.4c) reflected the effect of interfacial resistance on

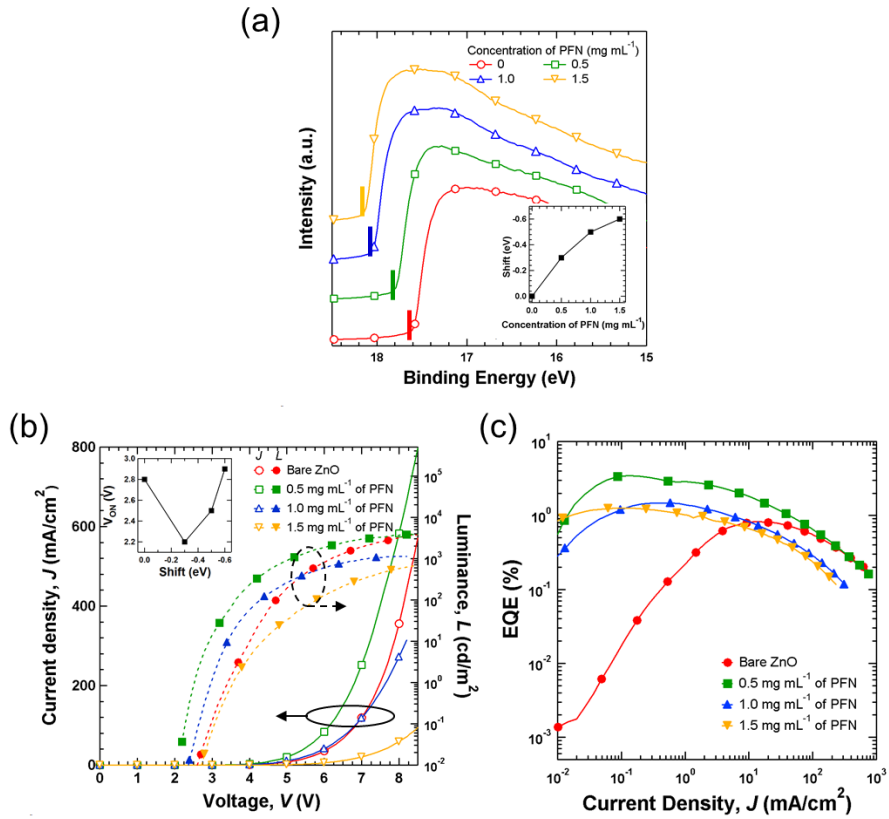


**Figure 3.4** (a) High binding energy cutoff region in UPS spectra of a bare ZnO film and PFN-coated ZnO films. Inset is a trend on vacuum level shift (Δ) varied by concentrations of PFN solutions. All spectra are referenced to the Fermi energy level of Au (111) surface. (b) *J*-*V* and *L*-*V* characteristics of QLEDs as a function of the concentration of PFN solution. Inset is turn-on voltages of QLEDs as a function of vacuum level shift. (c) EQE-*J* characteristics of QLEDs varied by the concentration of PFN solution (closed markers with solid lines) and the number of ZnSeS composition gradient shells (n) of QDs (open markers with dashed lines).

EQE, prohibiting facilitated injection of electrons into QDs. The resulting InP QLEDs with optimized amount of PFN (0.5 mg $mL^{-1}$) and InP@$GS_2$ QDs showed 3.46% of maximum EQE and 3,900 cd $m^{-2}$ of maximum brightness without any parasitic peaks from adjacent PFN and TCTA layers (Figure 3.5a). Particularly, distinct improvement of direct carrier injection at low applied bias enabled to realize large-area (1.2 cm x 1.2 cm) and flexible InP QLEDs with bright green emission in entire pixel (Figure 3.5b). The summarized performance data of InP QLEDs are listed in Table 1.

It is worth to note that the electroluminescence of QD-LEDs here emitted pure electroluminescence spectra from QDs, but long-tail emission was observed at high operation voltage (or current density). In the previous reports on Cd-based ones, In the previous reports, such surface state emission has been mainly due to the absence of shells[170] or accumulation of excess charge carriers on surface states by large carrier injection barrier.[171] However, relevant alignment of energy levels in the present device and no signature of surface states in film PL exclude those possibilities.

In core@shell QDs, the shell provides the potential barrier confining carriers which governs the extent of exciton delocalization to surface states or electronic coupling between QDs.[172] In terms of dot-do-dot spacing, increase in shell thickness reduces energy/charge transfer between QDs.[173-174] Considering that InP QDs present here have light electron effective mass (i.e., $m_e$ = 0.077 for InP and 0.13 for CdSe) and small conduction band offset between InP and ZnSeS (below 0.3 eV[155]), the exciton or charge carriers in InP QDs is likely to delocalize to surface states or surroundings (i.e., adjacent

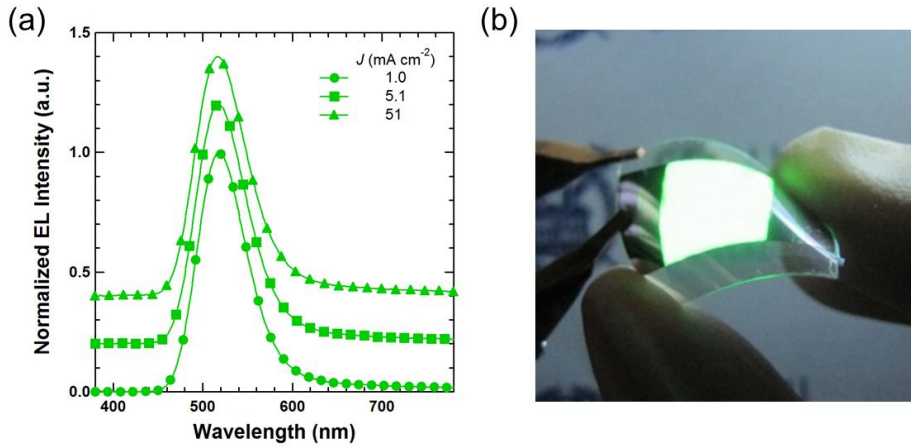


**Figure 3.5** (a) Normalized EL spectra of InP QLEDs comprising of InP@$GS_2$, as a function of current density (*J*). (b) A demonstration of large-area InP QLEDs on flexible polyethersulphone (PES) substrate (pixel size: 1.2 cm x 1.2 cm) at 5.5 V of applied bias.

**Table 3.1** Optical properties and device performance of InP QLEDs according to the concentration of PFN.

| QE (before/after) (%) | Shell Thickness (nm) | PL $\lambda_{max}$ /FWHM (nm) | EL $\lambda_{max}$ /FWHM (nm) @ 1 mA $cm^{-2}$ | PFN (mg $mL^{-1}$) | $V_{on}$ (V) | Peak E QE (%) | Max. LE (cd $A^{-1}$) | Max L (cd $m^{-2}$) |
|---|---|---|---|---|---|---|---|---|
| 0.72 / 0.65 | 1.7 ± 0.2 | 506/51 | 518/64 | 0 | 2.8 | 0.83 | 1.53 | 4,182 |
| | | | | 0.5 | 2.2 | 3.46 | 10.9 | 3,900 |
| | | | | 1 | 2.5 | 1.47 | 4.6 | 1,138 |
| | | | | 1.5 | 2.9 | 1.26 | 3.06 | 801 |

*Abbreviations and their meanings: QE (quantum efficiency before/after purification), PL (photoluminescence), EL (electroluminescence), $V_{on}$ (turn-on voltage), EQE (external quantum efficiency), LE (Luminous efficiency), and L (Luminance).

QDs or charge transport layers), compared with common CdSe/ZnS QDs. Therefore, electrons existed in InP QDs under device operation can be easily escape from the core region of QDs and recombine with free charge carriers at the surface states of QDs during device operation. It is supported that this surface state-related emission was significantly observed from the devices with poor EQE due to the imbalanced carrier injection or the devices comprising of InP QDs with thin ZnSeS shells. We believe that the advance in device structure for balanced carrier injection and novel structural design of InP QDs with III-V shells (i.e., GaN) naturally overcomes the surface-state emission in EL spectrum.

### 3.4 Conclusions

In summary, we realized the efficient and bright InP QLEDs comparable with previous Cd-based ones through the advanced synthetic method for InP QDs as well as the optimized device architecture. To facilitate the balanced carrier injection, thin PFN layer was intervened at ZnO/QD interface to introduce interfacial dipole. The PFN led to the vacuum level shift, leading to the reduction of electron injection barrier from ZnO to QDs. Owing to the extensive consideration on the material design and device structure, the QD-LEDs demonstrated here represented the maximum EQE of 3.46% with a maximum luminance of 3,900 cd $m^{-2}$, one of great advance among QD-LEDs based on InP QDs so far.

# Chapter 4. Stepwise Formation of CdSe Tetrapod:P3HT Bulkheterojunction for Hybrid Solar Cells

## 4.1 Introduction

Shape-controlled semiconductor nanocrystals have been extensively utilized in organic-inorganic hybrid solar cells in order to harness superior optical and electrical properties of inorganics using solution process. Since the CdSe rod-Poly(3-hexylthiophene) (P3HT) blend system was proposed by A. P. Alivisatos et al.[26], research on nanocrystal shape (e.g., dots, [175-176] [70, 177-179] rods, [180-182] tetrapods, [27, 29, 31, 183-184] hyper-branched nanocrystals[185]), device structure (e.g., use of metal oxide buffer layer[186]) or surface passivation process (e.g., thiols[182, 187] or amines[70]) has been emerged to improve photon-to-electron conversion efficiency. Based on those accumulated knowledge, more recently, the low bandgap conducting polymers[29, 31] have been synthesized for harvesting infrared region of solar spectrum in a framework of organic-inorganic hybrid solar cells.

In the conventional scheme for organic-inorganic hybrid solar cells, tetrapods (TPs) are modified with pyridine or amines for eliminating insulating surface ligands and blended with conducting polymers to achieve BHJ morphologies through the vertical segregation of nanocrystals. [26, 70, 180, 185, 187] The elimination of surface ligands is an essential step for improving interfacial contact between nanocrystals and conducting polymers directly. However, the absence of surface ligands fades the colloidal stability of TPs

and results in massive aggregates of nanocrystals during fabrication process, which is harmful to the uniformity, reliability and reproducibility of final devices.

In order to overcome the difficulty on the fabrication process mentioned above, the sequential deposition of CdTe TPs and P3HT was suggested by I. Gur et al.[28] They formed a TP monolayer on bare ITO substrates using bifunctional linkers, and filled empty void space with polymers *via* spin-coating process. This approach seems to be conceptually reasonable to realize easy and well-controlled fabrication process, but there are some constrains for achieving high device performance; their ideal model is only achievable when the quality of TPs is guaranteed, such as a long arm length covering all active layer thickness and high morphological uniformity for maximizing vertical orientation. Even if the TPs are repeatedly deposited to covering the whole active layer, intervening linker prevents smooth carrier transport through the TP arms. From the viewpoint of device structure, the absence of buffer layer is also problematic due to carrier loss and exciton quenching at ITO/active layer interface that shrink device performance. Nevertheless, the sequential deposition approach enables us to establish more reproducible and reliable fabrication of organic-inorganic hybrid solar cells thanks to the excellent colloidal stability of nanocrystals once those obstacles are resolved.

Herein, we suggested the advanced methodology for the sequential formation of organic-inorganic hybrid solar cells in a practical way. From the viewpoint of material preparation, we utilized the continuous precursor

injection approach for synthesizing arm length-controlled CdSe TPs with high morphological uniformity. Following, the stepwise fabrication process was established that separates thin film fabrication, surface modification, and formation of BHJ morphology; using the CdSe TPs capped with easily detachable oleylamine ligands, porous TP thin films were spin-casted to the substrate. And then, sequential rinsing and thermal annealing step improves the electrical property of CdSe TP networks, which eliminates insulating ligands as well as induces direct contact between TPs. Lastly, spin-coating of conducting polymer yielded the organic-inorganic BHJ morphology. In the point of device architecture, we employed a ZnO nanoparticle buffer layer below those BHJ active layers, not only due to the robustness against repeating solvent rinsing and thermal annealing but also their optical transparency in visible-infrared region.

The separation of fabrication process into the thin film formation, surface modification, and BHJ formation provides a clear framework for understanding the complex correlation between nanoscopic morphology, surface chemistry of nanocrystals, and device physics on the operation of solar cells. In the conventional framework, the introduction or elimination of surface ligands can affects the aggregation/dispersion morphology of nanocrystals in a polymeric matrix, so the effect of surface ligands on device performance cannot be directly correlated.[70] In contrast, the methodology suggested here excludes such complexity by separating nanostructure formation with surface passivation, thus, we clearly study on the effect of surface passivation on the device performance. Based on this clarity, we found

out the primary amine was the most effective ligands for the surface passivation of CdSe, directly affecting the recombination phenomenon of charged carriers. We believe that the methodology suggested here is highly beneficial for understanding of organic-inorganic hybrid solar cells as well as harnessing their full potential using low bandgap polymers.

## 4.2 Experimental section

**Materials** For the synthesis of CdSe tetrapods, cadmium oxide (CdO, 99.95%) was purchased from Alfa Aesar. Selenium (99.99%, powder), n-trioctylphosphine (TOP, 90%), oleic acid (OA, 90%), 1-octadecene (ODE, 90%), zinc acetate dehydrate ($Zn(ac)_2 \cdot 2H_2O$, 98%), potassium hydroxide (KOH, 90%), and cetyltrimethylammonium bromide (CTAB, 99+ %) were purchased from Sigma Aldrich. All chemicals were used as purchased.

**Synthesis of ZnO nanoparticles** ZnO nanoparticles were synthesized by modifying the method reported by Pacholski *et al.*[159] Firstly, 3 g of $Zn(ac)_2 \cdot 2H_2O$ and 120 mL of methanol were placed in 3-neck round bottom flask and heated to 60 $^oC$. At that temperature, 60 mL KOH solution containing 1.51 g of KOH was added dropwise into the $Zn(ac)_2 \cdot 2H_2O$ solution with strong agitation. The reaction mixture was kept at 60 $^oC$ for 2 hr 15 min. At the end of reaction, the product appeared as a milky solution. After precipitating the product by centrifugation at 4,000 rpm, the product was washed with methanol twice. Finally, the product was centrifuged again and redispersed in 5 mL of butanol.

**Preparation of injection solution** For the preparation of cadmium oleate ($Cd(OA)_2$) solution, 10 mmol of CdO, 7.8 mL of OA, 6.2 mL of ODE, and 1 mL of TOP were placed in an 100 mL 3-neck round flask coupled with a condenser. The mixture was heated to 280 °C under $N_2$ flow for 20 min. After the mixture was optically clear, the round flask was cooled down to 50 $^oC$ and added 0.14 mmol of CTAB under $N_2$ flow. Separately, 12 mmol of Se and 6

mL of TOP were mixed in a 50 mL 2-nect round flask with a condenser and heated at 200 $^{o}$C until the mixture became transparent solution. After the TOPSe was cooled down to room temperature, 5 mL of TOPSe solution was added to $Cd(OA)_2$ solution and the mixed solution was stirred them for 5 minutes.

**CdSe seeds with zincblende crystal structure**. Modified synthetic procedure[122] was employed to prepare CdSe seeds with zincblende crystal structure. Firstly, 0.5 mmol/mL of $Cd(OA)_2$ solution was prepared by reacting 5 mmol of CdO, 5 mL of OA, and 5 mL of ODE with the same reaction condition described above. Next, 1 mmol of Se and 10 mL of ODE were loaded into 100 mL 3-neck round flask and heated up to 300 $^{o}$C under $N_2$ flow. When the Se/ODE solution become optically clear, 4 mL of $Cd(OA)_2$ solution (2 mmol) was rapidly injected into the solution and reacted at 270 $^{o}$C for 15 min. Finally, 6 mL of ODE was added into the seed solution and cooled down to room temperature.

**Synthetic procedure for CdSe tetrapods in terms of CPI Approach**. For the 40 nm-long CdSe tetrapods, 5 ml of seed solution, 2.25 mL of OA, 1.5 mL of TOP, 21.25 mL of 1-ODE, and 0.21 mmol of CTAB were placed in 3-neck round flask with condenser, followed by heating up to 260 $^{o}$C. When the temperature is reached at 260 $^{o}$C, 28 mL of injection solution was added into the seed solution with 0.5 mL/min of injection rate. After 40 min of the reaction, the temperature was set to 280 $^{o}$C and reacted for 16 min. For the 80 nm-long CdSe tetrapods, 2.5 mL of seed solution, 2.25 mL of OA, 1.5 mL of TOP, 23.75 mL of 1-ODE, and 0.21 mmol of CTAB were placed in 3-neck

round flask, then heated up to 280 $^{o}$C. At the elevated temperature, 30 mL of injection solution was injected into the reactor in stepwise manner: 0.5 mL/min for 6 min, 0.6 mL/min for 6.67 min, 0.7 mL/min for 8.57 min (in this step, the temperature was set to 280 $^{o}$C) and 0.8 mL/min for 8.75 min. In a case of 103 nm-long CdSe tetrapods, 1.67 mL of seed solution, 2.25 mL of OA, 1.5 mL of TOP, 24.58 mL of 1-ODE, and 0.21 mmol of CTAB were loaded in 3-neck round flask, then heated to 260 $^{o}$C. At the elevated temperature, 40 mL of injection solution was introduced into the seed solution with controlled injection rate: 0.4 mL/min for 5 min, 0.5 mL/min for 12 min, 0.6 mL/min for 6.67 min, 0.7 mL/min for 5.71 min and 0.8 mL/min for 30 min (in this step, the temperature was set to 280 $^{o}$C). In order to purify the product, 2 mL of chloroform and an excess amount of acetone were added into the resulting solution until the solution became turbid, which was precipitated by centrifugation at 3,000 rpm. After the centrifugation the supernatant was decanted and the precipitate was re-dispersed in organic solvent such as chloroform, toluene, or hexane. The precipitation and re-dispersion was repeated until the samples were sufficiently purified.

**Surface modification process with $HBF_4$ and oleylamine** 5 mL of CdSe tetrapod dispersion (40 mg/mL) was precipitated with excess ethanol and centrifugation at 3000 rpm, supernatant was discarded. Then, the precipitate was dissolved with 5 mL of hexane, and added with 5 mL of N,N-dimethylformamide (DMF). Next, 0.5 mL of $HBF_4$ solution (48 wt% in $H_2O$) was added into the mixture and shaked for 30 sec. Because hexane and DMF/$H_2O$ solution were immiscible, the resulting mixture was separated into

two phases; clear upper layer (hexane) and dark lower layer (CdSe tetrapods in DMF/$H_2O$ mixture). After removing upper clear phase, 5 mL of hexane was added and the mixture was shaked again to wash out oleate ligands in the DMF/$H_2O$ phase. Repeating this washing step three times, the mixture was precipitated with excess amount of acetone. For the complete removal of oleate ligands, $HBF_4$ treatment was conducted twice. At the end of $HBF_4$ treatment, the bare CdSe tetrapods were precipitate with excess acetone and redispersed in chloroform/oleylamine mixture (chloroform : oleylamine = 8 : 2, in volume ratio). After 10 minutes, the excess amount of acetone was added to CdSe tetrapod dispersion, and centrifuged at 3000 rpm to remove excess oleylamine. Finally, the preciptates was re-dispersed in 2 mL of chloroform. In order to confirm the concentration (in mg/mL), 0.2 mL of small aliquot was extracted from the CdSe tetrapod dispersion and dried for 20 min at 90 $^oC$. The final concentration of CdSe tetrapod dispersion was about 40 mg/mL.

**Fabrication of porous CdSe tetrapod thin films on ZnO buffer layer**

Firstly, ZnO nanoparticles in butanol were spun on ITO substrates at 2000 rpm for 60 sec and dried in $N_2$ atmosphere at 100 $^oC$. Then, CdSe tetrapod dispersion were deposited by spin-coating at 2000 rpm for 30sec, followed by annealing at 150 $^oC$ for 20 min under Ar atmosphere. After the annealing is finished, the substrate was quenched to room temperature and washed twice with ethanol by spin-coating at 2000 rpm. For the complete fixation of CdSe tetrapods on ZnO thin film, the washed substrate was annealed at 150 $^oC$ for 10 min under Ar atmosphere. The resulting ZnO/CdSe tetrapod thin films can be preserved from next surface treatment or spin-coating processes.

**Depth profile measurement using Auger electron spectroscopy** Atomic contents of ZnO/CdSe tetrapod:P3HT thin films on a Si wafer were characterized by Auger electron spectroscopy (PHI 660, manufactured by Perkin-Elmer), equipped with $LaB_6$ electron gun, Ar ion beam and cylindrical mirror analyzer.

**Fourier transform-infrared spectroscopy (FT-IR) measurement** Pristine and $HBF_4$-treated CdSe tetrapods were prepared followed by experimental procedure mentioned above, and dropped on dual side-polished Si wafer. And then, FT-IR data were taken with a Perkin Elmer Frontier FT-IR spectrometer.

**Plain and cross-sectional image of CdSe tetrapod thin film** CdSe tetrapod thin films were fabricated on n-doped Si wafer with native oxide layer and dried under vacuum overnight. For the cross-sectional image, as-prepared films were cut by hands and placed on a vertical sample holder. The image was taken with a Carl Zeiss SUPRA 55VP.

**Fabrication of photovoltaic device** Surface passivation ligands dissolved in acetone (acetone : ligands = 8 : 2, in volume ratio) was spin-coated on CdSe tetrapod thin films twice Then, the resulting substrates were dried at 100 $^oC$ for 10 min under Ar atmosphere. Next, 2 wt % of P3HT in monochlorobenzene was spin-coated on those substrates at 1000 rpm for 30 sec, followed by thermal annealing at 150 $^oC$ on hot plate for 15 min in Ar atmosphere. Finally, 10 nm of $MoO_3$ layer and 100 nm of Al electrodes were deposited via thermal evaporation.

The current density-voltage (J–V) characteristics of the solar cells were measured with a Keithley 237 source measurement unit. The solar cell

performances were characterized under AM1.5G condition with an illumination intensity of 100 mW/cm$^2$ generated by a Newport 91160A solar simulator. J-V characteristics of the cells with illumination were measured using a metal mask of 0.09 cm$^2$. The intensity dependent measurements have been performed with various neutral density filters.

Incident photon to current conversion efficiency (IPCE) was measured using Oriel QE/IPCE Measurement Kit which composed of 300W Xenon Lamp, monochromator(74125), the order sorting filter wheel, the Merlin lock-in amplifier(70100) and the chopper. UV–Vis spectra of the P3HT:CdSe NCs films were taken with a Beckman DU-70 spectrophotometer and film morphology was analyzed with atomic force microscopy (AFM, Park Systems XE-100).

## 4.3 Results and Discussions

Fabrication concept and final device structure in the present study is depicted in Scheme 1. In step I, CdSe TPs capped with oleylamine were spun on top of a ZnO hole blocking buffer layer (ca. 20 nm) on ITO cathode. And then, insulating ligands on CdSe TPs are removed to ensure electrical contact between TPs or between TPs and conducting polymers. In the following step II, P3HT was filled the voids in the CdSe TP thin film. For the complete device operation, we adopted molybdenum oxide ($MoO_3$, 10 nm) and aluminium (Al, 100 nm) on top of this hybrid layer, as an electron blocking layer and an anode. This configuration, named as inverted device structure, ensures the extraction of charge carriers from resulting hybrid morphology. Because n-type CdSe domain is directly connected to the lower part of devices and P3HT covers the upper part of the CdSe domain, photogenerated electrons are needed to be extracted via bottom electrode.

In step I, there are two important requisites in terms of nanoscopic morphology as well as electrical property of inorganic domain. Firstly, lengthy CdSe TPs with high morphological uniformity need to be prepared to facilitate carrier transport within hybrid active layer and ensure sufficient junction area. Low shape selectivity (i.e., presence of many dots or rod shaped nanocrystals) or too-short arms could increase the junction point between TPs, thus impede facilitated carrier transport between them. In terms of porosity, many branches can effectively restrict the rotational and positional degrees of freedom during spin-coating process, thus kinetically-frozen porous TP layer

would be easily produced.[117] Secondary, a strategy for realizing interconnected TP networks without insulating ligands should be developed. However, processing of nanocrystals without stabilizing ligands is fairly hard; the nanocrystals without proper stabilization (i.e., steric stabilization by alkyl chains or charge-charge repulsion) unavoidably form large aggregates during the storage or processing of nanocrystal dispersion due to the Van der Waals attraction force between them. Particularly, TPs attract each other much stronger than dots, so that the bare TPs are likely to be precipitated. The layer-by-layer assembly is one of probable solution to achieve the porous TP films, but it requires long processing time (e.g., tens of minutes) to assemble hundreds nanometer of film thickness. Moreover, bifunctional linkers necessary for layer-by-layer perhaps interfere carrier transport between TPs.

Recent progress in the synthetic method of semiconductor nanocrystals enables us to easily overcome the requirements on material preparation. In the present study, we prepared CdSe TPs with high morphological uniformity and controllability based on continuous precursor injection approach. Controlling in the injection rate of precursors and reaction temperature, lengthy CdSe tetrapods with ~ 90% of shape selectivity could be successfully synthesized, as shown in Figure 4.1. The arm length-controlled tetrapods, from 40 nm, 76 nm, to 103 nm, have shape selectivity above 90 % and low deviation in arm length as well as diameter ($\sigma < \sim 3$ nm for length, 0.4 nm for arm diameter). The CdSe TPs used here were targeted to maximize light absorption in visible range, thus the arm diameter reached over 8 nm,

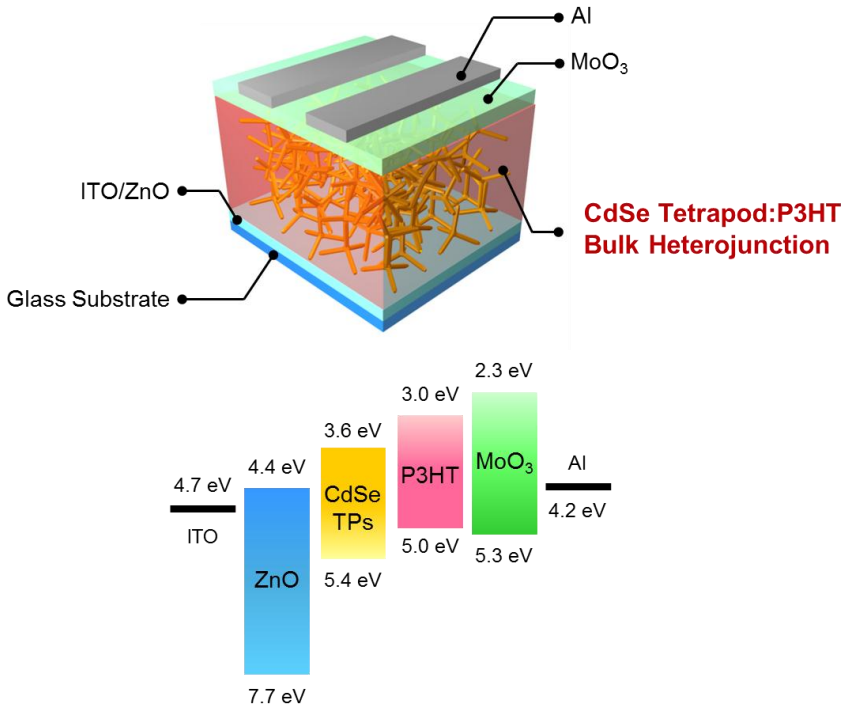


**Scheme 4.1** (top) A schematic on a device structure of CdSe tetrapod:P3HT bulk heterojunction (BHJ) solar cells and (bottom) energy level diagram of CdSe Tetrapod:P3HT BHJ solar cells with an inverted device structure.

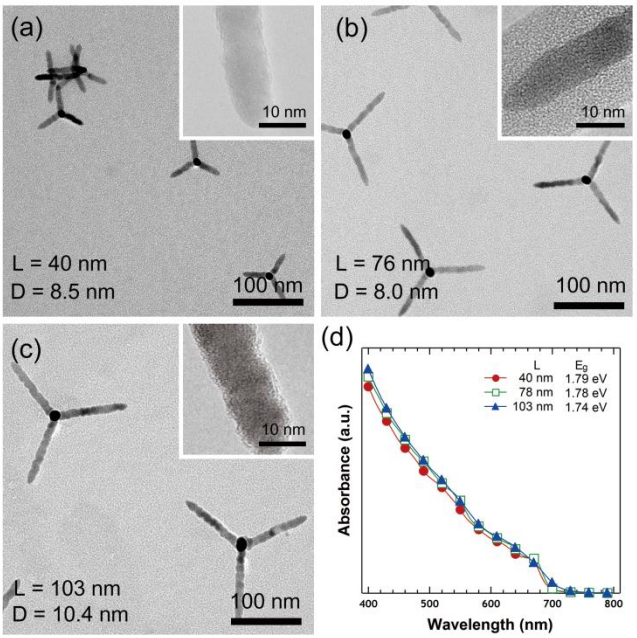


**Figure 4.1** (a-c) TEM images of CdSe tetrapods with controlled arm length and diameter. (d) Absorption spectra of CdSe tetrapods shown in (a-c).

above exciton Bohr radius of CdSe (~ 5.6 nm).[188] We found that CdSe TPs with arm diameter below 3 nm was too fragile to stand for spin-coating process.

The second requirement, fabrication of interconnected CdSe TP thin films without insulating ligands, was accomplished through strategic ligand exchange of oleate ligand with oleylamine ligand. As-synthesized CdSe TPs are capped with oleate ligands (Cd-OCOR) and they are strongly bound to Cd atoms on the surface. In spite of the beneficial stabilization effect of oleate ligand, however, those ligands are only removed by chemical exchange with other proton-donating ligands (i.e., carboxylic acids or phosphonic acids) or inefficient etching pathway with amine species (i.e., pyridine). Such reactive environment would causes undesired damages to beneath buffer layer or TP layer itself, for instance, dissolution of ZnO or TP nanoparticles during surface treatment or crack formation by rapid volume contraction. Whereas, primary amines with long alkylchain have sufficient affinity to CdSe nanocrystals, but their binding nature is obviously different from oleate ligand; an electron lone pair at nitrogen atom interacts with surface Cd atoms by chemical equilibrium. Namely, the amount of bound amines is influenced by the concentration of primary amines in a solution and the intervention of proton containing species capable of hydrogen bonding (i.e., alcohols) facilitates desorption of primary amines. Therefore, stripping of oleylamines on CdSe TPs can be conducted by more mild and simple process benign for beneath buffer layer.

Figure 4.2a displays the ligand exchange procedure of CdSe tetrapods with oleylamine.[189] Firstly, the oleate ligands were replaced with $HBF_4$ in solution phase, which donated protons to carboxylate groups and replaced the oleate ligands with $BF_4^-$. Removal of oleate ligands resulted in the precipitation of CdSe TPs, due to insufficient charge-charge repulsion in DMF. Repeating $HBF_4$ treatment considerably decreased the oleate ligands on TPs, examined by the reduced vibrational peaks from alkylchains after $HBF_4$ treatment in Figure 4.2b. And then, once the oleylamine and nonpolar solvent were added to the precipitates, then the TPs were well-dispersed in solvent by steric stabilization provided by oleylamine. The oleylamine-capped CdSe TPs showed optically-clear dispersion without any change in optical property and morphological uniformity. We note that shorter amines such as butylamine, hexylamine, or octylamine hardly stabilize TPs with long arms over 70 nm and oleylamine works effectively.

As-synthesized CdSe tetrapods are capped with oleate ligands which are strongly bound to Cd atoms on the surface (Scheme 4.2a, left). Although those long alkylchains are the essential component to preserve the colloidal stability of CdSe tetrapods, it cannot be easily removed from the nanocrystal surface by simple washing (i.e., precipitation/redispersion method or two-phase extraction)[190], desired in the second step. Ligand exchange of those strongly-bound oleate ligands with primary amine ligands could be a good approach to solve this problem. It is well-known that the bonding between primary amines and surface Cd atoms is sufficiently strong to stabilize nanocrystals, but their chemical nature is far different from the oleate ligands.

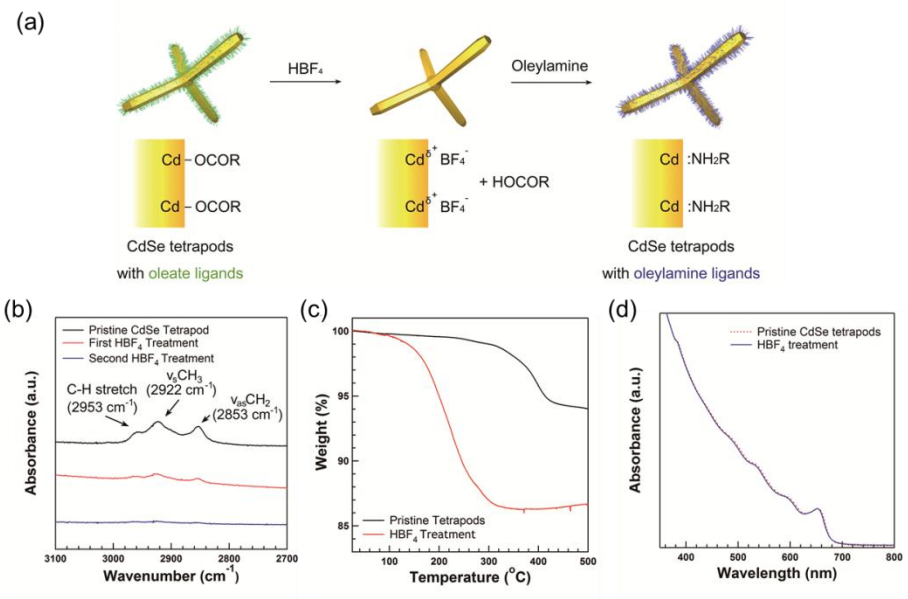


**Figure 4.2** (a) A schematic on two-step ligand exchange of CdSe TPs. (b) FT-IR spectra of CdSe TPs with repeating $HBF_4$ treatment. (c) TGA curve of pristine and $HBF_4$-treated CdSe TPs. (d) Absorption spectra of pristine and modified CdSe TPs in chloroform.

The primary amines interact with surface atoms by chemical equilibrium, influenced by the concentration of primary amines in a solution. Therefore, repeated washing of oleylamine-capped TP thin films with solvents can effectively remove the oleylamine, which drives the chemical equilibrium to desorption of surface ligands.

Figure 4.2a represents the ligand exchange procedure of CdSe tetrapods with oleylamine.[189] The oleate ligands are replaced with $HBF_4$ in solution phase, which donates protons to carboxylate groups and replace the oleate ligands as a form of $BF_4^-$. Repeating $HBF_4$ treatment considerably decreased the oleate ligands on TPs, examined by the reduced vibrational peaks after $HBF_4$ treatment in Figure 4.2b. Moreover, thermogravimetric analysis (TGA) of the $HBF_4$-treated CdSe TPs (Figure 4.2c) showed the distinctive difference. Whereas the pristine TPs lose their weight above 300 $^oC$ due to the thermal decomposition of oleate ligands, the modified one represented the reduced onset temperature around 100 $^oC$. It is attributed to the evaporation of solvents such as DMF, water, or ethanol that were used for $HBF_4$ treatment and purification. Following, once the oleylamine and nonpolar solvent were added to the precipitates, then the TPs were well-dispersed in solvent by steric stabilization provided by oleylamine. The oleylamine-capped CdSe TPs showed optically-clear dispersion without any change in optical property and morphological uniformity (Figure 4.2d). It was found that shorter amines such as butylamine, hexylamine, or octylamine hardly stabilized the CdSe TPs with long arms >70 nm and oleylamine worked most effectively.

On the basis of the as-prepared oleylamine-capped CdSe tetrapods, homogeneous CdSe TP thin films were fabricated by spin-coating and washed with ethanol, as presented in Figure 4.3a. As-casted tetrapod films on ZnO nanoparticle layers were annealed at 150 $^{o}$C for 20 min before washing and the washed films were annealed at 150 $^{o}$C for 10 min again. The thermal annealing of tetrapod films facilitated the weak fusion between ZnO/TPs or TPs/TPs, beneficial to improve electrical contact between them (Scheme 4.2b, right) as well as form robust inorganic networks resistive to the various organic solvents such as chloroform, toluene, or chlorobenzene that are good solvent for conducting polymers. After those annealing and washing process, the final TP thin films represented highly porous and homogeneous morphology as depicted in Figure 4.3b-d. It is clearly seen that the shorter tetrapods forms more dense films than the longer ones.

Through the simple spin-coating of P3HT solution, the void in TP thin films on ZnO layers could be easily filled without the collapse of lower ZnO and TP layers. It could be easily confirmed from the absorption spectra of films in Figure 4.4a. A characteristic shoulder of ZnO nanoparticles was obviously observed at ~ 350 nm for ZnO/CdSe TP and ZnO/CdSe TP:P3HT thin films. For the CdSe tetrapod layer, the strong absorption at UV-region was still remained in ZnO/CdSe TP:P3HT thin films. Persistence of CdSe TP layers could be confirmed from the removal of P3HT domain of ZnO/CdSe TP:P3HT thin films using chloroform. After washing out the P3HT domain, the absorption spectrum of washed film showed almost no difference with previous ZnO/P3HT layers (see red open square and green dashed line in

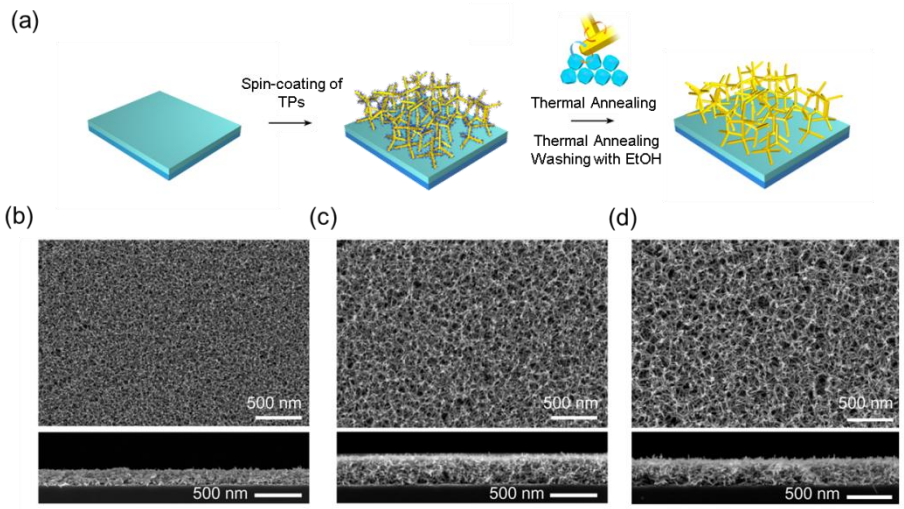


**Figure 4.3** (a) A schematic on the fabrication of porous CdSe TP thin films. Top (top) and cross-sectional SEM images (bottom) of final CdSe TP thin films comprising of (d) 40 nm, (e) 76 nm, and (f) 103 nm of arm length. All scale bars are 500 nm.

Figure 4.4a). And then, spin coating of P3HT solution on ZnO/TP thin films formed P3HT domain in the voids, as observed in Figure 4.4b-e. Depth profile of auger electron of sulfur covered entire range of film, from the onset of Cd signals to Si signals (Figure 4.4b), and cross-sectional SEM images clearly showed the P3HT filled in the voids (Figure 4.4c-e) for various TPs with different arm length. Therefore, we could conclude that the CdSe TP:P3HT BHJ was successfully constructed on a ZnO buffer layer.

In spite of the successful incorporation of P3HT domain, the resulting device recorded quite poor solar cell performance. For instance, power conversion efficiency of 0.91% was obtained from solar cells comprising of TPs with 76 nm of arm length. It is attributed to the presence of surface states of CdSe nanocrystals.[70] While primary amines have been proposed as surface passivation ligands for the solar cells containing CdSe nanocrystals, as mentioned in the introduction, the previous studies on the surface passivation of CdSe nanocrystals relied on the blending of surface-modified CdSe QDs and conducting polymers, and surface ligands on QDs could affect the morphology of QD aggregates in polymer matrix via enthalpic or entropic interaction with polymer interface.[191] In addition, the post treatments removing or replacing surface ligands affects not only to the dot-to-dot distance, but also to the surface states of QDs, resulting in the complexity involving aggregate morphology, dot-do-dot distance, and surface passivation. Regardless of the improved device performance by various pre- or post-treatment of CdSe:P3HT blend solar cells, such ambiguity have still remained as a bottleneck to understand photophysical phenomena and find

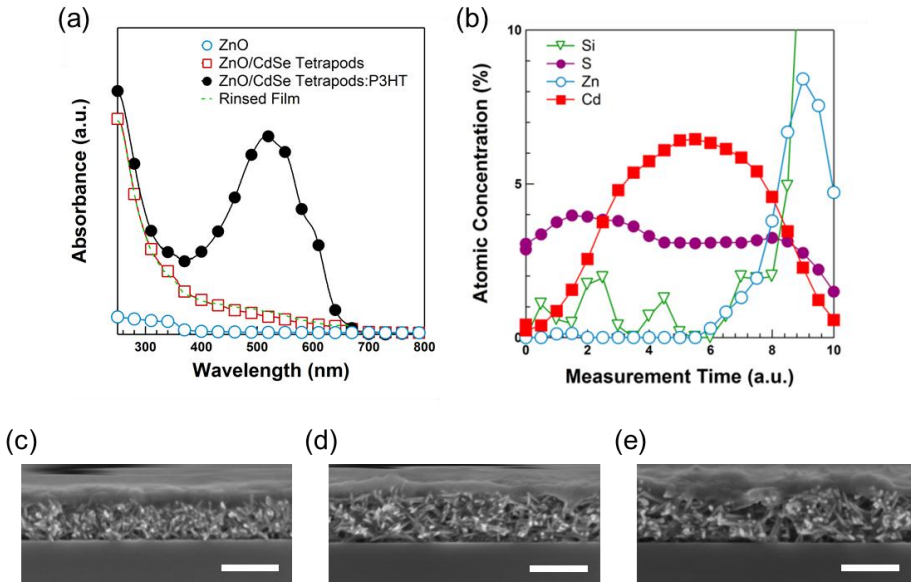


**Figure 4.4** (a) Absorption spectra of a ZnO (open blue circle), a ZnO/CdSe tetrapod (open red square), a ZnO/CdSe tetrapod:P3HT thin film (closed black dot), and a ZnO/CdSe tetrapod thin film acquired from ZnO/CdSe tetrapod:P3HT thin film, rinsed with chloroform. (b) Depth profiles Si, S, Zn, and Cd in ZnO/CdSe tetrapod:P3HT BHJ thin films taken by Auger electron spectroscopy. Samples in (a) and (b) were assembled with the TPs with 76 nm of arm length. Cross-sectional SEM images of ZnO/CdSe TP:P3HT thin films comprising of the TPs with (c) 40 nm, (d) 76 nm, and (e) 103 nm of arm length (scale bar: 200 nm).

a clue for efficient organic-inorganic hybrid solar cells.

To separate those variables and clarify the effect of surface states and their passivation on the device performance, we applied the representative surface ligands (e.g., hexylamine, hexanethiol, pyridine, and hexanoic acid) to the present device structure and explored the correlation of surface state – device characteristics in the viewpoint of carrier generation and recombination. Our approach can effectively excludes the morphological factors from the introduction of surface ligands, therefore, the change in PCE and device characteristics can be directly associated with the surface passivation effect.

Figure 4.5a and Table 4.1 shows current density (J) – voltage (V) characteristics and summarized results of solar cells with various surface passivation ligands. The solar cells passivated with pyridine and hexylamine had 1.5 and 2 times enhanced short circuit current density ($J_{SC}$) compared with the others, and particularly, hexylamine-treated one showed the highest fill factor (FF). Meanwhile hexanoic acid and hexanthiol did not affect the device performance. This drastic difference between amines and the others is attributed to the binding nature of those ligands of which possess X-type (carboxylic acid, alkylthiol) or L-type (amines) binding property to surface Cd atoms.[127, 190] The X-type ligands bind the nanocrystal's surface as a form of anion (i.e., carboxylate ($R\text{-}COO^-$) or thiolate($R\text{-}S^-$)) and exchanged with the other X-type ligands bound on the surface. In the present system, as-fabricated TP thin films lose X-type ligands (oleate ligands in the CPI approach) during $HBF_4$ treatment, so hexanoic acid and hexanthiol couldn't

bind to the CdSe surface by ligand exchange reaction and passivate surface states. In contrast amines interact with surface Cd sites by donating electron cloud, thus they are able to remain the nanocrystal's surface and passivate surface states.

In the meantime, hexylamine and pyridine affected the extent of surface passivation and open-circuit voltage ($V_{OC}$) differently; the passivation with hexylamine resulted in a large increase in $J_{SC}$ but decreased $V_{OC}$ slightly. By contrast, pyridine showed a less increase in $J_{SC}$ but $V_{OC}$ was unchanged. The difference in $J_{SC}$ is believed to be originated from the electron-donating property of aliphatic and aromatic amines. According to K. E. Knowles et al., surface ligands bound to Cd atoms generate molecular orbitals locating inside or outside bandgap, varied to the σ-donating character of amines. While the strong σ-donors widen the bonding-antibonding energy gaps and generate energy levels locating the outside of bandgap, the weak σ-donors generate antibonding orbitals locating the inside of bandgap.[192] In this framework, the aliphatic amine has stronger σ-donating character than aromatic amines, supported by the pKa values of amines (aliphatic primary amines: 10.6 and pyridine: 5.3), as a result, hexylamine can effectively eliminate surface states compared with pyridine. In contrast, pyridine seems to eliminates shallow surface states (near the conducting band edge), but could not fully remove deep surface states (near the middle of bandgap). In a case of $V_{OC}$, however, hexylamine seems to provide a larger resistance at CdSe/P3HT interface than pyridine, thus the hexylamine-treated solar cells represent lower $V_{OC}$ values than pyridine-treated one. Besides, the lowest $V_{OC}$ of hexanoic acid-treated

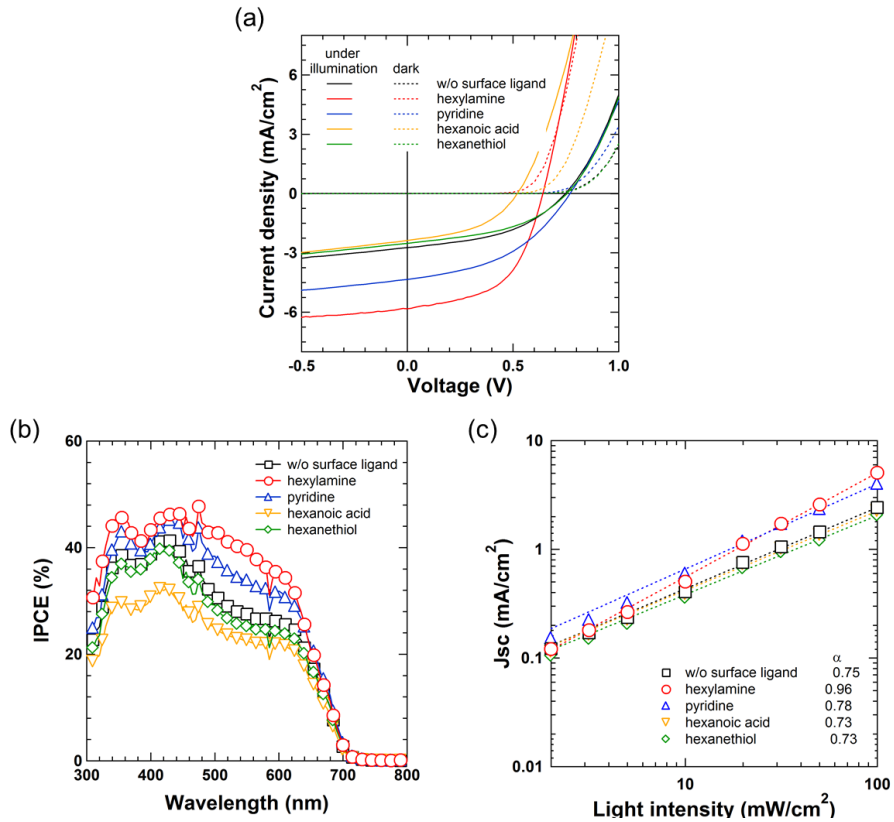


**Figure 4.5** (a) Current density (J) – voltage (V) characteristics, (b) Incident photon-to-current conversion efficiency (IPCE), and (c) light intensity dependence of short circuit current density of CdSe TP:P3HT BHJ solar cells comprising of CdSe tetrapod without surface ligands (black), passivated with hexylamine (red), pyridine (blue), hexanoic acid (yellow), hexanethiol (green). Dotted lines in (c) denote fitting line according to $J_{sc} \sim (I_{light})^{\alpha}$. The arm length of tetrapods was fixed to 76 nm and the thickness of CdSe TP:P3HT thin film was 230 nm.

**Table 4.1** Summary of current density ($J_{SC}$), open-circuit voltage ($V_{OC}$), fill-factor (FF), and power conversion efficiency (PCE) of CdSe tetrapod:P3HT BHJ solar cells in Figure 4.5.

| Passivation Ligands | $J_{SC}$ ($mA/cm^2$) | $V_{OC}$ (V) | FF (%) | PCE (%) |
|---|---|---|---|---|
| bare | 2.74 | 0.747 | 44.5 | 0.91 |
| hexylamine | 5.83 | 0.641 | 53.4 | 1.99 |
| pyridine | 4.34 | 0.769 | 43.7 | 1.46 |
| hexanoic acid | 2.37 | 0.520 | 45.3 | 0.56 |
| hexanethiol | 2.52 | 0.755 | 44.0 | 0.837 |

solar cells might be due to the excess hexanoic acid, which was not fully removed during drying step (at 100 $^{o}$C for 10 min) thanks to high boiling point (205 $^{o}$C).

The improvement by surface passivation ligands directly correlated with the incident photon to carrier conversion efficiency (IPCE), in Figure 4.5b. The IPCE of hexylamine and pyridine-treated solar cells were improved in entire wavelength and noticeable at the absorption region of P3HT (from 500 nm to 600 nm). It infers the reduction in surface states of CdSe nanocrystals influences the generation and transport of charged carriers, not only in the CdSe domain but also in the P3HT domain. In order to probe the effect of surface states on the fate of photogenerated charged carriers, we investigated a dependence of $J_{SC}$ on the light intensity (I) for the surface passivated solar cells (Figure 4.5c). $J_{SC}$ shows a power law dependence upon the light intensity I (e.g., $J_{SC} \propto I^{\alpha}$) and the exponent of I, α, indicates a carrier loss mechanism within the devices. When α = 1, the carrier recombination loss process is dominated by monomolecular recombination. When α = 0.5, in the meantime, the carrier recombination loss is dominated by bimolecular recombination.[193] [194] Assuming that the similarity of the present system follows the representative organic solar cells, the deviation of α from 1 (namely the contribution of bimolecular recombination) at $V_{OC}$ = 0 implies the presence of energetic traps that capture charged carriers and serves the recombination center. The effect of surface passivation was clearly observed in the dependence of $J_{SC}$ on the light intensity. As listed in Figure 4.5c, surprisingly, hexylamine-treated solar cells represented the highest α value,

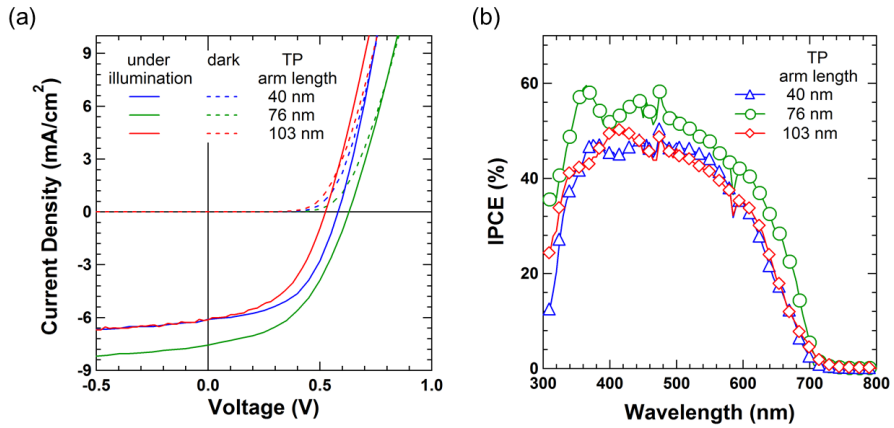


**Figure 4.6** (a) J-V characteristics and (b) IPCE curves of optimized CdSe TP:P3HT BHJ solar cells (Arm length / active layer thickness: 40nm / 190 nm for blue, 76 nm / 200 nm for green, and 103 nm / 210 nm for red).

**Table 4.2** Summary of current density ($J_{SC}$), open-circuit voltage ($V_{OC}$), fill-factor (FF), and power conversion efficiency (PCE) of CdSe tetrapod:P3HT BHJ solar cells with the arm length of 40 nm, 76 nm, and 103 nm, as shown in Figure 4.6.

| TP arm length (nm) | $J_{SC}$ ($mA/cm^2$) | $V_{OC}$ (V) | FF (%) | PCE (%) |
|---|---|---|---|---|
| 40 | 6.11 | 0.581 | 52.4 | 1.86 |
| 76 | 7.56 | 0.630 | 47.1 | 2.24 |
| 103 | 6.13 | 0.525 | 47.9 | 1.54 |

0.96, inferring that the major recombination originated from the geminate electron-hole pair (monomolecular recombination), not from the surface states (bimolecular recombination). By contrast, the other devices including pyridine-treated one showed less α value around 0.7, which means the coexistence of monomolecular and bimolecular recombination pathway. Conclusively, hexylamine was determined as the most suitable ligands for surface passivation of CdSe nanocrystals, leading to the undesired carrier recombination process via surface state-mediated energetic traps.

Based on the finding about surface passivation, we investigated the dependence of solar cell performances on the nanoscopic morphology of TP thin films. As we investigated above, the porosity was varied with the arm length of TPs and it would influence the P3HT domain size. Figure 4.6 and Table 4.2 shows the optimized devices comprising of TPs with 40 nm, 76 nm, and 103 nm of arm length. As confirmed in Figure 4.3b-d, TPs with shorter or longer arms form dense or sparse CdSe domain that directly influenced the size of P3HT domain. The dense TP morphology seems to prevent easy penetration of P3HT into the void, impeding the formation of BHJ in the entire film. While the sparse TP morphology might be beneficial to penetrate P3HT into the film, but it builds too large P3HT domain that reduces effective exciton dissociation at CdSe TP/P3HT interface. As a result, the solar cells with TPs with 76 nm of arm length represented the best performance due to suitable BHJ morphology. The best device (active layer thickness: 200 nm) showed 0.63 V of $V_{OC}$, 7.56 mA/cm$^2$ of $J_{SC}$, 47.1 % of FF, and 2.24 % of PCE.

## 4.4 Conclusions

So far, we demonstrated CdSe TP:P3HT BHJ solar cells with the new fabrication process. Based on the understanding of the binding modes of surface ligands on CdSe nanocrystals and well-controlled CdSe TPs with high morphological uniformity, inter-connected porous CdSe TP thin films without the insulating surface ligands were successfully prepared. And then, following spin-coating of P3HT solution on those films yielded well-defined CdSe TP:P3HT BHJ morphology. This separated fabrication of inorganic and organic domains serves a lot of advantages in terms of the reproducible and reliable fabrication, clear frameworks for understanding the device physics in organic-inorganic hybrid solar cells, and availability for the advanced hybrid solar cells with novel conducting polymers. Particularly, independent BHJ morphologies on the fabrication condition enabled us to prove that the primary amines were the most effective ligands for passivating surface states on CdSe nanocrystals, which minimized the undesired bimolecular recombination at the surface states acting as energetic traps. We believe that our finding and fabrication approach can improve the efficiency of organic-inorganic hybrid solar cells by applying the state-of-the-art low bandgap polymers and suggest the probable methodology for the novel optoelectronic devices based on the organic-inorganic hybrids.

# Chapter 5. Conclusion and Outlook

Ceaseless efforts on the preparation, characterization, and utilization of nanoscopic materials have opened huge possibilities to the unprecedented applications in various area ranging home appliances (e.g., solid-state lighting or display), energy conversion (e.g., solar cell or water splitting), or biology/medical science. As mentioned in the starting chapter, several main ideas and derivative applications using semiconductor nanocrystals have been successfully demonstrated by pioneering researchers, and continued to the next stage, determining the feasibility in a practical way. Regardless of the uniqueness of the semiconductor nanocrystals, it is clear that the multilateral approach on the material design, appropriate processing, and their harmonic organization into the devices is highly required to satisfy the needs of a market and accomplish the successful commercialization. Emerging reports based on the interdisciplinary cooperation by nature sciences and engineering departments reflect this consensus.

In this context mentioned above, this thesis discussed about the complete material–processing–device chains for optoelectronic devices based on the semiconductor nanocrystals, namely, light emitting diodes and solar cells.

From the viewpoint of the material design, morphological design of light conversion (InP@ZnSeS QDs) and light harvesting materials (CdSe tetrapods) was discussed. For the effective generation of photons from other energy sources, InP was chosen as a base material due to their low toxicity

compared with CdSe and spherical InP quantum dots with ZnSeS chemical composition gradient were synthesized by one-pot matter. Utilizing the reactivity difference between shell-forming precursors, the composition gradient of Se, Se dominantly located adjacent to the core, was easily achieved and performed as a buffer layer between core and shell phase. Employing the buffer layer mitigating lattice strain has been considered as an essential strategy for highly efficient core@shell QDs and the composition gradient shells can be powerful and versatile method to realize the core@shell formulations in easy, fast and reproducible way. Moreover the multiple composition gradient shells achieved high quantum efficiency above 70 %, comparable to the case of Cd-based QDs. In the future applications using QDs, heavy metal-free QDs will be replace the conventional Cd-based QDs to cope with the regulation for the use of heavy metal and the demonstration described here is able to be probable solution

Meanwhile, in order to facilitate the exciton dissociation for photovoltaic devices, tetrapod-shaped cadmium selenide nanocrystals were prepared based on the economic halide ligands and “continuous precursor injection” approach. Unlike the spherical nanocrystals elongated nanocrystals are thermodynamically unstable due to the enlarged surface area, so that the growth kinetics of such nanocrystals needs to be precisely considered. Using the halide ligands for controlling phase transformation of CdSe nanocrystals, the kinetic growth of wurtzite phase was precisely manipulated by the successive injection of reaction precursors, which determines the extent of kinetic growth of nanocrystal’s facets by adjusting the diffusion flux of

precursors from bulk to the nanocrystal's surface. The CdSe tetrapods prepared with this new synthetic route exhibit excellent shape selectivity above 90 % as well as finely tunable arm length (from 20 nm to 150 nm) and diameter (from 3 nm to 11 nm) by controlling the reaction temperature and injection rate. Moreover, multi-gram scale production was possible without degeneration of morphological uniformity.

Based on the newly synthesized nanocrystal systems, QD-based light emitting diodes and CdSe tetrapod:P3HT organic-inorganic bulk heterojunction solar cells were fabricated with the tailored fabrication process as well as the device structures.

For the InP QD-based light emitting diodes, the inverted device structures with an ZnO electron transporting layer was adopted due to the easy integration with thin film transistor backplanes and the capability of various hole transporting materials capable by thermal evaporation process. However, in spite of those advantages, the high conduction band position of InP QDs impedes a facilitated electron injection from ZnO to InP QDs. Therefore, a solution processible PFN layer was employed at the interface between ZnO and InP QDs as an interfacial dipole layer. A large difference in a solubility of ZnO, PFN, and QDs to organic solvents enabled the sequential orthogonal processing to stack three different layers and resulting devices represented largely improved device performance in terms of the maximum EQE of 3.46 % and a maximum luminance of 3900 cd/$m^2$, thanks to the balanced carrier injection and recombination.

For the utilization of CdSe tetrapods to organic-inorganic hybrid solar cells, new fabrication process, separating the formation of porous inorganic phase and the pore filling with conducting polymers, was developed for CdSe tetrapod:P3HT bulk heterojunction solar cells. While the simple blending of ligandless CdSe tetrapods and P3HT frequently causes the irreversible precipitation of nanocrystals, the new fabrication process guarantees the colloidal stability of CdSe tetrapods by exchanging oleate ligands bound on the surface with easily-detachable oleylamine ligands, and form ligand-free CdSe surface through spin coating followed by simple rinsing process. Thanks to the improved stability of nanocrystal dispersion and the fixed morphology of CdSe tetrapod phase, reliable and reproducible fabrication of organic-inorganic solar cells was capable without the concerning about the dependence of the connectivity between nanocrystals and aggregation morphology on the surface treatment of nanocrystals, and it served the clear platform to understand the photophysical phenomena in organic-inorganic hybrid solar cells. It was found that the surface passivation of CdSe nanocrystals with primary amine is essential for improving device performance, attributed to the reduction in surface state-mediated bimolecular recombination of charged carriers. The optimized device showed considerable photon-to-current efficiency up to 2.2 % and still had room for improvement by replacing organic parts with advanced low bandgap polymers or molecules.

From the viewpoint of material engineering, this thesis has suggested the complete development process for semiconductor nanocrystal-based optoelectronic devices, from the material design for the purpose (i.e., light

generation or harvesting), the fabrication process (i.e., orthogonal concept or sequential approach), to the structural design of optoelectronic devices (i.e., electric parts such as interfacial dipole layer or inorganic buffer layers). Each part are closely related and determined by the other parts. For example, the semiconductor nanocrystals prepared here guided the probable device structure (e.g., multilayered structure for QDs and bulkheterojunction morphology for tetrapods), and it leads the development of new processing method (e.g., sequential approach for solar cells). In opposite point of view, it is able to interpret the requirement of novel processing method leads to the modification of materials (e.g., ligand exchange of CdSe tetrapods). In this context, the series of research in this thesis proposed the one of probable direction for realizing the optoelectronic devices based on semiconductor nanocrystals. Here, I would like to suggest the outlook for the realization of practical QD-LEDs or organic-inorganic hybrid solar cells in terms of nanomaterial, processing, and device aspects.

In the aspect of materials, the regulation of the hazardous chemical compounds (e.g., Cd or Pb) and the production cost (i.e., mass production capability) can be possible constraints for the commercialization of semiconductor nanocrystal-based applications. Therefore, following researches need to surely consider those social and economic factors before establishing research concepts. For example, research on QDs composed of group III-V compounds (e.g., InP, GaP, InAs, or GaAs) have recently been emerged to replace Cd-based QDs, and the poor stability and quality of InP QDs have gradually been resolved by ceaseless dedication from the material

science area, including this thesis. In order to fully replace Cd-based QDs in the future, the poor color purity (full width at half maximum ~ 50 nm) and stability need to be matured through the innovative synthetic strategy and new reaction precursors. In the meantime, the light harvesting nanocrystals need to be changed to Cd-free ones with smaller bandgap, for instance, I-III-VI compounds such as copper chalcopyrite, cooper indium gallium selenide, or copper zinc tin sulfide. Besides, lead chalcogenides are also probable candidates for efficient IR absorber as well as novel carrier generation mechanism (namely, multiple exciton generation). The heavy metal regulation in solar cell area seems to be less tight than others due to the energy crisis, thus the light harvesting materials need to be chosen according not only to the environmental reason, but also to the social needs. In the point of material property, in the meantime, their distinctive physical phenomena such as quantum confinement effect, charging problem, multi-carrier dynamics (e.g., Auger process or multiple exciton generation), or electronic transport need to be carefully investigated under the single, many-body levels, or device configuration. Deeper understanding about those aspects has been recently emerged in several research groups, and such efforts give an important clue for designing optoelectronic devices.

The processing plays the role of a bridge for realizing novel nanomaterials to actual devices. Commonly, semiconductor nanocrystals are prepared as a form of solution phase, so that the processing for those nanomaterials has to be carefully considered to accomplish highly precise and reliable structures without damages during multiple fabrication steps.

Moreover the high throughput is an also critical requirement for commercialization. From this point of view, common processing conducted in a lab (e.g., spin coating) cannot be easily applied to the actual production of nanomaterial-based devices. Considering that the processing window and the number of steps are determined by both the state of materials (i.e., solubility, viscosity, or stability against thermal, chemical, or mechanical stresses) and the final device structure (i.e., multilayered thin films or three-dimensional structures), the processing for QD-LEDs or nanocrystal-based solar cells should be designed in different way. For the light emitting devices, the printing process with high precision and reliability will be particularly essential to integrate and pixelate multiple layers including QDs into the thin film transistor backplanes. In the meantime, the common solar cells has simpler device structure than LEDs, thus the high throughput processing would be more necessary. The roll-to-roll processing would be the probable candidate for the mass production of solution processed solar cells. Although current status on printing technologies is still insufficient to compete with conventional photolithography and vacuum deposition process, the engineering in the materials will be able to expand the processing condition as well as the reliability. From the viewpoint of material engineering, the organic-inorganic hybrid concept, granting flexible processibility of organic materials to the nanocrystals, can be one of examples.

The fundamental principle of semiconductor nanocrystal-based optoelectronic devices has a similarity with the conventional technologies; the sandwiched structures of organic light emitting diodes (OLEDs) and their

electronic materials are applied to QD-LEDs in the same way as before and the operation mechanism and constraints (e.g., energy level alignment, lifetime problem, and efficiency roll-off) looks same as the initial stage of OLEDs. In addition, the bulkheterojunction concept of organic-inorganic hybrid solar cells in this thesis also originates from the organic solar cells and shares similar problems with common solar cell technologies. In spite of the similarity of the device structures and the operation mechanism with the organic-based devices, however, the photophysical phenomena in semiconductor nanocrystals are distinctively different from the organic semiconductors and also from the bulk inorganic materials. And the current nanocrystal-based optoelectronics devices have not fully reflected those properties. Controlling the physical property of nanocrystals under the framework of electronic devices are highly required to resolve the current obstacles in the nanocrystal-based devices, such as low quantum efficiency and lifetime compared with the previous arts. Based on the accumulated knowledge about the device physics, the novel device architectures suitable for facilitated carrier injection, transport, carrier recombination or dissociation will be pursued to achieve the full potential of semiconductor nanocrystals in a framework of devices.

Although this thesis has focused on the light emitting diodes and solar cells which manipulate the light and electrons, the underlying principle discussed here can be widely applied to the other applications based on the novel materials and offer reasonable guidelines. It is believed that

Interdisciplinary approach and ceaseless devotions will make a success on the realization of nanoscience into the practical applications.

# Bibliography

[1] Rossetti, R.; Nakahara, S.; Brus, L. E., *J. Chem. Phys.* **1983,** *79* (2), 1086-1088.

[2] Efros, A. L.; Rosen, M., *Annu. Rev. Mat. Sci.* **2000,** *30* (1), 475-521.

[3] Murray, C. B.; Kagan, C. R.; Bawendi, M. G., *Annu. Rev. Mat. Sci.* **2000,** *30* (1), 545-610.

[4] Smith, A. M.; Nie, S., *Acc. Chem. Res.* **2009,** *43* (2), 190-200.

[5] Talapin, D. V.; Lee, J.-S.; Kovalenko, M. V.; Shevchenko, E. V., *Chem. Rev.* **2009,** *110* (1), 389-458.

[6] Vanmaekelbergh, D.; Liljeroth, P., *Chem. Soc. Rev.* **2005,** *34* (4), 299-312.

[7] Talapin, D. V.; Rogach, A. L.; Haase, M.; Weller, H., *J. Phys. Chem. B* **2001,** *105* (49), 12278-12285.

[8] Puzder, A.; Williamson, A. J.; Zaitseva, N.; Galli, G.; Manna, L.; Alivisatos, A. P., *Nano Lett.* **2004,** *4* (12), 2361-2365.

[9] Qu, L.; Yu, W. W.; Peng, X., *Nano Lett.* **2004,** *4* (3), 465-469.

[10] Liu, H.; Owen, J. S.; Alivisatos, A. P., *J. Am. Chem. Soc.* **2006,** *129* (2), 305-312.

[11] Xie, R.; Li, Z.; Peng, X., *J. Am. Chem. Soc.* **2009,** *131* (42), 15457-15466.

[12] Owen, J. S.; Chan, E. M.; Liu, H.; Alivisatos, A. P., *J. Am. Chem. Soc.* **2010,** *132* (51), 18206-18213.

[13] Norris, D. J.; Sacra, A.; Murray, C. B.; Bawendi, M. G., *Phys. Rev. Lett.* **1994,** *72* (16), 2612-2615.

[14] Li, J.; Wang, *Nano Lett.* **2003,** *3* (10), 1357-1363.

[15] Colvin, V. L.; Schlamp, M. C.; Alivisatos, A. P., *Nature* **1994,** *370* (6488), 354-357.

[16] Schlamp, M. C.; Peng, X.; Alivisatos, A. P., *J. Appl. Phys.* **1997,** *82* (11), 5837-5842.

[17] Sun, Q.; Wang, Y. A.; Li, L. S.; Wang, D.; Zhu, T.; Xu, J.; Yang, C.; Li, Y., *Nat Photon* **2007,** *1* (12), 717-722.

[18] Qian, L.; Zheng, Y.; Xue, J.; Holloway, P. H., *Nat Photon* **2011,** *5* (9), 543-548.

[19] Kwak, J.; Bae, W. K.; Lee, D.; Park, I.; Lim, J.; Park, M.; Cho, H.; Woo, H.; Yoon, D. Y.; Char, K.; Lee, S.; Lee, C., *Nano Lett.* **2012**.

[20] Cho, K.-S.; Lee, E. K.; Joo, W.-J.; Jang, E.; Kim, T.-H.; Lee, S. J.; Kwon, S.-J.; Han, J. Y.; Kim, B.-K.; Choi, B. L.; Kim, J. M., *Nat Photon* **2009,** *3* (6), 341-345.

[21] Chan, W. C. W.; Nie, S., *Science* **1998,** *281* (5385), 2016-2018.

[22] Medintz, I. L.; Uyeda, H. T.; Goldman, E. R.; Mattoussi, H., *Nat. Mater.* **2005,** *4* (6), 435-446.

[23] Liu, W.; Choi, H. S.; Zimmer, J. P.; Tanaka, E.; Frangioni, J. V.; Bawendi, M., *J. Am. Chem. Soc.* **2007,** *129* (47), 14530-14531.

[24] Soo Choi, H.; Liu, W.; Misra, P.; Tanaka, E.; Zimmer, J. P.; Itty Ipe, B.; Bawendi, M. G.; Frangioni, J. V., *Nat Biotech* **2007,** *25* (10), 1165-1170.

[25] Liu, W.; Howarth, M.; Greytak, A. B.; Zheng, Y.; Nocera, D. G.; Ting, A. Y.; Bawendi, M. G., *J. Am. Chem. Soc.* **2008,** *130* (4), 1274-1284.

[26] Huynh, W. U.; Dittmer, J. J.; Alivisatos, A. P., *Science* **2002,** *295* (5564), 2425-2427.

[27] Sun, B.; Marx, E.; Greenham, N. C., *Nano Lett.* **2003,** *3* (7), 961-963.

[28] Gur, I.; Fromer, N. A.; Alivisatos, A. P., *J. Phys. Chem. B* **2006,** *110* (50), 25543-25546.

[29] Dayal, S.; Kopidakis, N.; Olson, D. C.; Ginley, D. S.; Rumbles, G., *Nano Lett.* **2009,** *10* (1), 239-242.

[30] Li, Y.; Mastria, R.; Fiore, A.; Nobile, C.; Yin, L.; Biasiucci, M.; Cheng, G.; Cucolo, A. M.; Cingolani, R.; Manna, L.; Gigli, G., *Adv. Mater.* **2009,** *21* (44), 4461-4466.

[31] Chen, H.-C.; Lai, C.-W.; Wu, I. C.; Pan, H.-R.; Chen, I. W. P.; Peng, Y.-K.; Liu, C.-L.; Chen, C.-h.; Chou, P.-T., *Adv. Mater.* **2011,** *23* (45), 5451-5455.

[32] Konstantatos, G.; Howard, I.; Fischer, A.; Hoogland, S.; Clifford, J.; Klem, E.; Levina, L.; Sargent, E. H., *Nature* **2006,** *442* (7099), 180-183.

[33] Szendrei, K.; Cordella, F.; Kovalenko, M. V.; Böberl, M.; Hesser, G.; Yarema, M.; Jarzab, D.; Mikhnenko, O. V.; Gocalinska, A.; Saba, M.; Quochi, F.; Mura, A.; Bongiovanni, G.; Blom, P. W. M.; Heiss, W.; Loi, M. A., *Adv. Mater.* **2009,** *21* (6), 683-687.

[34] Choi, C. L.; Koski, K. J.; Sivasankar, S.; Alivisatos, A. P., *Nano Lett.* **2009,** *9* (10), 3544-3549.

[35] Amirav, L.; Alivisatos, A. P., *J. Phys. Chem. Lett.* **2010,** *1* (7), 1051-1054.

[36] Ji, X.; Copenhaver, D.; Sichmeller, C.; Peng, X., *J. Am. Chem. Soc.* **2008,** *130* (17), 5726-5735.

[37] Wuister, S. F.; de Mello Donegá, C.; Meijerink, A., *J. Phys. Chem. B* **2004,** *108* (45), 17393-17397.

[38] Wei, S.-H.; Zunger, A., *Appl. Phys. Lett.* **1998,** *72* (16), 2011-2013.

[39] Norris, D. J.; Efros, A. L.; Erwin, S. C., *Science* **2008,** *319* (5871), 1776-1779.

[40] Kortan, A. R.; Hull, R.; Opila, R. L.; Bawendi, M. G.; Steigerwald, M. L.; Carroll, P. J.; Brus, L. E., *J. Am. Chem. Soc.* **1990,** *112* (4), 1327-1332.

[41] Gur, I.; Fromer, N. A.; Geier, M. L.; Alivisatos, A. P., *Science* **2005,** *310* (5747), 462-465.

[42] Tian, Y.; Newton, T.; Kotov, N. A.; Guldi, D. M.; Fendler, J. H., *J. Phys. Chem.* **1996,** *100* (21), 8927-8939.

[43] Peng, X.; Schlamp, M. C.; Kadavanich, A. V.; Alivisatos, A. P., *J. Am. Chem. Soc.* **1997,** *119* (30), 7019-7029.

[44] Li, J. J.; Wang, Y. A.; Guo, W.; Keay, J. C.; Mishima, T. D.; Johnson, M. B.; Peng, X., *J. Am. Chem. Soc.* **2003,** *125* (41), 12567-12575.

[45] Pan, D.; Wang, Q.; Jiang, S.; Ji, X.; An, L., *Adv. Mater. (Weinheim, Ger.)* **2005,** *17* (2), 176-179.

[46] Talapin, D. V.; Mekis, I.; Götzinger, S.; Kornowski, A.; Benson, O.; Weller, H., *J. Phys. Chem. B* **2004,** *108* (49), 18826-18831.

[47] Reiss, P.; Protière, M.; Li, L., *Small* **2009,** *5* (2), 154-168.

[48] Zhong, X.; Han, M.; Dong, Z.; White, T. J.; Knoll, W., *J. Am. Chem., Soc.* **2003,** *125* (28), 8589-8594.

[49] Zhong, X.; Zhang, Z.; Liu, S.; Han, M.; Knoll, W., *J. Phys. Chem. B* **2004,** *108* (40), 15552-15559.

[50] Xinhua, Z.; Yaoyu, F.; Yuliang, Z.; Zhenyu, G.; Lei, Z., *Nanotechnology* **2007,** *18* (38), 385606.

[51] Deng, Z.; Yan, H.; Liu, Y., *J. Am. Chem. Soc.* **2009,** *131* (49), 17744-

17745.

[52] Xie, R.; Kolb, U.; Li, J.; Basché, T.; Mews, A., *J. Am. Chem. Soc.* **2005,** *127* (20), 7480-7488.

[53] Bae, W. K.; Char, K.; Hur, H.; Lee, S., *Chem. Mater.* **2008,** *20* (2), 531-539.

[54] Kim, S.; Kim, T.; Kang, M.; Kwak, S. K.; Yoo, T. W.; Park, L. S.; Yang, I.; Hwang, S.; Lee, J. E.; Kim, S. K.; Kim, S.-W., *J. Am. Chem. Soc.* **2012**.

[55] Li, L.; Reiss, P., *J. Am. Chem. Soc.* **2008,** *130* (35), 11588-11589.

[56] Kim, T.; Kim, S. W.; Kang, M.; Kim, S.-W., *J. Phys. Chem. Lett.* **2011,** *3* (2), 214-218.

[57] Holmes, J. D.; Johnston, K. P.; Doty, R. C.; Korgel, B. A., *Science* **2000,** *287* (5457), 1471-1473.

[58] Jun, Y.-w.; Choi, J.-s.; Cheon, J., *Angew. Chem., Int. Ed.* **2006,** *45* (21), 3414-3439.

[59] Lu, X.; Hanrath, T.; Johnston, K. P.; Korgel, B. A., *Nano Lett.* **2002,** *3* (1), 93-99.

[60] Trentler, T. J.; Goel, S. C.; Hickman, K. M.; Viano, A. M.; Chiang, M. Y.; Beatty, A. M.; Gibbons, P. C.; Buhro, W. E., *J. Am. Chem. Soc.* **1997,** *119* (9), 2172-2181.

[61] Yu, H.; Buhro, W. E., *Adv. Mater.* **2003,** *15* (5), 416-419.

[62] Hanrath, T.; Korgel, B. A., *J. Am. Chem. Soc.* **2002,** *124* (7), 1424-1429.

[63] Pacholski, C.; Kornowski, A.; Weller, H., *Angew. Chem.* **2002,** *114* (7), 1234-1237.

[64] Yu, J. H.; Joo, J.; Park, H. M.; Baik, S.-I.; Kim, Y. W.; Kim, S. C.; Hyeon,

T., *J. Am. Chem. Soc.* **2005,** *127* (15), 5662-5670.

[65] Penn, R. L.; Banfield, J. F., *Geochim. Cosmochim. Acta* **1999,** *63* (10), 1549-1557.

[66] Cho, K.-S.; Talapin, D. V.; Gaschler, W.; Murray, C. B., *J. Am. Chem. Soc.* **2005,** *127* (19), 7140-7147.

[67] Milliron, D. J.; Hughes, S. M.; Cui, Y.; Manna, L.; Li, J.; Wang, L.-W.; Paul Alivisatos, A., *Nature* **2004,** *430* (6996), 190-195.

[68] Williams, K. J.; Tisdale, W. A.; Leschkies, K. S.; Haugstad, G.; Norris, D. J.; Aydil, E. S.; Zhu, X. Y., *ACS Nano* **2009,** *3* (6), 1532-1538.

[69] Zhou, Y.; Riehle, F. S.; Yuan, Y.; Schleiermacher, H.-F.; Niggemann, M.; Urban, G. A.; Kruger, M., *Appl. Phys. Lett.* **2010,** *96* (1), 013304-013303.

[70] Radychev, N.; Lokteva, I.; Witt, F.; Kolny-Olesiak, J.; Borchert, H.; Parisi, J. r., *J. Phys. Chem. C* **2011,** *115* (29), 14111-14122.

[71] Koleilat, G. I.; Levina, L.; Shukla, H.; Myrskog, S. H.; Hinds, S.; Pattantyus-Abraham, A. G.; Sargent, E. H., *ACS Nano* **2008,** *2* (5), 833-840.

[72] Beard, M. C.; Midgett, A. G.; Law, M.; Semonin, O. E.; Ellingson, R. J.; Nozik, A. J., *Nano Lett.* **2009,** *9* (2), 836-845.

[73] Tang, J.; Kemp, K. W.; Hoogland, S.; Jeong, K. S.; Liu, H.; Levina, L.; Furukawa, M.; Wang, X.; Debnath, R.; Cha, D.; Chou, K. W.; Fischer, A.; Amassian, A.; Asbury, J. B.; Sargent, E. H., *Nat. Mater.* **2011,** *10* (10), 765-771.

[74] Ip, A. H.; Thon, S. M.; Hoogland, S.; Voznyy, O.; Zhitomirsky, D.; Debnath, R.; Levina, L.; Rollny, L. R.; Carey, G. H.; Fischer, A.; Kemp, K. W.; Kramer, I. J.; Ning, Z.; Labelle, A. J.; Chou, K. W.; Amassian, A.; Sargent, E.

H., *Nat Nano* **2012,** *7* (9), 577-582.

[75] Coe, S.; Woo, W.-K.; Bawendi, M.; Bulovic, V., *Nature* **2002,** *420* (6917), 800-803.

[76] Ziegler, J.; Xu, S.; Kucur, E.; Meister, F.; Batentschuk, M.; Gindele, F.; Nann, T., *Adv. Mater.* **2008,** *20* (21), 4068-4073.

[77] Mattoussi, H.; Radzilowski, L. H.; Dabbousi, B. O.; Thomas, E. L.; Bawendi, M. G.; Rubner, M. F., *J. Appl. Phys.* **1998,** *83* (12), 7965-7974.

[78] Bae, W. K.; Kwak, J.; Park, J. W.; Char, K.; Lee, C.; Lee, S., *Adv. Mater.* **2009,** *21*, 1690.

[79] Jang, H. S.; Yang, H.; Kim, S. W.; Han, J. Y.; Lee, S. G.; Jeon, D. Y., *Adv. Mater.* **2008,** *20*, 2696.

[80] Sun, Q.; Wang, Y. A.; Li, L. S.; Wang, D.; Zhu, T.; Xu, J.; Yang, C.; Li, Y., *Nat. Photonics* **2007,** *1*, 717.

[81] Coe, S.; Woo, W. K.; Bawendi, M. G.; Bulovic, V., *Nature* **2002,** *420*, 800.

[82] Lee, J.; Sundar, V. C.; Heine, J. R.; Bawendi, M. G.; Jensen, K. F., *Adv. Mater.* **2000,** *12*, 1102.

[83] Colvin, V. L.; Schlamp, M. C.; Alivisatos, A. P., *Nature* **1994,** *370*, 354.

[84] Medintz, I. L.; Uyeda, H. T.; Goldman, E. R.; Mattoussi, H., *Nat. Mater.* **2005,** *4*, 435.

[85] Kim, S.; Lim, Y. T.; Soltesz, E. G.; De Grand, A. M.; Lee, J.; Nakayama, A.; Parker, J. A.; Mihaljevic, T.; Laurence, R. G.; Dor, D. M.; Cohn, L. H.; Bawendi, M. G.; Frangioni, J. V., *Nat. Biotechnol.* **2004,** *22*, 93.

[86] Derfus, A. M.; Chan, W. C. W.; Bhatia, S. N., *Nano Lett.* **2004,** *4*, 11.

[87] Bruchez, M.; Moronne, M.; Gin, P.; Weiss, S.; Alivisatos, A. P., *Science* **1998,** *281*, 2013.

[88] Huang, K.; Demadrille, R.; Silly, M. G.; Sirotti, F.; Reiss, P.; Renault, O., *ACS Nano* **2010,** *4*, 4799.

[89] Allen, P. M.; Walker, B. J.; Bawendi, M. G., *Angew. Chem., Int. Ed.* **2010,** *49*, 760.

[90] Xu, S.; Ziegler, J.; Nann, T., *J. Mater. Chem.* **2008,** *18*, 2653.

[91] Li, L.; Reiss, P., *J. Am. Chem. Soc.* **2008,** *130*, 11588.

[92] Xie, R.; Battaglia, D.; Peng, X., *J. Am. Chem. Soc.* **2007,** *129*, 15432.

[93] Borchert, H.; Haubold, S.; Haase, M.; Weller, H.; McGinley, C.; Riedler, M.; Moller, T., *Nano Lett.* **2002,** *2*, 151.

[94] Battaglia, D.; Peng, X., *Nano Lett.* **2002,** *2*, 1027.

[95] Haubold, S.; Haase, M.; Kornowski, A.; Weller, H., *ChemPhysChem* **2001,** *5*, 331.

[96] Micic, O. I.; Smith, B. B.; Nozik, A. J., *J. Phys. Chem. B* **2000,** *104*, 12149.

[97] Micic, O. I.; Curtis, C. J.; Jones, K. M.; Sprague, J. R.; Nozik, A. J., *J. Phys. Chem.* **1994,** *98*, 4966.

[98] Choi, H. S.; Ipe, B. I.; Misra, P.; Lee, J. H.; Bawendi, M. G.; Frangioni, J. V., *Nano Lett.* **2009,** *9*, 2354.

[99] Aharoni, A.; Mokari, T.; Popov, I.; Banin, U., *J. Am. Chem. Soc.* **2006,** *128*, 257.

[100] Kim, S. W.; Zimmer, J. P.; Ohnishi, S.; Tracy, J. B.; Frangioni, J. V.; Bawendi, M. G., *J. Am. Chem. Soc.* **2005,** *127*, 10526.

[101] Cao, Y.; Banin, U., *J. Am. Chem. Soc.* **2000,** *122*, 9692.

[102] Kang, Z.; Liu, Y.; Tsang, C. H. A.; Ma, D. D. D.; Fan, X.; Wong, N. B.; Lee, S. T., *Adv. Mater.* **2009,** *21*, 661.

[103] Zou, J.; Baldwin, R. K.; Pettigrew, K. A.; Kauzlarich, S. M., *Nano Lett.* **2004,** *4*, 1181.

[104] English, D. S.; Pell, L. E.; Yu, Z.; Barbara, P. F.; Korgel, B. A., *Nano Lett.* **2002,** *2*, 681.

[105] Holmes, J. D.; Ziegler, K. J.; Doty, R. C.; Pell, L. E.; Johnston, K. P.; Korgel, B. A., *J. Am. Chem. Soc.* **2001,** *123*, 3743.

[106] Bae, W. K.; Nam, M. K.; Char, K.; Lee, S., *Chem. Mater.* **2008,** *20*, 5307.

[107] Bae, W. K.; Char, K.; Hur, H.; Lee, S., *Chem. Mater.* **2008,** *20*, 531.

[108] Talapin, D. V.; Mekis, I.; Gotzinger, S.; Kornowski, A.; Benson, O.; Weller, H., *J. Phys. Chem. B* **2004,** *108*, 18826.

[109] Reiss, P.; Carayon, S.; Bleuse, J.; Pron, A., *Synth. Met.* **2003,** *139*, 649.

[110] McBride, S.; Treadway, J.; Feldman, L. C.; Pennycook, S. J.; Rosenthal, S. J., *Nano Lett.* **2006,** *6*, 1496.

[111] Lo, S. S.; Mirkovic, T.; Chuang, C.-H.; Burda, C.; Scholes, G. D., *Adv. Mater. (Weinheim, Ger.)* **2011,** *23* (2), 180-197.

[112] Choi, C. L.; Li, H.; Olson, A. C. K.; Jain, P. K.; Sivasankar, S.; Alivisatos, A. P., *Nano Lett.* **2011,** *11* (6), 2358-2362.

[113] Malkmus, S.; Kudera, S.; Manna, L.; Parak, W. J.; Braun, M., *J. Phys. Chem. B* **2006,** *110* (35), 17334-17338.

[114] Peng, P.; Milliron, D. J.; Hughes, S. M.; Johnson, J. C.; Alivisatos, A. P.;

Saykally, R. J., *Nano Lett.* **2005,** *5* (9), 1809-1813.

[115] Dayal, S.; Reese, M. O.; Ferguson, A. J.; Ginley, D. S.; Rumbles, G.; Kopidakis, N., *Adv. Funct. Mater.* **2010,** *20* (16), 2629-2635.

[116] Cui, Y.; Banin, U.; Björk, M. T.; Alivisatos, A. P., *Nano Lett.* **2005,** *5* (7), 1519-1523.

[117] Miszta, K.; de Graaf, J.; Bertoni, G.; Dorfs, D.; Brescia, R.; Marras, S.; Ceseracciu, L.; Cingolani, R.; van Roij, R.; Dijkstra, M.; Manna, L., *Nat. Mater.* **2011,** *10* (11), 872-876.

[118] Zhong, H.; Scholes, G. D., *J. Am. Chem. Soc.* **2009,** *131* (26), 9170-9171.

[119] Fiore, A.; Mastria, R.; Lupo, M. G.; Lanzani, G.; Giannini, C.; Carlino, E.; Morello, G.; De Giorgi, M.; Li, Y.; Cingolani, R.; Manna, L., *J. Am. Chem. Soc.* **2009,** *131* (6), 2274-2282.

[120] Talapin, D. V.; Nelson, J. H.; Shevchenko, E. V.; Aloni, S.; Sadtler, B.; Alivisatos, A. P., *Nano Lett.* **2007,** *7* (10), 2951-2959.

[121] Zhang, W.; Jin, C.; Yang, Y.; Zhong, X., *Inorg. Chem.* **2011,** *51* (1), 531-535.

[122] Liu, L.; Zhuang, Z.; Xie, T.; Wang, Y.-G.; Li, J.; Peng, Q.; Li, Y., *J. Am. Chem. Soc.* **2009,** *131* (45), 16423-16429.

[123] Karel Čapek, R.; Moreels, I.; Lambert, K.; De Muynck, D.; Zhao, Q.; Van Tomme, A.; Vanhaecke, F.; Hens, Z., *J. Phys. Chem. C* **2010,** *114* (14), 6371-6376.

[124] Peng, Z. A.; Peng, X., *J. Am. Chem. Soc.* **2001,** *123* (7), 1389-1395.

[125] Huang, J.; Kovalenko, M. V.; Talapin, D. V., *J. Am. Chem. Soc.* **2010,**

*132* (45), 15866-15868.

[126] Asokan, S.; Krueger, K. M.; Colvin, V. L.; Wong, M. S., *Small* **2007,** *3* (7), 1164-1169.

[127] Owen, J. S.; Park, J.; Trudeau, P.-E.; Alivisatos, A. P., *J. Am. Chem. Soc.* **2008,** *130* (37), 12279-12281.

[128] Seals, R. D.; Alexander, R.; Taylor, L. T.; Dillard, J. G., *Inorg. Chem.* **1973,** *12* (10), 2485-2487.

[129] Saruyama, M.; Kanehara, M.; Teranishi, T., *J. Am. Chem. Soc.* **2010,** *132* (10), 3280-3282.

[130] Gordon, J. E., *J. Org. Chem.* **1965,** *30* (8), 2760-2763.

[131] Yeh, C.-Y.; Lu, Z. W.; Froyen, S.; Zunger, A., *Phys. Rev. B* **1992,** *46* (16), 10086.

[132] Huang, F.; Banfield, J. F., *J. Am. Chem. Soc.* **2005,** *127* (12), 4523-4529.

[133] Manna, L.; Wang; Cingolani, R.; Alivisatos, A. P., *J. Phys. Chem. B* **2005,** *109* (13), 6183-6192.

[134] Coe, S.; Woo, W. K.; Bawendi, M. G.; Bulović, V., *Nature* **2002,** *420*, 800.

[135] Sun, Q.; Wang, Y. A.; Li, L. S.; Wang, D.; Zhu, T.; Xu, J.; Yang, C.; Li, Y., *Nat. Photon* **2007,** *1*, 717.

[136] Bae, W. K.; Nam, M. K.; Char, K.; Lee, S., *Chem. Mater.* **2008,** *20* (16), 5307-5313.

[137] Kim, S.; Kim, T.; Kang, M.; Kwak, S. K.; Yoo, T. W.; Park, L. S.; Yang, I.; Hwang, S.; Lee, J. E.; Kim, S. K.; Kim, S.-W., *J. Am. Chem. Soc.* **2012,** *134* (8), 3804-3809.

[138] Caruge, J. M.; Halpert, J. E.; Wood, V.; Bulovic, V.; Bawendi, M. G., *Nat Photon* **2008,** *2* (4), 247-250.

[139] Cho, K. S.; Lee, E. K.; Joo, W. J.; Jang, E.; Kim, T. H.; Lee, S. J.; Kwon, S. J.; Han, J. Y.; Kim, B. K.; Choi, B. L.; Kim, J. M., *Nat. Photon* **2009,** *3*, 341.

[140] Kwak, J.; Bae, W. K.; Lee, D.; Park, I.; Lim, J.; Park, M.; Cho, H.; Woo, H.; Yoon, D. Y.; Char, K.; Lee, S.; Lee, C., *Nano Lett.* **2012,** *12* (5), 2362-2366.

[141] Stouwdam, J. W.; Janssen, R. A. J., *J. Mater. Chem.* **2008,** *18* (16).

[142] Wood, V.; Halpert, J. E.; Panzer, M. J.; Bawendi, M. G.; Bulović, V., *Nano Lett.* **2009,** *9* (6), 2367-2371.

[143] Kim, T.-H.; Cho, K.-S.; Lee, E. K.; Lee, S. J.; Chae, J.; Kim, J. W.; Kim, D. H.; Kwon, J.-Y.; Amaratunga, G.; Lee, S. Y.; Choi, B. L.; Kuk, Y.; Kim, J. M.; Kim, K., *Nat Photon* **2011,** *5* (3), 176-182.

[144] Zhu, T.; Shanmugasundaram, K.; Price, S. C.; Ruzyllo, J.; Zhang, F.; Xu, J.; Mohney, S. E.; Zhang, Q.; Wang, A. Y., *Appl. Phys. Lett.* **2008,** *92* (2), 023111-023113.

[145] Haverinen, H. M.; Myllyla, R. A.; Jabbour, G. E., *Appl. Phys. Lett.* **2009,** *94* (7), 073108-073103.

[146] Kazlas, P. T.; Zhou, Z.; Stevenson, M.; Niu, Y.; Breen, C.; Kim, S.-J.; Stecket, J. S.; Coe-Sullivan, S.; Ritter, J., *SID Symposium Digest of Technical Papers* **2010,** *41* (1), 473-476.

[147] Li, L.; Daou, T. J.; Texier, I.; Kim Chi, T. T.; Liem, N. Q.; Reiss, P., *Chem. Mater.* **2009,** *21* (12), 2422-2429.

[148] Nakamura, H.; Kato, W.; Uehara, M.; Nose, K.; Omata, T.; Otsuka-Yao-Matsuo, S.; Miyazaki, M.; Maeda, H., *Chem. Mater.* **2006,** *18* (14), 3330-3335.

[149] Zhang, J.; Xie, R.; Yang, W., *Chem. Mater.* **2011,** *23* (14), 3357-3361.

[150] Chen, D.; Viswanatha, R.; Ong, G. L.; Xie, R.; Balasubramaninan, M.; Peng, X., *J. Am. Chem. Soc.* **2009,** *131* (26), 9333-9339.

[151] Norris, D. J.; Yao, N.; Charnock, F. T.; Kennedy, T. A., *Nano Lett.* **2000,** *1* (1), 3-7.

[152] Pradhan, N.; Peng, X., *J. Am. Chem. Soc.* **2007,** *129* (11), 3339-3347.

[153] Xie, R.; Peng, X., *J. Am. Chem. Soc.* **2009,** *131* (30), 10645-10651.

[154] Ippen, C.; Greco, T.; Wedel, A., *Journal of Information Display* **2012,** *13* (2), 91-95.

[155] Lim, J.; Bae, W. K.; Lee, D.; Nam, M. K.; Jung, J.; Lee, C.; Char, K.; Lee, S., *Chem. Mater.* **2011,** *23* (20), 4459-4463.

[156] Xie, R.; Battaglia, D.; Peng, X., *J. Am. Chem. Soc.* **2007,** *129* (50), 15432-15433.

[157] Zhang, Y.; Xie, C.; Su, H.; Liu, J.; Pickering, S.; Wang, Y.; Yu, W. W.; Wang, J.; Wang, Y.; Hahm, J.-i.; Dellas, N.; Mohney, S. E.; Xu, J., *Nano Lett.* **2010,** *11* (2), 329-332.

[158] Yang, X.; Divayana, Y.; Zhao, D.; Leck, K. S.; Lu, F.; Tan, S. T.; Abiyasa, A. P.; Zhao, Y.; Demir, H. V.; Sun, X. W., *Appl. Phys. Lett.* **2012,** *101* (23), 233110.

[159] Pacholski, C.; Kornowski, A.; Weller, H., *Angew. Chem. Int. Ed.* **2002,** *41* (7), 1188-1191.

[160] Lim, J.; Bae, W. K.; Kwak, J.; Lee, S.; Lee, C.; Char, K., *Opt. Mater.*

*Express* **2012,** *2* (5), 594-628.

[161] Fu, H.; Zunger, A., *Phys. Rev. B* **1997,** *56* (3), 1496.

[162] Wood, V.; Panzer, M. J.; Halpert, J. E.; Caruge, J. M.; Bawendi, M. G.; Bulović, V., *ACS Nano* **2009,** *3* (11), 3581-3586.

[163] He, Z.; Zhong, C.; Su, S.; Xu, M.; Wu, H.; Cao, Y., *Nat Photon* **2012,** *6* (9), 591-595.

[164] Seo, J. H.; Nguyen, T.-Q., *J. Am. Chem. Soc.* **2008,** *130* (31), 10042-10043.

[165] Choi, H.; Park, J. S.; Jeong, E.; Kim, G.-H.; Lee, B. R.; Kim, S. O.; Song, M. H.; Woo, H. Y.; Kim, J. Y., *Adv. Mater.* **2011,** *23* (24), 2759-2763.

[166] Guan, X.; Zhang, K.; Huang, F.; Bazan, G. C.; Cao, Y., *Adv. Funct. Mater.* **2012,** *22* (13), 2846-2854.

[167] Huang, F.; Wu, H.; Wang, D.; Yang, W.; Cao, Y., *Chem. Mater.* **2004,** *16* (4), 708-716.

[168] Wu, H.; Huang, F.; Mo, Y.; Yang, W.; Wang, D.; Peng, J.; Cao, Y., *Adv. Mater.* **2004,** *16* (20), 1826-1830.

[169] Yang, T.; Wang, M.; Duan, C.; Hu, X.; Huang, L.; Peng, J.; Huang, F.; Gong, X., *Energy Environ. Sci.* **2012,** *5* (8), 8208-8214.

[170] Schreuder, M. A.; Xiao, K.; Ivanov, I. N.; Weiss, S. M.; Rosenthal, S. J., *Nano Lett.* **2010,** *10* (2), 573-576.

[171] Wan Ki, B.; Jeonghun, K.; Jaehoon, L.; Donggu, L.; Min Ki, N.; Kookheon, C.; Changhee, L.; Seonghoon, L., *Nanotechnology* **2009,** *20* (7), 075202.

[172] Beard, M. C.; Turner, G. M.; Murphy, J. E.; Micic, O. I.; Hanna, M. C.;

Nozik, A. J.; Schmuttenmaer, C. A., *Nano Lett.* **2003,** *3* (12), 1695-1699.

[173] Mićić, O. I.; Jones, K. M.; Cahill, A.; Nozik, A. J., *The Journal of Physical Chemistry B* **1998,** *102* (49), 9791-9796.

[174] Crooker, S. A.; Hollingsworth, J. A.; Tretiak, S.; Klimov, V. I., *Phys. Rev. Lett.* **2002,** *89* (18), 186802.

[175] Lili, H.; Donghuan, Q.; Xi, J.; Yanshan, L.; Li, W.; Junwu, C.; Yong, C., *Nanotechnology* **2006,** *17* (18), 4736.

[176] Olson, J. D.; Gray, G. P.; Carter, S. A., *Sol. Energy Mater. Sol. Cells* **2009,** *93* (4), 519-523.

[177] Zhou, Y.; Eck, M.; Veit, C.; Zimmermann, B.; Rauscher, F.; Niyamakom, P.; Yilmaz, S.; Dumsch, I.; Allard, S.; Scherf, U.; Krüger, M., *Sol. Energy Mater. Sol. Cells* **2011,** *95* (4), 1232-1237.

[178] Zhou, Y.; Riehle, F. S.; Yuan, Y.; Schleiermacher, H.-F.; Niggemann, M.; Urban, G. A.; Kruger, M., *Applied Physics Letters* **2010,** *96* (1), 013304.

[179] Ren, S.; Chang, L.-Y.; Lim, S.-K.; Zhao, J.; Smith, M.; Zhao, N.; Bulović, V.; Bawendi, M.; Gradečak, S., *Nano Lett.* **2011,** *11* (9), 3998-4002.

[180] Sun, B.; Greenham, N. C., *Phys. Chem. Chem. Phys.* **2006,** *8* (30), 3557-3560.

[181] Liu, J.; Tanaka, T.; Sivula, K.; Alivisatos, A. P.; Fréchet, J. M. J., *J. Am. Chem. Soc.* **2004,** *126* (21), 6550-6551.

[182] Wu, Y.; Zhang, G., *Nano Lett.* **2010,** *10* (5), 1628-1631.

[183] Sun, B.; Snaith, H. J.; Dhoot, A. S.; Westenhoff, S.; Greenham, N. C., *J. Appl. Phys.* **2005,** *97* (1), 014914.

[184] Wang, P.; Abrusci, A.; Wong, H. M. P.; Svensson, M.; Andersson, M. R.;

Greenham, N. C., *Nano Lett.* **2006,** *6* (8), 1789-1793.

[185] Gur, I.; Fromer, N. A.; Chen, C.-P.; Kanaras, A. G.; Alivisatos, A. P., *Nano Lett.* **2006,** *7* (2), 409-414.

[186] Qian, L.; Yang, J.; Zhou, R.; Tang, A.; Zheng, Y.; Tseng, T.-K.; Bera, D.; Xue, J.; Holloway, P. H., *J. Mater. Chem.* **2011,** *21* (11), 3814-3817.

[187] Greaney, M. J.; Das, S.; Webber, D. H.; Bradforth, S. E.; Brutchey, R. L., *ACS Nano* **2012,** *6* (5), 4222-4230.

[188] Ekimov, A. I.; Hache, F.; Schanne-Klein, M. C.; Ricard, D.; Flytzanis, C.; Kudryavtsev, I. A.; Yazeva, T. V.; Rodina, A. V.; Efros, A. L., *J. Opt. Soc. Am. B* **1993,** *10* (1), 100-107.

[189] Hassinen, A.; Moreels, I.; de Mello Donegá, C.; Martins, J. C.; Hens, Z., *J. Phys. Chem. Lett.* **2010,** *1* (17), 2577-2581.

[190] Fritzinger, B.; Capek, R. K.; Lambert, K.; Martins, J. C.; Hens, Z., *J. Am. Chem. Soc.* **2010,** *132* (29), 10195-10201.

[191] Green, P. F., *Soft Matter* **2011,** *7* (18), 7914-7926.

[192] Knowles, K. E.; Tice, D. B.; McArthur, E. A.; Solomon, G. C.; Weiss, E. A., *J. Am. Chem. Soc.* **2009,** *132* (3), 1041-1050.

[193] Schilinsky, P.; Waldauf, C.; Brabec, C. J., *Appl. Phys. Lett.* **2002,** *81* (20), 3885-3887.

[194] Riedel, I.; Parisi, J.; Dyakonov, V.; Lutsen, L.; Vanderzande, D.; Hummelen, J. C., *Adv. Funct. Mater.* **2004,** *14* (1), 38-44.

# 초 록

반도체 나노입자는 형태, 크기 및 화학적 조성을 변화시킴으로써 나노입자 내부의 전자준위밀도, 엑시톤의 형성 및 재결합, 전도현상 등 다양한 광물리학적 현상을 단일 나노입자 혹은 이들의 집합체 수준에서 자유자재로 제어할 수 있다는 장점을 가지고 있다. 따라서 반도체 나노입자를 전기발광소자, 태양전지, 광촉매 등 빛과 전자의 효율적인 상호변환이 요구되는 광전자소자의 차세대 소재로 적용하고자 하는 연구가 다양한 학제간의 교류를 통해 계속되고 있다. 성공적인 광전자소자를 제작하기 위해서는, 광물리학적 현상을 제어하고 원하는 방향으로 발현시키기 위한 나노입자의 형태, 조성 및 구조에 대한 재구성뿐만이 아니라, 이를 집약시킨 최적의 소자구조 및 제작공정에 대한 포괄적인 고려가 필요하다. 이상의 맥락에서, 본 학위 논문에서는 고효율의 전기발광소자 또는 유기-무기 하이브리드 태양전지에 초점을 맞추어, 반도체 나노입자를 빛 또는 전자의 생산에 최적화된 형태로 합성하고 이들을 광전자소자로 제작하는 연구에 대해 논의하고자 한다.

제 1 장에서는, 엑시톤의 효과적인 재결합을 유도하여 고발광성의 나노입자를 구현하기 위하여 인화인듐 구형 나노입자를 핵@껍질 구조로 합성하였다. 인화인듐 핵과 황화아연 껍질의 격자불일치에서 비롯되는 광효율 저하를 최소화하기 위하여, 핵과 껍질의 격자상수

차이를 완화시킬 수 있는 셀렌화아연을 황화아연 껍질에 화학적 농도구배 형태로 도입하였다. 셀레늄 전구체와 황 전구체의 반응성 차이를 이용하여 셀렌화아연이 인화인듐 핵 주변부에 주로 분포하도록 껍질의 조성을 제어한 결과, 핵과 껍질 사이의 격자상수 차이가 효과적으로 완화되어 양자점의 발광효율이 70% 이상으로 향상되었으며, 물리적/화학적 열화 요소로부터 양자점의 발광특성이 안정적으로 유지되도록 껍질의 두께를 증가시킬 수 있었다.

한편, 엑시톤 파동함수의 비편재화를 최대화시켜 효과적인 전하분리 및 전하수송특성을 지닌 무기물 광흡수체를 구현하고 이를 유기-무기 하이브리드 태양전지로 응용하기 위하여, 사지상형의 셀렌화 카드뮴 나노입자를 대량합성하는 방법을 개발하였다. 셀렌화카드뮴의 결정구조를 제어할 수 있는 저가의 할로겐 리간드와 더불어 나노입자의 이방성 성장을 제어하기 위한 연속주입법을 고안하여 적용한 결과, 섬아연광구조의 핵에 4 개의 육방결정구조 가지가 성장된 사지상형 나노입자를 90% 이상의 높은 형상선택도와 다양한 종횡비로 대량합성 할 수 있었다.

제 2 장에서는, 고효율의 인화인듐 양자점을 전기발광소자의 발광층으로 도입하는 연구를 수행하였다. 양자점 발광층 내부로의 원활한 전하주입 및 재결합을 유도하기 위하여, 본 연구에서는 투명전극을 음극으로, 산화아연/공액고분자전해질을 전자주입층으로 사용하는 역방향의 하부발광 소자구조를 도입하였다.

공액고분자전해질에 의해 형성된 계면쌍극자가 산화아연과 인화인듐간의 전자주입장벽을 최소화하여 전자와 홀의 균형잡힌 재결합을 유도함에 따라, 양자점 전기발광소자의 외부양자효율(3.46 %)과 최대밝기(3,900 cd/$m^2$)가 기존 기술 대비 큰 폭으로 향상되었다.

제 3 장에서는, 카드뮴 셀레나이드 사지상형 나노입자를 유기-무기 하이브리드 태양전지의 광흡수체로 도입하기 위하여, 나노입자와 공액고분자간의 벌크이종접합을 산화아연 완충층 상에 순차적으로 조립하는 연구를 수행하였다. 이상의 단계적 공정은 표면처리된 이방성 나노입자의 콜로이드 안정성을 효과적으로 유지하여 유기-무기 이종접합 박막의 균일성 및 공정성을 크게 향상시킬 수 있었다. 한편 사지상형 나노입자 표면에 존재하는 트랩 준위를 1-헥실아민을 통해 최소화하여 poly(3-hexylthiophene) 고분자와 유기-무기 하이브리드 벌크이종접합 태양전지를 구현한 결과, 2.2%의 전력변환효율을 나타내었다.

이상의 연구 결과는 반도체 나노입자 기반의 광전자소자를 성공적으로 구현하기 위해서는 소재, 제작공정, 그리고 소자구조에 대한 깊이 있는 이해와 종합적인 접근이 필요함을 시사한다. 각각의 요소에 대한 학제간의 긴밀한 교류를 통해, 나노과학 분야의 다양한 결과들이 신개념의 광전자소자에 성공적으로 적용되기를 기대한다.

주요어: 반도체 나노입자, 양자점, 사지상형 나노입자, 양자점 발광소자, 유기-무기 하이브리드 태양전지

학 번: **2007-21216**